The Influence of Charge Transport Layer Interfaces on the Performance of Electroluminescent Colloidal Quantum Dot Light-Emitting Devices

by

Tyler Davidson-Hall

A thesis

presented to the University of Waterloo

in fulfillment of the

thesis requirement for the degree of

Doctor of Philosophy

in

Electrical and Computer Engineering

Waterloo, Ontario, Canada, 2020

Author's Declaration

I hereby declare that I am the sole author of this thesis. This is a true copy of the thesis, including any required final revisions, as accepted by my examiners.

I understand that my thesis may be made electronically available to the public

Abstract

Electroluminescent quantum dot light-emitting devices (QDLEDs) are a relatively new technology for displays that have all of the benefits of emissive displays commonly associated with organic light-emitting devices (OLEDs) such as low power draw, deeper black levels, and fast refresh rates. However, QD emitters confer additional valuable characteristics for displays due to their high photoluminescence quantum yield (PLQY) approaching 100%, narrow emission full-width at half maximum (FWHM < 20 nm), the tunability of their peak luminescence wavelengths across the entire visible spectrum, and their solution-processability which makes them compatible to low-cost and flexible fabrication techniques. Unfortunately, like their organic counterpart, the long-term stability of QDLEDs has been limited for many years. While high-efficiency red and green QDLEDs have recently been demonstrated with electroluminescence lifetimes of over 1,000,000 hours, this may not be suitable for some applications given the luminance of the devices for which these lifetimes are rated. Furthermore, like OLEDs, blue QDLEDs are far less stable than red and green with the record lifetime being orders of magnitude less. Therefore, it is important to understand the mechanisms governing QDLED stability in order to improve device lifetimes. In general, the main degradation mechanism affecting QDLEDs has been attributed to multi-charge carrier interactions referred to as Auger recombination which uniquely affects QDs to a greater degree due to their nanoscale structure but also the inherent charge imbalance within QDLEDs. However, there is little focus on the degradation of devices outside of this process. Given the similarity in structure between QDLEDs and OLEDs, this work aims to elucidate upon additional degradation mechanisms that may influence the long-term stability of these devices by considering the degradation mechanisms that affect organic semiconductors.

This thesis investigates each interface present within the QDLED structure to identify its influence on QDLED performance, with strategies to improve efficiency in addition to the main focus of device stability. The primary interfaces of interest occur between the electron transport layer (ETL) and the QD emission layer (EML) as well as between the QD EML and the hole transport layer (HTL). However, the interface between the HTL and the hole injection layer (HIL) will also be shown to influence the electroluminscence stability of QDLEDs despite not interacting with the QD layer directly. This work utilizes the hybrid inverted QDLED structure which consists of an inorganic ETL and an organic HTL as this structure has proven to be far superior to devices with all-organic or all-inorganic transport layers. Therefore, it is the HTL that will be of particular interest in this thesis. Red and green QDs were utilized as the EML over the course of this work, but the primary focus will be on the red QDLEDs as they resulted in the most efficient and long-lives devices allowing for a better environment in which the influence of the interfaces on QDLED performance could be evaluated. However, the results should be applicable to a wide range of QD EMLs of different colours and compositions.

The role of the ETL / EML interface in QDLED performance was investigated by introducing the wide band gap work function modification layer between the two layers. While a $1.6\times$ improvement in maximum EQE was observed, this coincided with a worsening of the charge imbalance. Rather than a result of improved charge balance, this efficiency enhancement was attributed to a reduction in QD exciton quenching by the ZnO due to the passivation of surface states at this interface. While this resulted in a negligible effect on the EL stability of these QDLEDs at the time, further experiments investigating the effect of excitons at the EML / HTL interface would identify these excitons as an issue for long-term QDLED stability. Ultimately, the main influence of the ETL / EML interface on QDLED performance lies in the exciton quenching effect of ZnO surface states which limits the QD film PLQY. The influence of the ETL and EML layers on morphological stability was investigated by a systematic study on the processing parameters of ZnO and the QDs for spherical and rod-shape QDs. The main factor determining the degree of morphological degradation in the emissive area homogeneity was the roughness of each layer. This is

also a limitation in OLED morphological stability, as the organic semiconductors are prone to crystallization when deposited on rough surfaces. Therefore, although rough layers are the catalyst of this morphological instability, it is the organic HTL that is the limiting factor in long-term morphological stability.

The role of degradation of the HTL on overall QDLED stability was further investigated through PL measurements from QDLEDs over time while irradiated with UV light. By measuring changes in the QD PL over time under constant UV illumination in devices with a variety of organic semiconductors, it became clear that the HTL has a significant influence over the loss in QD PLQY during aging. While the QDs individually are relatively stable during the measurement period, the PLQY loss in the QDLEDs correlated to the individual PLQY loss of the organic layers. It was therefore found that the exciton-induced degradation of the organic molecules at the QD / HTL interface that is particularly deleterious to QDLED stability. A multi-layer HTL structure was investigated in order to improve charge balance and reduce hole accumulation at the QD / HTL interface. With the optimized structure, a 25× enhancement in QDLED lifetime was observed. This HTL structure allows for the use of alternate HILs which do not damage the underlying organic layers during device fabrication, restricts the accumulation of holes at the QD / HTL interface and reduces charging of the QD layer, and limits degradation of the HTL at the QD / HTL interface. Ultimately, this work has identified and characterized a degradation mechanism affecting long-term EL stability of QDLEDs and presents a device structure which utilizes a cascading HTL with small gaps between each component's HOMO energy level with an organic HIL minimizing the effects of this mechanism on QDLED EL stability.

Acknowledgments

This PhD journey was incredibly rewarding, where every step along the way provided a new challenge to overcome. In the moment – when nothing you try seems to work – it's frustrating. But in hindsight they're important character, patience, and research skills building experiences that I wouldn't trade for anything else. Throughout all of this I couldn't have asked for a better supervisor than Professor Hany Aziz, whose guidance, compassion, invaluable knowledge, and insights have inspired me to become a better researcher and a better person.

I would like to acknowledge my advisory committee, Professor Siva Sivoththaman, Professor Irene Goldthorpe and Professor Kevin Musselman for reviewing my work and their valuable comments and suggestions. I would also like to thank Professor Ghassan Jabbour for accepting the role as my external PhD examiner and Professor Na Young Kim for attending my PhD Seminar.

Special thanks go out to my colleagues, Hossein Zamani Siboni, Qi Wang, Graeme Williams, Yingjie Zhang, Uyxing Vongsaysy, Yoshitaka Kajiyama, Bin Sun, Sibi Sutty, Elizabeth Salsberg, Amanda Victorious, Hyeonghwa Yu, Yongjoo Cho, Edward Jin, Mozhgan Sadeghian-Lemraski, Ahmed Elbaroudy, Peng Wang, Dong Seob Chung, Fatemeh Samaeifar, and Atefeh Ghorbani Koltapeh for all of their advice and discussions throughout my graduate studies, academic or otherwise.

I would like to thank Richard Barber and Czang-Ho Lee for their technical assistance and for making the Giga-to-Nano lab facilities a great working environment.

I would also like to thank my parents, Brenda Davidson and Jack Hall; my siblings, Dylan, Jackie, and Lee-Ann; and all the rest of my extended family and friends for their love and support. I would not have been able to do it without you all.

Most of all, I'd like to thank Natalie Hirano for her continual support, kindness, and understanding during those long nights in the lab and accepting my erratic schedule. You kept me sane and grounded in the ensuing exhaustion. Without question, the best and most important part of graduate school was all the time that we spent together.

Table of Contents

List of Figures

List of Tables

List of Abbreviations & Chemical Names

2,6-DCzPPy	2,6-bis[3-(9H-carbazol-9-yl)phenyl]pyridine
AFM	Atomic force microscope
Alq3	tris-(8-hydroxyquinoline)aluminium
CBP	4,4'-N,N'-dicarbazole-biphenyl
CHTL	A hole transport layer consisting of several materials with cascading energy levels
DCJTB	4-(dicyanomethylene)-2-t-butyl-6-(1,1,7,7-tetramethyljulolidyl-9-enyl)-4H-pyran
EL	Electroluminescence
EML	Emission layer
EQE	External quantum efficiency
ETL	Electron transport layer
FIrpic	bis(4,6-difluorophenylpyridinato-N,C2)picolinatoiridium
FRET	Förster resonance energy transfer
FWHM	Full-width at half-maximum
HATCN	1,4,5,8,9,11-hexaazatriphenylene-hexanitrile
HOMO	Highest occupied molecular orbital
HTL	Hole transport layer
HTM	Hole transport material
IPA	Isopropanol
IQE	Internal quantum efficiency
ITO	Indium tin oxide
JVL	Current density-voltage-luminance
LCD	Liquid crystal display

LED	Light-emitting device
LT50	Time for a LED to reach 50% of its initial luminance under constant electrical driving
LUMO	Lowest unoccupied molecular orbital
mCP	1,3-bis(carbazol-9-yl)benzene
MEA	Monoethanolamine
MoO3	Molybdenum trioxide
NiO	Nickel oxide
NPB	N,N′-bis(naphthalen-1-yl)-N,N′-bis(phenyl)benzidine
OLED	Organic light-emitting device
OPV	Organic photovoltaics
OSC	Organic semiconductor
PEDOT:PSS	poly(ethylenedioxythiophene):polystyrene sulfonate
PEI	polyethylenimine
PEIE	polyethylenimine ethoxylated
PFI	tetrafluoroethylene-perfluoro-3,6-dioxa-4-methyl-7-octene-sulfonic acid
PL	Photoluminescence
PMMA	poly(methyl methacrylate)
Poly-TPD	poly(N,N′-bis(4-butylphenyl)- N,N′-bis(phenyl)benzidine)
PPV	poly(p-phenylenevinylene)
PVK	poly(vinylcarbazole)
QD	Quantum dot
QDLCD	Liquid crystal display incorporating a quantum dot colour conversion layer
QDLED	Quantum dot light-emitting device
QY	Quantum yield

RMS	Root-mean square
Spiro-2NPB	2,2′,7,7′-tetrakis[N-naphthalenyl(phenyl)-amino]-9,9-spirobifluorene
Spirot-CBP	2,2',7,7'-tetrakis(carbazol-9-yl)-9,9-spirobifluorene
Spiro-TPD	spiro-N,N′-diphenyl-N,N′-bis(3-methylphenyl)-(1,1′-biphenyl)-4,4′-diamine
TAZ	3-(4-biphenylyl)-4-phenyl-5-t-butylphenyl-1,2,4-triazole
TBADN	3-tert-butyl-9,10-di(naphth-2-yl)anthracene
t-Bu-PBD	2-(biphenyl-4-yl)-5-(4-tert-butylphenyl)-1,3,4-oxadiazole
TCTA	4,4′,4″-tris- (carbazol-9-yl)triphenylamine
TFB	poly(9,9-dioctylfluorene-co-N-(4-(3-methylpropyl))diphenylamine
TM	Transition moment
TOP	Trioctylphosphine
TOPO	Trioctylphosphine oxide
TPBi	1,3,5-tris(2-N-phenylbenzimidazolyl)-benzene
TPD	N,N'-diphenyl-N,N'-bis(3-methylphenyl)-(1,1'-biphenyl)-4,4'-diamine
TrPL	Transient photoluminescence
TTA	Triplet-triplet annihilation
ZnAc	Zinc acetate
ZnO	Zinc oxide
ZTO	Zinc tin oxide

Chapter 1: Introduction and Background

The emergence of colloidal quantum dots (QDs) nearly 4 decades ago has spurred significant efforts to utilize their unique characteristics and optimize their luminescence for many optical applications such as light-emitting devices (QDLEDs) for displays and solid-state lighting, photovoltaics, and biological labeling. CdSe-based QDs dominate in the visible spectrum due to their high photoluminescence (PL) quantum yield (PLQY) approaching 100%, narrow emission full-width at half maximum (FWHM < 20 nm), the tunability of their peak luminescence wavelengths across the entire visible spectrum, and their solution-processability which makes them amenable to low-cost processing.[1–8]

Recently, commercial liquid crystal displays (LCDs) became available with QDs used as colour conversion films (in what has been deemed QLED commercially, but will be referred to here as QDLCD for clarity) reaping the benefits of the good PL stability and emissive properties of QDs. Although LCDs rose to prominence due to their own superiority to the previous generation of display technology, organic light-emitting diode (OLED) displays have begun to challenge LCDs as the dominant technology.[9] In an LCD, polarized light from a white backlight transmits through a film of liquid crystal molecules which can further polarize the light. The polarization factor is controlled by the orientation of the liquid crystal molecules which is controlled by an applied electric field. Finally, a fixed polarizer only allows a specific polarization of the incident photons which are then passed through red, green, and blue colour filters to produce RGB sub-pixels in a display. The main drawbacks of this technology are: the large power draw of the always-on backlight, poor contrast from the minimum black level which arises from the baseline light level transmitted through the OFF liquid crystal state, and poor colour saturation as the RGB subpixel colour is defined by overlap of the broad white backlight emission spectrum with the allowable transmission by each colour filter.[9] While LCDs can be considered a transmissive display technology, OLEDs are an emissive technology so only the sub-pixels that are used to display the image are turned on, resulting in low power draw, deeper black levels, and fast refresh rates.[9–11] Although the light emitted by OLEDs is still

often transmitted through polarizers and colour filters which can reduce their brightness, this has less of an effect compared to LCDs as each sub-pixel of the OLED display can be fabricated to selectively emit red, green, and blue photons. Perhaps one of the most unique properties of OLEDs arises from the low temperature fabrication process as this allows for the use of flexible plastic substrates and low-cost, large scale processing although this feature is seldom realized in current commercial applications.[11] The drawbacks of OLED displays generally lie in their molecular instability – particularly blue OLEDs – since the organic semiconductors (OSCs) used in this technology degrade over time due to environmental, chemical, and physical mechanisms and thus are not as robust as the inorganic semiconductors traditionally used in displays.[9,10,20,12–19] The different degradation rates of the RGB sub-pixels manifests as the image burn-in commonly associated with OLED displays. The development of QDLCDs has improved colour saturation since they can be used as colour filters themselves and their narrow emission spectra can achieve much larger colour spaces required for ultra-high-definition displays. However, the prospect of utilizing QDs as the emitter in an emissive display technology is tantalizing for the same reasons that they are utilized in LCDs, allowing for much more narrow emitters compared to OLEDs (~50 nm FWHM). A simplified schematic breakdown of the components in QDLCDs and QDLEDs is illustrated below in **Figure 1.1**.
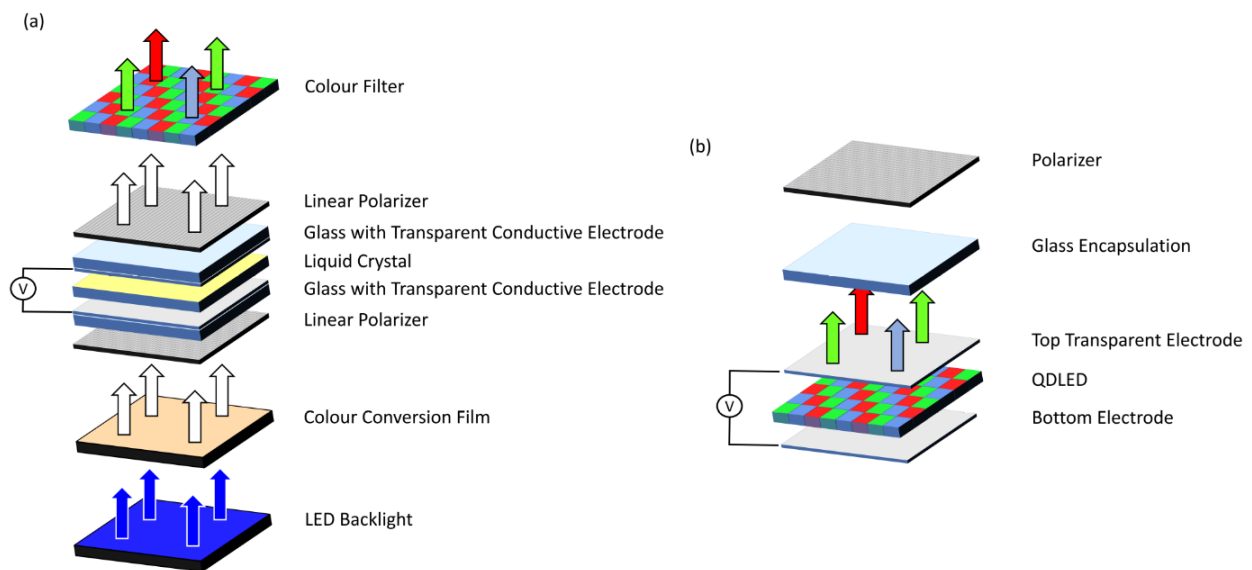
Figure 1.1 A simplified schematic breakdown of (a) QDLCD and (b) QDLED displays.

Recently, red and green QDLEDs have demonstrated comparable efficiencies and lifetimes to OLEDs, which will be discussed in later sections. Due to their generally inorganic composition, QDs may be able to achieve highly efficient and stable blue emission by avoiding the degradation mechanisms that plague organic semiconductors, but this has not yet been realized. The discrete nature of QDs in a cast film as well as strong carrier confinement and exciton confinement results in properties akin to disordered amorphous molecular semiconductors such as OSCs.[21] As such, much of the early work on electroluminescent (EL) QDLEDs operation mechanics and device structures have built upon the groundwork laid by OLED research. For the most part, QDLEDs are very similar to OLEDs, with the exception of the emissive layer (EML) which is a layer of QDs as opposed to a luminescent OSC. Although most improvements in QDLED efficiency have resulted from enhancements in QD synthesis techniques, there is room to improve both efficiency and stability of QDLEDs through optimization of the device architecture. While OLED degradation mechanisms have been extensively studied and will be relevant to the devices discussed in this thesis, there has been a lack of specific investigation into the degradation mechanisms of QDLEDs. The largest factor governing QDLED degradation is currently accepted as excessive charging of QDs due to the inherent charge imbalance within these devices.[2,22-29] Beyond the effect of charges on QDs, degradation in QDLEDs remains a relatively unexplored topic.

1.1 Thesis Overview

In chapter 1, basic information regarding the mechanism by which photons are created via radiative recombination of excitons is presented, the quantum confinement effect which gives QDs their unique optical properties is then discussed, followed by a section detailing common colloidal QD properties, materials, and synthesis methods as they relate to QDLEDs, and finally concluding with a section on EL QDLED operation mechanisms, architectures, and degradation mechanisms.

In chapter 2, a brief history of QDLEDs from their inception is split up into 3 sections covering their initial years of exploration (1994-2005), the intermediate years of development (2006-2012), and the recent years of refinement (2013-2019), followed by a section detailing the literature on QDLED stability, finally concluding with the motivation for this work and the objectives it aims to address.

Chapter 3 details the experimental procedures utilized in this work with respect to device fabrication, including the material selection, device layout, and deposition techniques, followed by descriptions of the techniques used to characterize the QDLEDs in this work, including current-voltage-luminance characterization, EL and PL stability measurements, steady state and time-resolved EL and PL spectrometry, and surface morphological characterization.

In chapter 4, the role that the interface between the electron transport layer and emission layer plays in device performance is explored by introducing a wide bandgap polymer work function modification layer at this interface.

In chapter 5, the role of the electron transport and emission layers on the morphological stability of QDLEDs is investigated systematically by varying the processing parameters and characteristics of each layer.

In chapter 6, the role that excitons play in the degradation of QDLEDs is explored through PL stability measurements elucidating upon the extent to which degradation of the organic transport layers can influence the overall device stability especially for degradation that occurs near the QD interface.

In chapter 7, the role of hole accumulation at the QD interface and degradation of the hole transport layer is investigated while also developing an improved device structure in order to minimize the accumulation of charge carriers near the QD interface, leading to significantly improved QDLED EL stability.

Finally, a summary of the research results and conclusions of this work are provided in chapter 8 along with directions for future work.

1.2   The Transition Moment

The fundamental mechanism governing light emission and absorption is the transition moment (TM) of a material, which defines the probability of excitation or relaxation of an electron from its initial state (*a*) to its final state (*b*). In the context of this work, the initial state is the excited, higher energy state whereas the final state is the lower energy ground state. The transition rate between these states can be found by integrating Fermi's golden rule equation across all initial and final states considering the probability that each state is filled.[30] After making some modifications to fit our use of this equation, the total transition rate per unit volume can be written as:

$$R_t = \frac{4}{\hbar V} \sum_{k_a} \sum_{k_b} |\hat{e} \cdot < b|\mu|a > |^2 \frac{\gamma}{(E_b - E_a - \hbar\omega)^2 + \gamma^2} (f_a - f_b) \tag{1}$$

Where *V* is volume, *k* is the initial or final wavevector, $\hat{e}$ is the wave polarization vector, μ is the dipole moment, γ is the FWHM of the Lorenzian lineshape, *E* is the energy state, $\hbar$ is the reduced Planck constant, ω is the frequency of the absorbed or emitted photon, and *f* is the probability of a particular state to be occupied by an electron.[30] In this equation, the evaluation of the dipole moment with respect to initial and final eigenstates is called the transition moment and is the factor that defines the probability of excitation or relaxation of the electron. A series of simplifications to the TM can be made to separate the expression into a product of independent integrals:

$$< b|\mu|a > \approx \int \theta_b^* \theta_a \, dt_N \cdot \int S_b^* S_a \, dt_S \cdot \int \varphi_b^* \mu \, \varphi_a \, dt_e \tag{2}$$

This separation results in integrals corresponding to the nuclear vibrational ($\int \theta_b^* \theta_a \, dt_N$), electron spin ($\int S_b^* S_a \, dt_S$), and electron spatial overlap ($\int \varphi_b^* \mu \, \varphi_a \, dt_e$) wavefunctions.[31,32] This important factorization is possible since the nuclear motion of a molecule can be considered negligible compared to that of the electron, given their large mass difference and that only the initial and final orbitals of the electron need to be considered, assuming that electron-electron interactions are negligible and only one electron participates

in each transition.[31,32] If any of the three separate integrals that make up the simplified TM are equal to zero, then that particular transition is deemed forbidden and will not proceed. The so-called forbidden transitions are only impossible due to the preceding assumptions that were made and when these assumptions are no longer accurate there may be a small possibility for these transitions. However, in most cases these assumptions are accurate enough to explore the selection rules for allowed, or probable, transitions.

According to Hund's rule and the Pauli exclusion principle, degenerate energy orbitals will be filled with the same spin – either up or down – since this is the most stable electronic orientation and it is forbidden to have two electrons with the same 4 quantum numbers in an orbital.[32] Thus, the triplet state with parallel spins is forbidden in the ground state and the singlet state is the only allowable ground state.[32] For a non-zero solution to the electronic spin overlap integral the initial and final states must be the same – either singlet or triplet.[32] Thus, an excitation will only be allowed in a singlet $\rightarrow$ singlet and likewise for a relaxation. Mathematically, triplet $\rightarrow$ triplet transitions are also allowed so, while not necessarily possible for excitations, this will be important in the discussion of energy transfer mechanisms between molecules. However, this is one case where the assumptions made earlier misrepresent the capability of an electronic transition since the singlet $\rightarrow$ triplet transition probability is merely negligible in a standard organic molecule.[32] The effect of spin-orbit coupling imbues some singlet character to triplet states and vice versa via a perturbation either through: (i) interactions between the magnetic dipole of an electron, its orbital motion, and the static field from the positively charge nucleus which scales with the quartic power of atomic weight, or (ii) by decreasing the gap between singlet and triplet state energy such that thermal energy can induce a flip in the electron spin.[32]

There are a number of possible allowable relaxations of an excited electron whether by radiation or a loss to phonon vibrations.[33] The excited state lifetime is very short and ultimately determined by the fastest transition rate. Allowed transitions, such as the singlet radiative recombination transition, $S_1 \rightarrow S_0$, occurs quickly with a rate constant $k_f \sim 10^6 - 10^9$ s^{-1} whereas the forbidden triplet transition, $T_1 \rightarrow S_0$, is much slower with a rate constant of $k_p \sim 10^{-2} - 10^4$ s^{-1}.[33] Meanwhile, radiationless transitions occur between energy

envelopes of electronic states with degenerate energy levels so there is no dissipation of energy through emission of a photon or vibration.[33] Following a radiationless transition, an electron will likely not be in the ground state and will expend any excess energy through vibrational relaxation.[33] Quenching is a detrimental competing process to radiative transitions that can be caused by a multitude of sources but is generally due to some sort of impurity which leads to a loss of the excited state energy through non-radiative dissipation.[33] Energy transfer is similar but not necessarily undesirable and in many cases it can be essential for efficient devices although in combination with quenchers it may reduce device performance.

The main energy transfer mechanism that is relevant to QDLEDs is Förster resonance energy transfer (FRET). FRET occurs through a coupling of dipoles between two molecules where the wavefunctions of the donor and acceptor both oscillate with the same frequency, facilitating the transition of an excited state from the donor to acceptor.[31] FRET requires an overlap in the emission spectrum of the donor with the absorption spectrum of the acceptor similar to the trivial energy transfer mechanism.[31] While the two processes are similar in effect, they occur over two different ranges – trivial energy transfer can occur over any distance but the FRET transition rate scales with R^{-6} as seen in the following equation:

$$\Gamma_F = \frac{1}{\tau_D}\frac{1}{R^6}\left(\frac{3}{4\pi}\int \frac{c^4}{\omega^4 n^4}F_D(\omega)\sigma_A(\omega)d\omega\right) \tag{3}$$

Where τ_D is the excited state lifetime, R is the distance between donor and acceptor, c is the speed of light, n is the refractive index of the medium, F_D is the emission spectrum of the donor and σ_A is the absorption spectrum of the acceptor.[31] The FRET range is typically limited to distances < 10 nm.[31] There are some cases where Dexter energy transfer, an exchange of electrons between a donor and acceptor molecule which requires a spatial overlap of the orbitals (as opposed to dipole-dipole overlap in FRET), may occur in QDLEDs. This necessitates an even closer separation between the two molecules, typically < 1 nm, so it is not common due to the large spatial separations between QD cores in a film.

1.3   Quantum Confinement

The source of QDs' unique and attractive properties for light emission (primarily their size-tunable band gap, and emission and absorption spectra) lies in quantum confinement of excitons. The exciton is a bound state formed due to the Coulombic attractions between an electron and hole.[21] In bulk materials, the exciton radius can be modeled as a hydrogenic atom's Bohr radius (a_B) and is given by the following equation:

$$a_B = \frac{4\pi\epsilon_0\epsilon_r\hbar^2}{m_r^*e^2} = \frac{\epsilon_r m_e}{m_r^*} * (0.53 \text{ Å}) \tag{4}$$

Where ϵ_0 is the vacuum permittivity, ϵ_r is the permittivity of the medium, m_r^* is the reduced effective mass of the electrons and holes, e is the elementary charge, and m_e is the mass of a free electron. If the quantum dot size is smaller than the exciton radius, then the exciton will be strongly confined within the QD. Quantum dot sizes on the same order of magnitude should weakly confine excitons.[21] In both confinement conditions, excitons will no longer be able to move freely in that dimension. Just as in the particle-in-a-box and hydrogen atom models (solutions are detailed in refs.[21,34–36]), the confinement of an exciton in one or more dimensions will discretize the number of states that the exciton can occupy as well as shift the ground state energy level toward higher values.

This size-dependent energy gap is perhaps the most valuable trait of QDs. Since both electrons and holes will be confined to the small radius of the QD, there is a Coulombic attraction between the negative and positively charged components of the exciton that forms imparting a Frenkel-like character as opposed to the Wannier-Mott excitons in bulk semiconductors.[21] While the Coulomb potential energy used in hydrogen atom energy state calculations would typically be used to evaluate the exciton binding energy, if the quantum dot is strongly confined (i.e. $R < a_B$), then the hydrogen model begins to break down and the Brus equation is used instead which includes a charge carrier separation distance factor as highly confined excitons will have larger binding energies.[21,35,37,38] However, since the exciton binding energy as estimated

by the Brus equation is only inversely related to the QD radius its effect on the transition energy is not as strong as confinement.[21,35,37,38] The electronic transition energy for the lowest states of a spherical quantum dot can be written as:

$$\hbar\omega = E_{g,bulk} + \frac{\hbar^2\pi^2}{2m_r^*R^2} - \frac{1.8e^2}{\epsilon_0\epsilon_rR} \tag{5}$$

Where $\hbar\omega$ is the energy required for an electronic transition between states (i.e. the formation or recombination of an exciton), $E_{g,bulk}$ represents the bulk band gap of the material, the second term represents the combined electron and hole confinement energy, and the third term represents the Coulombic interaction between the confined electron and hole. R is the radius of the spherical QD. Therefore, one can see that the energy of an exciton in a QD will always be greater than that of its bulk counterpart and that decreasing the QD radius will increase this energy value. This QD exciton energy will be referred to as the band gap for convenience in the following work.

For a spherical particle with radius R, the envelope function of a charge carrier in the particle can be found to have the following form:

$$\Phi_{n,l,m}(r,\theta,\varphi) = C\frac{j_l(k_{n,l}r)Y_l^m(\theta,\varphi)}{r} \tag{6}$$

$$k_{n,l} = \frac{\alpha_{n,l}}{R} \tag{7}$$

Where C is a normalization constant, $j_l(k_{n,l}r)$ is the lst order spherical Bessel function and $\alpha_{n,l}$ is the nth zero of j_l, and Y_l^m is a spherical harmonic. The eigenfunctions of equation (6) are atomic-like orbitals that can be identified with the quantum numbers n (1,2,3…), l (s,p,d,…), and m (for which the resultant energies are degenerate and this can be ignored).[39] The energy of each state (n,l) is given by:

$$E_{n,l} = \frac{\hbar^2\alpha_{n,l}^2}{2mR^2} \tag{8}$$

Where each of the resultant levels corresponds to an atomic-like orbital that is confined to the QD (1S, 1P, 1D, 2S, …). This energy is used in equation (5) to find the lowest energy state of the quantum dot (1S)

where the first zero of the 1st order spherical Bessel function is equal to π.[5] The higher energy states correspond to each of the allowable QD energies, and is depicted in **Figure 1.2** in relation to the k-space depiction of a bulk semiconductor's energy states.
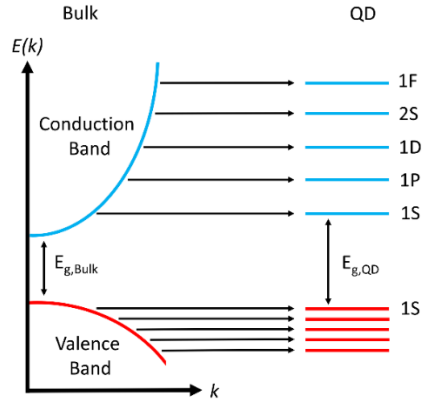
Figure 1.2 Comparison of the atomic-like orbitals of QD energy states to bulk energy states in k-space. Adapted with permission.[5] Copyright 2016 American Chemical Society.

In many bulk semiconductors including CdSe, the minimum conduction state of electrons is derived from S-type atomic orbitals and is 2-fold degenerate due to the spin state of the electron. However, the valence band maximum is derived from P-type wavefunctions which are split by spin-orbit interactions into a 4-fold degenerate band (heavy and light holes) with Bloch function angular momentum $j = 3/2$ and a 2-fold degenerate band (split-off) with angular momentum $j = 1/2$.[39–42] The light hole sub-band has an angular momentum projection of $j_m = \pm 1/2$ and the heavy hole sub-band has an angular momentum projection of $j_m = \pm 3/2$.[5] Depending on the crystal structure of the semiconductor, crystal-field splitting may induce a separation in the light hole and heavy hole bands (Δ_{AB}).[39–42] For CdSe, zinc-blende crystals do not have an energy level split whereas wurtzite crystals have a crystal-field splitting of $\Delta_{AB} = 26$ meV.[5,39]

In QDs where the effective mass of holes is much greater than the effective mass of electrons (in CdSe, $m_h = 6m_e$), the energy separation between the valence band states becomes small enough that quantum confinement-induced mixing of the hole sub-bands is observed.[39–42] The valence bands in these QDs are therefore characterized by the total angular momentum $F = j + l$, a vector sum of the Bloch function angular

momentum and the orbital momentum l which corresponds to the atomic-like orbitals that arise from the quantum mechanical solution of the QD wavefunction.[39–42] The convention for writing these mixed states is the form nl_F which would be $1S_{3/2}$ for the lowest energy valence band. A comparison of the valence band splitting in a bulk semiconductor and QDs, showing the fine structure of the band edge energy states and allowable transitions, is included below in **Figure 1.3**. One can see that the lowest energy electron-hole pair would reside in the 1S (electron) and $1S_{3/2}$ (hole) energy levels.
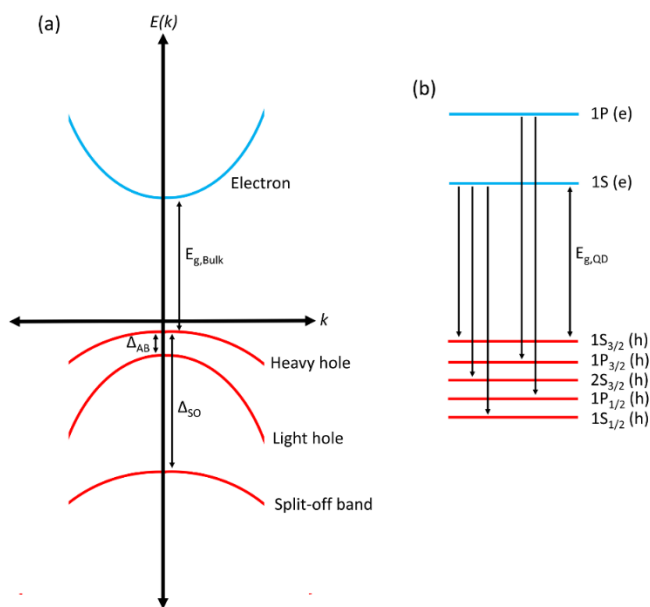
Figure 1.3 Valence band splitting in (a) a bulk semiconductor, showing the heavy and light hole splitting (Δ_{AB}) and split-off hole band (Δ_{SO}) and (b) for a QD, depicting the fine structure splitting of the band edge energy states and allowable radiative transitions. Adapted with permission.[5] Copyright 2016 American Chemical Society.

1.4　Colloidal Quantum Dots

The two dominant growth techniques that separate QD classifications are epitaxial growth and wet chemistry colloidal suspensions. Epitaxial growth and photolithography allows for precise patterning and positioning of individual QDs for applications in quantum computing and cryptography. Meanwhile, colloidal QDs are more applicable for large-scale devices as it is possible to utilize the multitude of solution coating techniques for deposition while also offering much more control over process scalability, carrier confinement, size, distribution and even shape.[2] All of the QDs discussed in this work will be colloidal suspensions for their application to QDLEDs for which their solution-processability is a major attractive feature. Practically, this allows for the synthesis of QDs with specific size (and, therefore, emission wavelengths) targeted to maximize the colour space of a display. The very narrow density of allowable states in QDs results in narrow light emission spectra with FWHM values < 20 nm which also contributes to highly saturated colours for displays. Semiconductors are the most common QD due to their intermediate confinement size (< 10 nm) which are easiest to fabricate and band gap (< 4 eV) which can be manipulated for interesting optical properties in the visible, IR, and UV ranges.[21]

1.4.1　Core Materials

Although QDs can be synthesized from a wide variety of materials, and semiconductors such as Si, C, CdTe, PbSe, and PbS are highly researched topics in fields such as photovoltaics, thermoelectrics, and biological sensing, CdSe has become the dominant QD core material for light emission. CdSe is a group II-VI semiconductor with a bulk band gap of 1.74 eV with a deep red emission peak (712 nm) which allows it to cover the entire visible spectrum by manipulating the QD size reduced as depicted in **Figure 1.4**. However, the very small radius required for blue QDs results in poor quality and size distribution due to the difficulty in controlling uniformity in short reaction times at low temperatures, among other undesirable confinement-related properties of small QDs.[5,43–45]

13
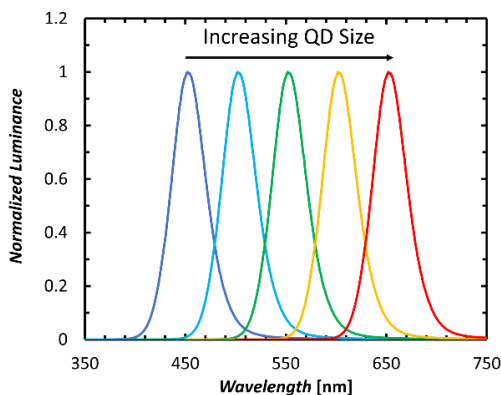
Figure 1.4 Size-dependent emission spectra of CdSe-based QDs.

However, CdSe is a highly toxic and carcinogenic material that has restrictions on the amount that can be incorporated in commercial products. In order to switch to a safer fabrication process and product, alternate core materials have recently experienced an increased research initiative. InP has become a leading QD core material in this regard since its 1.27 eV bulk band gap allows for the synthesis of red- and green-emitting QDs with PLQYs approaching that of CdSe core QDs, with encouraging recent reports on device performance.[46–49] Unfortunately, that leaves a void in the blue range that has not been sufficiently filled for Cd-free QDs as the best candidate material to date, ZnSe with a bulk band gap of 2.82 eV, has thus far proven to be suboptimal.[50] Blue QDs are therefore generally relegated to using CdS with a bulk band gap of 2.42 eV or an alloyed core of $Zn_xCd_{1-x}Se_{1-y}S_y$ with a bulk band gap between CdSe and ZnS.[51–55]

1.4.2 Shell Structure & Materials

QDs were initially synthesized and utilized in a homogeneous core-only form, but these QDs had poor PLQY and spectral stability as a consequence of significant exciton quenching due to dangling surface bonds and surface oxidation. This has been overcome through progress in QD design and synthesis. By introducing a subsequent protective "shell" around the QD emissive core, the surface defects on the core that limited spectral stability and PLQY earlier could be passivated provided that the lattice constant of the

14

core and shell are similar.[56–62] This QD structure is generally referred to as core / shell to reflect the instant change in composition from the core to the shell. While there are surface defects on the outer radius of the shell which can quench excitons, selecting a shell material with adequately shallower conduction band energy and deeper valence band energy relative to the core will confine the electron and hole wavefunctions to the core. This concept is illustrated in **Figure 1.5**. The requirement of a larger band gap and similar lattice constant to CdSe means that only a few materials are suitable for the shell, the three most common being CdS, ZnSe, and ZnS. Organic ligands are also used to passivate QD surface defects with the added benefit of improving solubility in organic solvents which simplifies solution-based deposition processes.[61–65]

By increasing the shell thickness, the distance separating surface defects from the core excitons can be increased to a point that nearly 100% PLQY can be attained.[66–69] This is suitable for photo-excited QDs where excitons are created via photon absorption, but when charge injection and transport are also important (i.e. in EL QDLEDs) then thick shells may impede the overall device performance. Gradient composition QDs have been pursued to address this issue and also to reduce lattice mismatch stresses.[70–75] A gradual change in the chemical composition from the core to the shell (i.e. CdSe / CdSe$_{1-x}$S$_x$ / CdS, where x increases from 0 to 1 with increasing radius) smooths out the abrupt change in conduction and valence energy levels and lattice constant to a gradual slope that is controllable by the synthesis process. The gradient composition QDs have also demonstrated reduced Auger recombination rates. The convention of core@shell is generally used to differentiate gradient QDs from the instant change in composition of core / shell QDs.
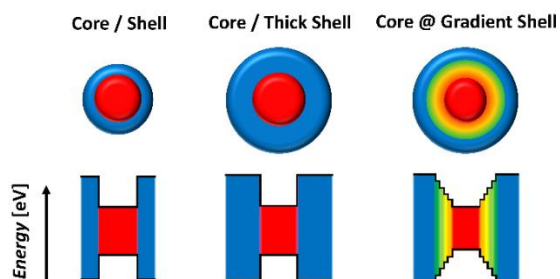
Figure 1.5 A structural and energy level schematic depiction of the three dominant structures of QDs commonly used in QDLEDs: core / shell, core / thick shell, and core@gradient shell.

1.4.3   Quantum Dot Synthesis

Although it is possible to synthesize QDs in a high temperature precipitation from molten precursors, the organic synthesis technique produces much more valuable QDs as they can be recovered as a powder rather than suspended in glass and their surface can also be passivated with organic ligands to aid in solvent dispersion. The ligand passivation is especially important because the surface atoms have many dangling bonds which act as trap states and non-radiative recombination centres to decrease the QD PLQY.[56][76] The standard organic process refined by Murray *et al.* involves size selective precipitation to produce a nearly monodisperse quantum dot product with radius < 10 nm.[63] The organometallic precursor (e.g dimethylcadmium) is dissolved in trioctylphosphine oxide (TOPO), and added to a solution of selenium shot dissolved in trioctylphosphine (TOP) prepared under an inert atmosphere at 300 °C while stirring.[63] The formation of CdSe crystallites leads to a sudden decrease in temperature, which must be increased and maintained at 230 – 260 °C.[63] Homogeneous nucleation of the reagents occurs immediately and the decrease in temperature halts nucleation.[63] Further growth as temperature is increased occurs via Ostwald ripening which is a slow diffusion from small to larger molecules that arises from the instability of high surface energy small particles.[63] As the QDs grow in size and narrow in distribution, the temperature required to maintain growth increases so the final distribution of sizes can be dynamically optimized during the process.[63] Subsequent rinsing with methanol results in TOP / TOPO capped CdSe QDs that can be dissolved in a wide range of organic solvents. Utilization of a more complex combination of surfactants in addition to TOP and TOPO has been successful in improving the PLQY and monodispersity of the resultant QDs.[77]

A second synthesis step can be followed to coat the CdSe core with a wider bandgap semiconductor shell such as CdS, ZnS, or ZnSe to further improve PLQY and exciton confinement to the QD core.[56] This shell overcoating process is essentially a continuation of the QD synthesis while introducing new precursor materials corresponding to the desired shell composition. In order to avoid homogeneous growth of shell-only composition QDs during the reaction, the shell precursors can be added dropwise at low

temperatures.[77] While the organic ligands passivate some dangling bonds, the bulky nature of these ligands means that there will inevitably be some free surface states. Meanwhile, a full overcoat of a wider bandgap material with similar lattice parameter will eliminate CdSe free surface states and the carriers should remain confined within the CdSe core away from the shell surface traps which are also passivated by ligands.[56] Quantum dots with up to 50% PLQY and 40 nm FWHM emission were first reported with core / shell QDs, improving on the 15% PLQY and 50 nm FWHM in the CdSe core-only QDs at the time.[56,63] The use of a ZnS shell leads to better confinement in the core and greater PLQY than CdS due to its larger bandgap, but is ultimately limited by the difference in lattice parameter which is also greater than CdS. As the ZnS shell thickness increases beyond 1.3 monolayers, the PLQY decreases due to an increase in defect density.[56] However, this can be circumvented by the growth of a gradient shell from CdSe to CdS to ZnS which can lead to PLQY nearing 100% and an even narrower emission FWHM while also significantly reducing the effects of photo-oxidation of the CdSe core.[2,66,74] Recent work in high PLQY gradient composition (> 70%)[78] and core/shell/shell (> 95%)[27] QD structures has resulted in good crystallinity and a suppression of blinking along with single-exponential PL decay, characteristic of a reduction in non-radiative recombination mechanism. Interestingly, this has been achieved by conducting the entire reaction at elevated (> 250 ºC) temperatures and in some cases with a higher temperature shell growth. This may be related to post-growth alloying that occurs between core and shell materials that has been observed to occur at high temperatures.[79]

1.5   Electroluminescent QDLED Architecture & Mechanics

A QDLED in its most basic form will consist of the following layers: electrodes which inject holes (anode) and electrons (cathode) into the QDLED, charge transport layers which transport holes (HTL) and electrons (ETL) through the QDLED, and an EML where the holes and electrons form excitons and radiatively recombine to emit photons. Owing to the convention used in OLEDs, an upright QDLED will have the anode as the bottom contact and the cathode as the top contact while and inverted QDLED will have the cathode as the bottom contact and the anode as the top contact, as depicted in **Figure 1.6**. Unlike OLEDs, which have the benefit of complete deposition through thermal evaporation if desired (and is the technique by which commercial OLED displays are fabricated), the QD layer in QDLEDs must be processed with solution-based techniques such as through spincoating, inkjet printing or transfer printing.[2] While beneficial for low-cost products, this can be detrimental to device efficiency and stability.[2,80] The solution processing requirement adds another degree of inconsistency and complexity, imposing limits on the materials that can be used in certain devices as solvent orthogonality must be considered such that underlying layers are not destroyed.[22,80–82]
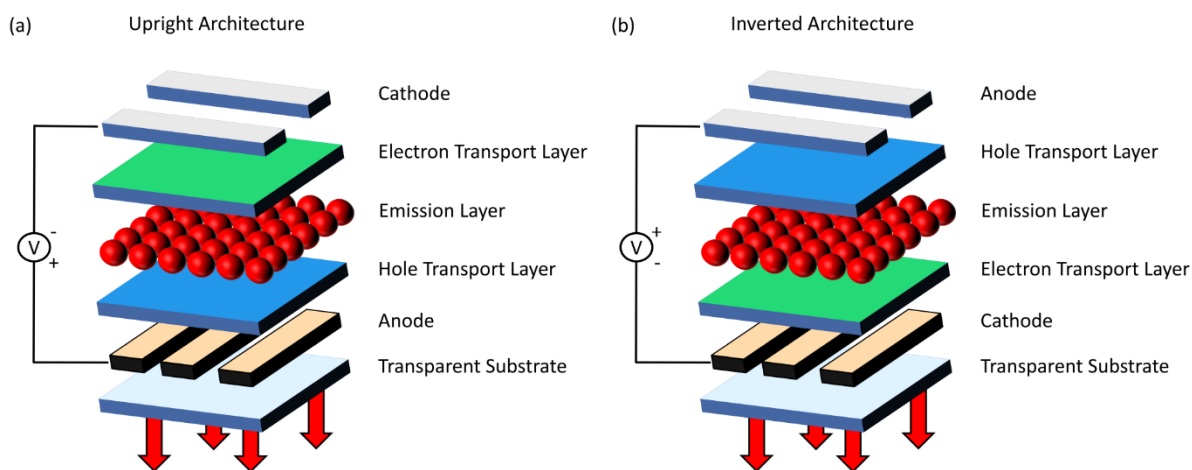
Figure 1.6 Bottom-emitting QDLEDs with (a) an upright and (b) an inverted architecture.

The defining characteristic of LED performance is its external quantum efficiency (EQE), the ratio between photons emitted from the device to the charge carriers injected from the electrodes,[83] as defined by the following equation:

$$EQE = \eta_{rec}\eta_{\text{spin}}\eta_{\text{PL}}\eta_{\text{OC}} \qquad (9)$$

Where η_{rec} is the electron-hole recombination efficiency, η_{spin} is the spin state recombination efficiency, η_{PL} is the PLQY, and η_{OC} is the outcoupling efficiency of the device. The electron-hole recombination efficiency is essentially a charge balance and carrier leakage factor where 100% corresponds to each charge carrier forming an exciton within the OLED, decreasing if one carrier has a higher concentration than the other or reaches the counter electrode without recombining. The spin state recombination efficiency relates to the allowed and forbidden radiative recombination pathways of excitons on a spin-basis. The PLQY is a measure of the competing radiative and non-radiative transition rates of excitons within the emission layer. If the emissive pathways are dominant, then η_{PL} will approach 100%. Although QDs with PLQY upward of 100% have been demonstrated, these measurements do not reflect the PLQY of a QD film where energy transfer of excitons from the core of one QD to surface states on an adjacent QD can increase non-radiative exciton recombination.[2,70] This leads to a reduction in film PLQY by an order of magnitude or more compared to the values measured in solution. The outcoupling efficiency describes the probability that a photon emitted by the QDLED will escape the device. The standard outcoupling factor is assumed to be 20% as derived from ray optics, but recent optical dipole modeling of high efficiency devices has challenged this notion and the outcoupling factor could be as high as 30%.[83,84]

1.5.1 Exciton Formation & Recombination

Unlike the QDs excited by photons in colour conversion films which create excitons via photon absorption, in QDLEDs the injection of electrons and holes directly into the QD conduction and valence energy levels forms excitons via Coulombic attraction to produce EL. While the excitons created by either

method will emit photons with the same energy, only singlet excitons will be created during PL while both singlet and triplet excitons will exist in EL. The distinction between singlet and triplet excitons relates to the exciton's total spin quantum number (s) of the hole and electron states where singlets have $s = 0$ and triplets have $s = 1$.[85] Without perturbation, the radiative recombination of triplet excitons is generally not allowed since the ground state of the transition has $s = 0$ and the transition moment spin overlap integral forbids transitions between spin states (i.e. $\Delta s = 0$). The spin multiplicity of singlets and triplets is defined by the equation $2s+1$, resulting in a ratio of 1 singlet for every 3 triplets. Thus, in a randomly assembled population of excitons where charge carriers are injected with a random spin state (such as in EL QDLEDs), we expect to find that 75% of the excitons are triplets.

However, the distinction between singlet and triplet excitons is not as simple in QDs due to the energy level structure and mixing in the quantum confinement regime. As noted in section 1.2, the lowest energy excitons in a QD will consist of an electron in the 1S state and a hole in the $1S_{3/2}$ state. The lowest energy exciton in a QD is a forbidden "dark" state according to the fine structure of band-edge exciton states in QDs. The fine structure arises from several factors such as crystal field effects which split the light and heavy hole band energies, deviations from spherical shaped QDs, and electron-hole exchange interactions.[5,40–42] The electron-hole exchange, which represents the different total spins of excitons, is what results in the "dark" exciton state.[40–42] An exciton consisting of a $|j_m| = 1/2$ hole and spin 1/2 electron results in 2 states with total angular momentum $N_m = 0$ (referred to as 0^L and 0^U, for lower and upper energy states with the same total angular momentum) and 2 states with $|N_m| = 1$ (1^U).[40–42,86] An exciton consisting of a $|j_m| = 3/2$ hole and spin 1/2 electron results in 2 states with total angular momentum $|N_m| = 2$ and 2 states with $|N_m| = 1$ (1^L).[40–42,86] The lowest energy exciton state corresponds to $|N_m| = 2$, which is not optically active as the transition is forbidden by the electric dipole approximation and cannot undergo relaxation by a single photon.[40–42,86] The next lowest energy state is 1^L which is optically active and referred to as the "bright" exciton.[42] These two exciton states are the most important for their application in EL QDLEDs and the energy difference between these two states (Δ_{db}) can be related to the rate of radiative recombination and

PLQY of the QDs as a smaller energy difference will allow for easier thermalization of excitons from the "dark" state to the "bright" state.[5] Effectively, at sufficiently high temperatures (such as the room temperature operation of EL QDLEDs), all excitons should be capable of recombining radiatively.[5] However, it should be noted that the bright-dark splitting increases as QD size decreases so this is not necessarily the case for sufficiently small QDs.[42] The other exciton states discussed earlier are valuable for understanding and utilizing the absorption spectra of QDs for many other applications.

Ideally, all excitons will recombine radiatively resulting in a PLQY of 100% but in reality this is not necessarily the case. Whereas both singlet and triplet excitons may eventually recombine radiatively, there are several processes that can lead to non-radiative recombination via energy transfer of the exciton or charge transfer to a quencher such as surface defect sites and dangling bonds or exciton-phonon interactions.[40,63,87,88] These states may arise due to lattice mismatch stresses in the QDs which result in voids or dislocations in the crystal structure, and dangling bonds will be present at the surface facets of the QDs. The surface states are more detrimental in homogeneous core-only QDs where the exciton is confined close to the defect site. All these non-radiative recombination mechanisms should equally affect EL and PL QDLEDs, but it is the presence of charge carriers as well as excitons that complicates exciton recombination in EL QDLEDs in comparison to PL QDLEDs. Fluctuations between "on" and "off" states in the PL intensity over time known as blinking have been a significant issue of interest for researchers in the field as the process limits the PLQY of QDs.[5] In this case, the on state corresponds to a bright exciton that radiatively recombines and the off state corresponds to a dark state that recombines non-radiatively. This property has been attributed to non-radiative relaxation of excitons in negatively and positively charged QDs, referred to as a trions, where the positive trions generally have a faster decay rate and are therefore less likely to emit a photon.[4,5,89–94] The performance of charged QDs are of particular interest for EL QDLEDs since the injection of charge carriers makes the eventual charging of QDs inevitable.

Auger recombination is one such non-radiative recombination process where an exciton recombines and transfers the resultant energy to a third charge carrier (either a hole or an electron) which can

21

significantly impact QD luminescence. The rate of Auger recombination in bulk semiconductors has an inverse exponential relationship to temperature and increases exponentially with increasing band gap.[5] However, the Auger process is more efficient in QDs compared to their bulk counterparts due to their strong Coulomb electron-hole coupling and the relaxation in momentum conservation in atomic systems, which results in a significant and progressive reduction in the energy barrier for the Auger recombination process as QDs volume decreases.[94–99] The Auger decay rates in QDs are often much faster than the radiative decay rates, resulting in significant reductions in the PLQY of charged QDs. Therefore, it is important to reduce the influence of Auger recombination for high performance EL QDLEDs using methods such as compositionally engineered gradient QD structures and surface passivation with organic ligands.

1.5.2   Charge Injection & Transport

Charge carrier injection between the individual layers and into the EML especially is a critical parameter to consider in the design of QDLEDs. The very deep energy levels of CdSe QDs make this consideration perhaps the most critical as it puts severe constraints on the electrical properties of the transport layers. Owing to the previous work on OLEDs as well as the constraints put on the device structure due to the low temperature and solution-based deposition of the QD layer, amorphous and molecular semiconductor films are generally used as the transport layers in QDLEDs. A red CdSe core-only QD should have a conduction band around 4.5 eV below the vacuum energy level (conventionally written as -4.5 eV) and a valence band around -6.5 eV, both of which are much deeper than typical lowest unoccupied molecular orbital (LUMO) energy levels of organic ETLs and highest occupied molecular orbital energy (HOMO) energy levels of organic HTLs.[2] This results in favourable electron injection into the CdSe with little to no energy barrier, but a large barrier inhibiting hole injection. There are several equations that have been developed to model carrier injection between two energy states such as Fowler-Nordheim tunneling, Richardson-Schottky thermionic emission, drift-diffusion and multiple trapping theory, and analytical methods, each with their own dominant regimes regarding material choice and properties.[100–104] However,

the injection efficiency generally follows an exponential relationship to energy barrier and electric field where minimal energy barriers and greater electric fields promote carrier injection across an interface. The barrier to carrier injection between 2 adjacent layers is related to the difference in energy levels from the donor molecule to the acceptor molecule. In a QDLED, the QD EML is thus expected to be very electron-rich, disrupting charge balance in the emission layer. The built-up charges in the QDs can be detrimental to both efficiency and stability.[2] For green and blue QDs, both conduction and valence band energy levels increase which can further exacerbate the difficulty of carrier injection. Further, by utilizing core / shell (or core@shell) QDs with a wider band gap shell material (such as CdS or ZnS) and organic ligands which are generally wide band gap insulating materials, the distance between charge donor and acceptor molecules increases in addition to the larger energy barrier inhibiting charge injection.

In bulk semiconductors, carrier transport occurs via band transport where the very small interatomic distances (< 3 Å) and strong molecular interactions between atoms form a continuous conduction and valence band as illustrated in **Figure 1.7**(a). This allows for a rather uninhibited movement of charge carriers between atoms, with electron (μ_e) and hole (μ_h) mobility values typically greater than 100 cm^2 V^{-1} s^{-1} which can be described by several carrier scattering mechanisms.[101] For molecular semiconductors, the HOMO energy level can be considered as the valence band equivalent where the highest energy bound electrons reside and can be excited to the LUMO which can be considered as the conduction band equivalent.[101] However, since the HOMO and LUMO are not actually continuous bands and in most cases organic semiconducting thin films are amorphous, the movement of charge carriers is much different than the band transport observed in crystalline semiconductors. The molecular disorder, diverse intermolecular bond strengths, and poor wavefunction overlap in amorphous films results in a Gaussian distribution of the density of states as depicted in **Figure 1.7**(c), ultimately leading to a hopping transport mechanism between molecules as opposed to band transport.[101] Here, hopping is essentially the tunneling (or injection) of charge carriers between molecules with a Gaussian distribution of energy levels as described by the following Gaussian disorder model equation:

$$\mu(F,T) = \mu_\infty \exp\left[-\left(\frac{2\sigma}{3k_BT}\right)^2\right]\exp\left(\beta\sqrt{F}\right) \tag{10}$$

$$\beta = C\left[\left(\frac{\sigma}{k_BT}\right)^2 - \Sigma^2\right] \tag{11}$$

Where T is the absolute temperature, F is the electric field over the space of interest, k_B is the Boltzmann constant, μ_∞ is the high temperature limit of mobility and the constant C is 2.9×10^{-4} cm$^{1/2}$ V$^{-1/2}$.[101] The material dependent variables in the equation are the positional disorder (Σ) of the molecules in the amorphous thin film and the disorder in energy levels (σ), which can be rationalized as the width of the Gaussian distribution of states.[101] While still dependent on the electric field applied across the film, the hopping transport mechanism is inherently much slower than band transport, with typical good amorphous materials exhibiting carrier transport values on the order of 10^{-3} cm^2 V^{-1} s^{-1}.[101] More often than not, organic films will have either a dominant hole transport or electron transport character although it is possible to have bipolar transport as well.[101] It is feasible to improve electron transport to 10^{-3} cm^2 V^{-1} s^{-1} but there is a trade-off in device stability due to poor morphology of these films.[101] Charge transport through inorganic semiconductor nanoparticle and QD films generally follows the hopping mechanism as well since charge carriers must move from one discrete nanoparticle to the next with localized charge carrier wavefunctions, disorder in their energetic states, and distances between the donor and acceptor similar to that of the organic molecular films.[100] However, the dependence of mobility on carrier density dominates for inorganic films that have been highly doped. Ultimately, the electron and hole density in QDLEDs should be balanced to avoid a build-up of charges leading to the non-radiative recombination pathways discussed in section 1.5.1 and to maximize device efficiency.
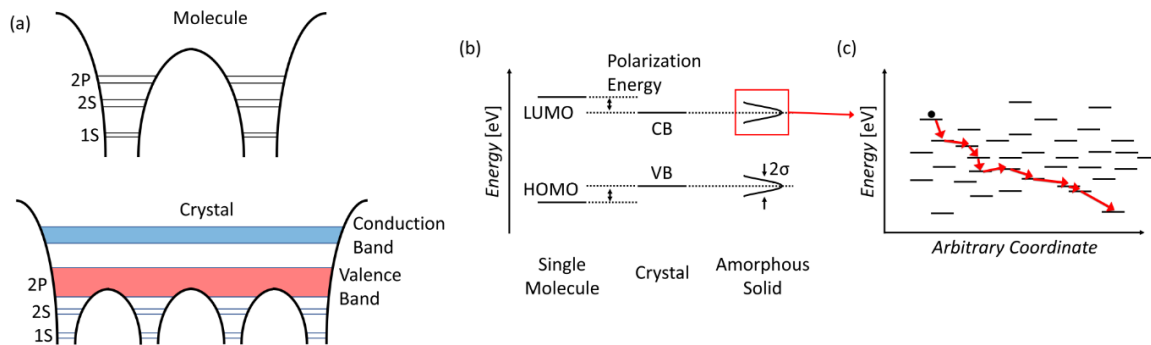
Figure 1.7 (a) The basis for the formation of conduction and valence bands in periodic crystals as opposed to molecules. The energy of the highest state occupied by bound electrons is split and shared by each atom without a potential energy barrier. (b) The difference in LUMO (conduction) and HOMO (valence) state energy and distribution for single molecule, ordered crystal, and amorphous films. (c) A pictorial representation of what a Gaussian distribution of amorphous energy bands would look like in an arbitrary direction with respect to charge transport.

1.5.3   Upright *vs.* Inverted Architecture

Owing to the convention used in OLEDs, there are two devices architectures which are depicted in

Figure 1.6: the upright structure where holes are injected from the bottom electrode deposited on the

substrate and electrons are injected from the electrode deposited on top of the device stack and an inverted

structure where electrons are injected from the bottom electrode and holes are injected from the top. Each

architecture has sub-types designating the electrode from which light is emitted, either top-emitting or

bottom-emitting.

In QDLEDs, the transport layer material selection process is the main factor in determining the

architecture and deposition sequence of the device. Indium tin oxide (ITO) is a very popular transparent

conductive electrode material allowing for light emission from the QDLED with low resistivity, but its high

processing temperature (> 300 ºC) requires deposition on the transparent glass substrate to avoid thermal-

induced damage of the rest of the QDLED layers.[105,106] Due to the requisite solution-based deposition of

the QD EML, the underlying transport layer must be resistant to whichever solvent is used. Small molecule

organic transport layers are notably susceptible to damage from solvent exposure, limiting their use as the

first transport layer. It is more common to use polymer and inorganic transport layers deposited by a

solution-based process which are resistant to subsequent solvent treatments. The transport layer deposited on top of the QD layer may be solution-based or evaporated, opening up the material selection to small molecule organic transport layers. The final layer is the counter electrode, generally a reflective metal due to their superior conductivity, but may be transparent in the case of a top-emitting device. HIL and EIL layers may be deposited between the electrodes and their corresponding transport layers to improve charge carrier injection, reducing the device driving voltage and improving its efficiency.

The conduction and valence energy states of CdSe-based QDs are very deep in comparison to the typical transport layers used for many OLEDs. The valence energy states of organic and inorganic transport layers generally lie between -5 eV to -6 eV. Thus, materials with deeper energy levels are favoured in order to improve hole injection into the QD EML. ITO has a work function of -4.7 eV, which better aligns with the deep energy states of these HTLs in comparison to the commonly used Al counter electrode (-4.3 eV).[107] Therefore, deposition of the HTL on top of the ITO electrode should facilitate improved hole transport through the QDLED which is one of the reasons that the upright architecture currently dominates high performance QDLED structures in literature.

1.5.4 Degradation Mechanisms

Given the similarity in fabrication process and materials used between OLEDs and QDLEDs, we can expect that many of the degradation mechanisms of OLEDs can be extended to QDLEDs. Beginning with the first OLED studies, stability was identified as a major hurdle to overcome in commercial devices.[14,108] These degradation mechanisms can be classified in two categories: intrinsic degradation and extrinsic (or ambient) degradation.[13,14] The ambient degradation mechanism was the first one to be identified as a possible problem for OLEDs and can be considered an environmental moisture and oxygen contamination, interaction, or reaction with the various components in the devices.[12,14] Extrinsic degradation typically induces the formation of dark spots in the emissive area which grow larger over time with or without a bias

applied to the device. Oxidation and corrosion of the top electrode (in contact with air) was initially determined as a leading source of ambient degradation as delamination of the electrode from the underlying organic layer occurs due to the evolution of gas, reducing the contact area and decreasing carrier injection.[12–14] However, improving the metal-organic interface alone does not solve the ambient degradation issue as most organic semiconductors are also sensitive to moisture and oxygen and can easily crystallize.[12–14] While a crystallized organic domain can have higher carrier mobility, the inhomogeneous mobility across the layer will lead to non-uniform emission as certain areas will have preferential transport and injection. Furthermore, the change in morphology can also lead to dark spot formation as voids or shunts in the organic layers arise.[12–14] Thankfully, extrinsic degradation can be avoided in modern devices through encapsulation to isolate the OLED from atmospheric gases.

Degradation studies have shifted toward the intrinsic mechanisms which have proven to be more challenging as the dominant mechanism can depend on the particular materials used in the device. There have been several intrinsic degradation processes suggested in literature including charged molecules, chemical degradation and morphological changes within the thin films.[13,14] One of the first intrinsic degradation methods to be discovered is the instability of cationic tris-(8-hydroxyquinoline)aluminium (Alq$_3$) species which, since it is an ETL, occurs in the event of hole leakage past the exciton formation area.[13,14] It is clear from this mechanism that charge balance is an important factor in preserving device lifetimes. For QDLEDs in particular, charge imbalance is very difficult to resolve and Auger recombination resulting from this charge imbalance is commonly recognized as a source of degradation.[2,22–29] Although molecular instability due to ionic species is not seen in all molecules, the accumulation of charges is inevitable at interfaces with a barrier to injection.[13,14] The accumulated charges can recombine with mobile charges or excitons via energy transfer to dissipate energy non-radiatively.[13,14] This progressive degradation in luminance over time is attributed to the formation of trap states during current flow through the device. The depressed energy gap, particularly in deep trap states, leads to higher rates of internal conversion and undesirable emission.[13,14] One source of the trap states is chemical degradation by bond dissociation as a

result of the additional energy of excited state excitons on a particular atom, effectively acting as quenching sites.[13–15] The energy required for carbon-nitrogen bond dissociation is approximately equal to the singlet excited state energy in many organic semiconductors so it follows that the degradation of these materials may be dependent on exciton density.[14,15] Due to the long-lived triplet exciton lifetime, a bimolecular degradation process between triplets and polarons (a charged molecule that induces a dipole in the surrounding molecules that leads to partial screening of the charge) can lead to significant degradation whereas the introduction of only excitons or only charge carriers is negligible in some cases.[16–19] This exciton-polaron interaction was found to induce irreversible aggregation of the organic molecules with a correlation to increasing bandgap energies.[16–19]

Degradation of QDs themselves can occur through several avenues such as photo-oxidative bleaching, charging, and formation or exposure of surface trap states and dangling bonds. With the exception of charging, these degradation mechanisms more strongly affect core-only QDs as the charge carrier wavefunction may interact with the surface states. Photo-oxidative bleaching is an exciton-mediated process where energy transfer to oxygen adsorbed on the QD surface may cause oxidation. This results in a reduction in QD size and produces a blue-shift in the emission spectrum over time, but also a reduction in PLQY as the oxidized surface may quench excitons.[56,67,88,109] However, the core / shell (and core@shell) QD structure confines excitons to the QD core so degradation of the shell's surface will have less of an impact on exciton recombination, especially so for thicker shells. Although PL stability was an issue for early QDs, QDs have now demonstrated exceptional PL stability under constant illumination of 150 mW cm^{-2} blue light in accelerated aging tests corresponding to at least 100,000 hours with negligible degradation, much greater than many organic transport layers.[110] However, charging QDs can be a significant source of PLQY loss in core / shell QDs. As discussed in section 1.5.2, the non-radiative recombination process in positive and negative trions is much faster than the radiative recombination of excitons. Thus, excitons in charged QDs are more likely to undergo non-radiative (Auger) recombination

28

as evidenced by the "on"-"off" state switching referred to as blinking. This degradation mechanism is generally suspected to be the main limiting factor of QDLED stability.[22,23,113,24–26,81,82,88,111,112]

The EL stability of QDLEDs is quantified by measuring their EL intensity over time while driven at a constant current. The most commonly used metric corresponds to the time it takes to decrease to 50% of the initial luminance (LT50), although other degradation points such as 90% of the initial luminance (LT90) are not uncommon. Since the rate of degradation depends on the device's initial luminance, the initial luminance should be the same if accurate comparisons between the degradation rates of different QDLEDs are to be made. There is however a relationship between the degradation point at two different initial luminances of a device that can be described by the following equation:

$$(L_a)^n LT[X] = (L_b)^n LT[X] \qquad\qquad 1 < n < 2 \qquad\qquad (12)$$

Where L_a and L_b are two different initial luminance values for the lifetime measurement, n is the exponential luminance dependence of device decay, and $LT[X]$ is the time it takes for the device luminance to degrade from the intial value to $X\%$ of the initial value.[114] Using this relationship, as long as the degradation point is maintained, the degradation time of any given device can be estimated for any initial luminance after empirically determining the acceleration factor, n, with several independent measurements. While this method is common practice and essential to avoid long testing times, the results are often skewed since the factor n is not precisely known and merely estimated since it is highly material dependent. For QDLEDs, a commonly calculated value for n is 1.8 but since this acceleration factor depends on QD composition and device architecture there are deviations from this number among different devices and for different colour QDs.[28,78,115,116] The standard lifetime measurement used in literature to compare between different devices is a LT50 carried out at any initial luminance that is then converted to the equivalent LT50 for an initial luminance of 100 cd m^{-2}. Although greater initial luminance values may be more appropriate for modern device applications, the 100 cd m^{-2} benchmark has continued from its use in early device stability studies. The convention in this work will refer to the LT50 reported for (or converted to) an initial luminance of 100 cd m^{-2} unless otherwise specified.

Chapter 2: A Brief History of QDLED Performance

Some of this review has been published in Davidson-Hall, T. and Aziz, H., Appl. Phys. Lett., vol. 116(1), pp. 010502, 2020. It has been reproduced with permission from the publisher.

Since the first QDLED introduced in 1994 by Colvin *et al.* there has been a significant improvement in both performance and lifetime of the devices rivaling some of the benchmark high performance OLEDs.[117] Initially devised as a bilayer structure comprising the CdSe core-only QD layer and an organic HTL sandwiched between ITO and metal (usually Al) electrodes, the EQE of the first QDLED was < 0.01%.[117] Meanwhile, the first report of QDLED EL lifetime found their 0.1% EQE devices to have a LT50 of 11 hours.[118] It was not until zinc oxide (ZnO) was introduced as the ETL in 2008 that massive gains in EQE and lifetime were made.[119,120] In the last decade alone, significant leaps in both QDLED efficiency and lifetime have been demonstrated as shown in **Figure 2.1** below. With improvements in QD design and QDLED structure, devices with maximum EQE values of up to 30.9%,[27] 25.0%,[121] and 19.8%[122] for red, green, and blue devices as well as LT50s of 2,260,000 hours,[115] 1,760,000 hours,[28] and 32,705 hours[26] for red, green, and blue QDLEDs have been reported in literature. Aside from the progress in QD design and synthesis as detailed in the previous sections, there has also been an evolution in QDLED architecture and material choice. This chapter will present a review of the evolution in QDLEDs that has led to these improvements, concluding with the motivations and objectives of this work.
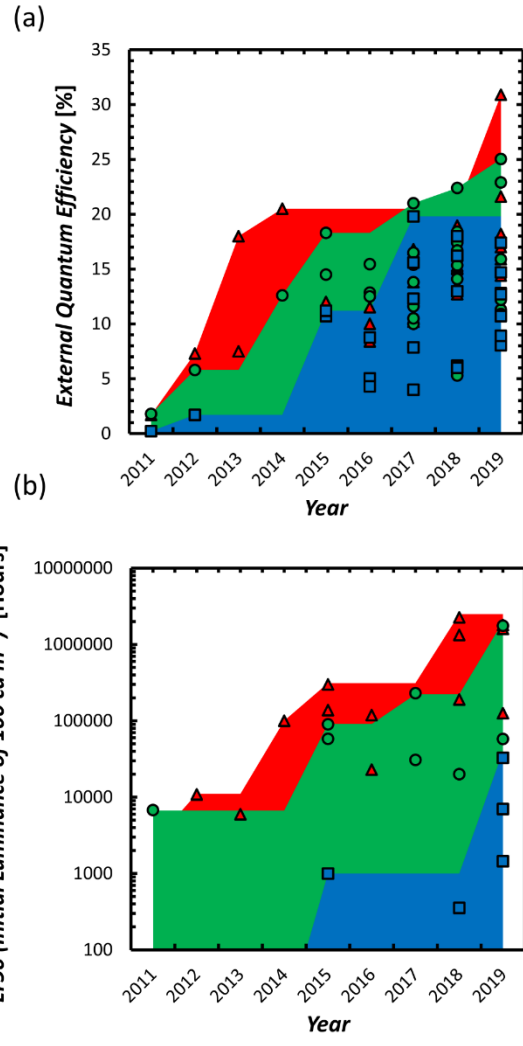
Figure 2.1 (a) EQE and (b) LT50 (for an initial luminance of 100 cd m^{-2}) metrics reported in literature since 2011 for red (triangle),[22,23,115,116,123–130,24,131–140,25,141,26–28,78,81,82] green (circle),[22,23,126,129,131,132,134–136,139,141,142,24,143–152,25,26,28,70,81,121,125] and blue (square)[22,23,122,125,126,129,131,132,134,136,139,141,24,149,153–156,26,28,51,52,54,55,81] electroluminescent QDLEDs. References for devices with record EQE and LT50 values are included beside the data point. Where LT50 values are unavailable for a 100 cd m^{-2} initial luminance, the LT50 values at the provided initial luminance have been converted to an equivalent value using the lifetime relation of $L_0^n LT50 = L_1^n LT50$ where n is the acceleration factor of 1.8 frequently calculated for QDLEDs.[28,78,115,116]

31

2.1   1994-2005: Core-Only and Core / Shell QDs with Organic Transport Layers

The first QDLED was a bilayer structure comprising the QD layer and a poly(p-phenylenevinylene) (PPV) organic HTL sandwiched between ITO and Mg electrodes with an EQE of < 0.01%.[117] The QDs in this work were red-emitting with a peak emission of 612 nm. These QDs are larger in size than green or blue QDs, resulting in narrower size distribution with a greater ratio of core to surface states and were generally more stable with greater PLQY at the time. Both upright and inverted structures were investigated, but the upright structure demonstrated superior efficiency and a lower turn-on voltage due to better energy level alignment between the ITO work function (-4.7 eV) and PPV HOMO energy level (-5.1 eV) as well as Mg work function (-3.7 eV) and CdSe conduction band. The EL spectra of these devices had a significant contribution from both the QD layer and the PPV molecules indicating that excitons were being formed in both layers, although the emission shifted toward PPV-dominance at higher driving voltages. This was an early indication that injection of holes into the QD layer would become an issue for QDLEDs. At the time, CdSe core-only QDs had solution PLQY < 15% due to uninhibited surface state quenching.[56,63] Metals are also strong exciton quenchers due to a combination of energy transfer to and exciton dissociation at the metal interface.[157,158] These factors likely contributed to the poor efficiency of these devices.

At the same time as the initial QDLED experiments, devices utilizing CdSe QDs embedded in a mixture of poly(vinylcarbazole) (PVK) HTL and 2-(biphenyl-4-yl)-5-(4-tert-butylphenyl)-1,3,4-oxadiazole (t-Bu-PBD) ETL between ITO and Al electrodes were being studied by Dabbousi *et al*.[159] The QD contribution to the EL emission spectra in these devices was much greater, serving as trap sites in the carrier conduction through the HTL:ETL composite or receiving excitons via energy transfer from the composite. However, the improved colour purity of the QDLED emission did not translate to improved efficiency as the devices had an EQE of 0.0005%. Early QDLED work by Schlamp *et al*. addressed the PLQY issue of core-only QDs by utilizing CdSe / CdS core / shell QDs in the same device architecture as Colvin *et al*. with optimized layer thicknesses to achieve an EQE of 0.22%.[109] However, poor carrier mobility of the

QDs coupled with metal quenching ultimately limited the device performance. While Mattoussi *et al*. were not able to surpass the EQE of the CdSe / CdS QDLEDs, their devices with CdSe / ZnS QDs and the same transport layers resulted in a maximum EQE of 0.1% but were somewhat stable with a LT50 of 11 hours.[118]

The next innovation in QDLED structure was introduced by Coe *et al*. in 2002 with an EQE of 0.52%, realized by utilizing neat HTL and ETLs on either side of a single monolayer of CdSe / ZnS QDs (and similar to the structure depicted in **Figure 1.6**) instead of a composite layer.[160] N,N'-diphenyl-N,N'-bis(3-methylphenyl)-(1,1'-biphenyl)-4,4'-diamine (TPD) was first spincoated on ITO, improving hole injection into the QDs due to its deeper HOMO energy level (-5.4 eV) compared to PPV. The spectral overlap of TPD emission with the QD absorption was noted at a benefit as excitons created in the HTL may undergo FRET to the QD layer. Meanwhile, Alq$_3$, a green-emitting ETL commonly used in red fluorescent OLEDs, was used to minimize the contribution of the QD layer to charge transport through the device and move the EML away from the cathode to reduce metal quenching. There was a significant green peak in the emission of these QDLEDs due to holes bypassing the QDs and injecting into the Alq$_3$ layer since the EML was only one monolayer thick. Introducing a thin 3-(4-biphenylyl)-4-phenyl-5-t-butylphenyl-1,2,4-triazole (TAZ) hole and exciton blocking layer was successful in confining excitons to the QD layer, but this device was less efficient with an EQE of 0.3%. A similar structure was used to demonstrate the first QDLEDs utilizing green-emitting QDs with a peak EL wavelength of 540 nm the following year with EQE < 0.5%.[161] The EQE of their red QDLEDs improved to 1.1% and then to 2.0% in 2005 by improving upon their fabrication processes to create high quality QD monolayer EMLs with sufficient uniformity to eliminate emission from the organic transport layers that arose from voids in the prior QD films.[162] Hikmet *et al*. demonstrated a comparable efficiency in 2005 with rod-shaped CdSe / CdS QDs between a PVK HTL and a 1,3,5-tris(2-N-phenylbenzimidazolyl)-benzene (TPBi).[163] The rod-shape of these QDs are attractive for QDLEDs because if they are deposited in such a way to align their optical dipole perpendicular to the plane of emission not only can the outcoupling efficiency of the device can be improved significantly, but the light can be polarized as well.

2.2   2006-2012: Red, Green and Blue QDLEDs with Inorganic and Organic / Inorganic Hybrid Transport Layers

Although successful in producing EL from QDs, QDLEDs with all-organic transport layers could not reach efficiencies observed in OLEDs which by 2006 had exhibited EQEs of up to 19% due to the advent of phosphorescent emitters capable of 100% spin state recombination efficiency.[164] The PLQY of the QDs was still low at the time as synthetic methods were still being developed and optimized. The degradation of the organic layers was also identified as a likely source of the limited lifetime of the QDLEDs due to ambient instability of the OSCs and organic / metal contacts. However, in the ensuing years, QDLED performance would ascend to levels comparable to OLEDs and devices with smaller size QDs (with green and blue emission) emerged capable of realizing full-colour QDLED displays.

Anikeeva *et al*. found that EQE could be improved by 1.5× (to a value of 2.3%) for red CdSe / ZnS QDs embedded in an organic TPD HTL. By reducing the QDs exposure to charge carriers, they are less likely to become charged and undergo non-radiative Auger recombination. In such a structure, the QD emission then requires efficient energy transfer from the HTL. This was the main mechanism by which it was believed that organic transport layers were superior to inorganic transport layers in achieving high performance QLDEDs. Work by Zhang *et al*. elaborated upon this mechanism, showing that green QDLED efficiency could be improved by 2.5× (to a value of 0.55%) by doping bis(4,6-difluorophenylpyridinato-N,C2)picolinatoiridium (FIrpic), a blue organic phosphorescent emitter, into the HTL at the QD / HTL interface.[165] This system is able to capture both singlet and triplet excitons that form on the 4,4'-N,N′-dicarbazole-biphenyl (CBP) HTL via energy transfer to the FIrpic emitter since CBP's triplet energy level is similar to that of FIrpic. This then allows for FRET of both singlet and triplet excitons to the QD layer due to the favourable overlap between FIrpic emission and the CdSe / ZnS QD absorption spectra. Without efficient triplet emission from the HTL, these excitons (i.e. 75% of total excitons) would only be transferable through the very short-range Dexter transfer. Although this device structure did not set the

34

standard for QDLED architecture, it demonstrates the potential contribution of energy transfer from the organic layers to QD EL in these devices.

A green all-organic transport layer QDLED was reported by Steckel *et al.* in 2006 with a maximum EQE of 0.5%. By synthesizing alloyed QDs with the structure $Cd_xZn_{1-x}Se$ / $Cd_yZn_{1-y}S$, larger QDs could be made with wider band gaps as the alloyed core had a band gap between that of CdSe and ZnSe corresponding to the alloy ratio. In an optimization of device structure and QD composition, Anikeeva *et al.* designed devices spanning the entire visible spectrum with many of the devices reaching record efficiencies, blue (0.4% EQE) and green (2.6% EQE) in particular.[166] This optimization took into account both charge injection issues and FRET from the organic layers. For red and orange devices, the green emitting Alq_3 ETL was used. Alq_3 would absorb light emitted from blue QDs so it was replaced with TPBi in those devices. Meanwhile, spiro-N,N′-diphenyl-N,N′-bis(3-methylphenyl)-(1,1′-biphenyl)-4,4′-diamine (Spiro-TPD) was used as the HTL due to its high glass transition temperature of 102 ºC which imparted better morphological stability over TPD (65 ºC) with a band gap wide enough for suitable FRET to all QD colours.

In 2006, Caruge *et al.* investigated sputtered p-type nickel oxide (NiO) as an inorganic alternative to the organic HTLs commonly used up to that point with a red CdSe / ZnS EML and Alq_3 ETL.[167] Quenching of QD EL by the high free charge carrier density of metal oxides was noted, finding that resistive NiO thin films quenched QD excitons less than conductive NiO films. The valence band of NiO is -6.7 eV which should significantly improve hole injection into the QDs in comparison to the organic HTLs noted earlier. However, the HOMO energy level of Alq_3 is only -5.8 eV so holes can be easily injected from the QD layer to the ETL in this device structure. The authors observed a significant contribution of Alq_3 emission for driving current densities of up to 3 A cm^{-2}, a value significantly higher than all-organic QDLEDs were capable of sustaining. Ultimately, these devices achieved maximum EQEs of only 0.18% but the concept of inorganic transport layers was intriguing to QDLED researchers. Building upon this work, the authors then replaced the ETL with a sputtered zinc tin oxide (ZTO) alloy in 2008 to create a completely inorganic

QDLED.[120] ZTO was chosen as the ETL material for its deep conduction (-4.3 eV) and valence (-7.7 eV) band energy levels, enabling good electron injection into the QDs and a barrier to hole injection from the EML to the ETL. This device structure was similarly capable of being driven with current densities of up to 3.5 A cm^{-2} but achieved a maximum EQE of only 0.1%, albeit with ZnCdSe alloyed core-only QDs with a reduced PLQY. At the same time, Stouwdam *et al*. also reported on their findings utilizing ZnO as an inorganic ETL in CdSe / ZnS QDs but with an organic PVK HTL.[119] Rather than deposition by sputtering, the ZnO film was also spin-coated from a nanoparticle suspension. Blue (CdSeS / ZnS) and green (CdSe / ZnS) QDLEDs were also fabricated with the same device structure although less efficient as a result of their lower PLQY. Perhaps discouraging since these devices initially performed worse than their all organic counterparts, ZnO would soon become the benchmark ETL in QDLEDs.

The hybrid QDLED architecture where one organic transport layer (typically the HTL) and one inorganic transport layer (typically the ETL) began to establish itself in 2011 as the work by Qian *et al*. showed that not only could they reach EQEs comparable to the all-organic transport layer devices but that this new structure may result in longer EL lifetimes.[81] With an upright structure consisting of a poly(N,N′-bis(4-butylphenyl)- N,N′-bis(phenyl)benzidine) (poly-TPD) HTL and a ZnO ETL, EQEs of 1.7%, 1.8%, and 0.22% were reported for red, green, and blue QDLEDs. The inorganic transport layers typically have one or more orders of magnitude higher mobility than organic layers so it seems counterintuitive for this switch to improve performance when electron injection into the QDs is already very easy and electron charging is considered detrimental to both efficiency and stability. In these devices, the turn-on voltage for luminance was found to be below that of the photon voltage (i.e. band gap) of the QDs which is another puzzling result given the significant barrier to injection from poly-TPD with its HOMO energy level of -5.2 eV. The authors attribute this low turn-on voltage to the greater charge imbalance as interfacial excitons result in Auger recombination-assisted hole injection. Therefore, increasing the electrons accumulating at the QD / HTL interface leads to an increase in the Auger-assisted hole injection. This study also reported the most stable QDLEDs to that point, with an LT50 of 270 hours at an initial luminance of 600 cd m^{-2}. The

35 nm thick ZnO layer deposited on top of the QD layer served as a barrier to moisture and oxygen diffusion through the device to the more sensitive QD and organic layers. In an inverted structure utilizing ZnO as the ETL and CBP as the HTL, Kwak *et al*. demonstrated far superior performance in red, green, and blue QDLEDs with EQEs of 7.3%, 5.8%, and 1.7%, respectively.[23] The main factor leading to such an improvement in these devices is the deep HOMO energy level of CBP (-6.0 eV) providing the best match to the QD valence band of any commercially available HTL. An investigation into QDLED performance as a function of HTL HOMO energy level was conducted, finding that EQE generally increased as the HOMO became deeper as one may expect. The QDs themselves were also optimized as the red had a double shell CdSe / CdS / ZnS structure, green had a CdSe@ZnS gradient shell structure, and blue had a $Cd_{1-x}Zn_xS@ZnS$ gradient shell structure all with PLQY > 70%. The red QDLED also exhibited very good EL stability with a LT50 of 600 hours with an initial luminance of 500 cd m^{-2}. In comparison, the upright structure with the same transport layers was much more unstable with a LT50 of just 1.5 hours which contradicts the earlier notion that the stability enhancement is a result of the environmental passivation effect. Rather, the authors of this work attribute the improved stability to an improvement in charge balance within the devices.

2.3   2013-2019: Gradient Composition QDs, Hybrid Transport Layers, and Interface Engineering

Although the QDLED device structure and transport layer choice has not changed much from the hybrid architecture since 2012, it is this period of time over which the greatest improvements in efficiency and EL stability have been demonstrated. Recently, further optimization of synthesis processes have been able to produce red and green gradient composition QDs with PLQY approaching 100% that minimize the rate of Auger recombination. QDLEDs incorporating these QDs have EQEs of up to 30.9%,[27] 25.0%,[121] for red and green devices, respectively, and LT50s of 2,260,000[115] and 1,760,000[28] hours which compare favourably to state-of-the-art OLEDs. While blue QDLEDs lag behind their OLED counterparts, the 19.8% maximum EQE[122] and 32,705 hour LT50[26] is encouraging for future developments.

The first high efficiency QDLED was reported in 2013 by Mashford *et al*. with an EQE of 18% for CdSe / CdS QDs in the inverted hybrid structure with ZnO and a 2,2′,7,7′-tetrakis[N-naphthalenyl(phenyl)-amino]-9,9-spirobifluorene (spiro-2NPB) HTL.[82] The HOMO energy level of spiro-2NPB is -5.5 eV, shallower than that of CBP, so the high efficiency of this device is somewhat surprising especially since the authors do not address this aspect of the QDLED. Instead, the back transfer of trapped charges on the QD EML to the ZnO ETL was found to occur in these devices and believed to be one of the reasons for the significant improvement in EQE and EL stability. Following this work, Dai *et al*. demonstrated 20.5% EQE red QDLEDs with thick-shelled CdSe / CdS QDs (> 90% PLQY) with a LT50 of 100,000 hours.[124] While ZnO was used as the ETL and poly-TPD and PVK were used as a bilayer HTL, the breakthrough in this device structure was the incorporation of a wide bandgap insulating polymer poly(methyl methacrylate) (PMMA) at the interface between ZnO and the QD layers in an upright architecture. The PMMA layer reduces the roughness of the underlying QD layer, acts as a barrier to electron injection from ZnO to improve charge balance, and reduces the quenching of excitons in the QD layer by ZnO. These results highlight the powerful impact of the interfaces within the QDLED on overall device performance. However,

these results conflict with the previous high efficiency QDLED as blocking the back transfer of charges from QDs to ZnO seems to improve these devices. The ZnO layer was also very thick (150 nm) which further impedes electron transport, but also provides a thicker barrier to oxygen and moisture-induced degradation of the underlying layers. The crystal structure thick shell was notably important as well, as when the authors utilized thin shell wurtzite (as opposed to zinc blende) CdSe / CdS QDs with the same transport layers the maximum EQE of these devices was 4.7%. While moving the QD layer away from the electrodes through the introduction of the ETL has led to an improvement in QDLED efficiency by reducing metal-induced exciton quenching, ZnO itself also has a propensity to quench excitons in the QD emissive layer albeit with a quenching efficiency less than many other inorganic transport layers. Inspired by the previous work with PMMA, considerable work has been done to passivate the ZnO / QD interface with wide band gap insulators (such as polyethylenimine (PEI),[130,168–171] polyethylenimine ethoxylated (PEIE),[51,172–175] PMMA,[124,154,176], and Al_2O_3[128,152,177]) or through alloying the ZnO with other metals (such as Al, Li, and Mg, among others).[55,126,135,137,138,147,178–181] Further improvements to red, green, and blue QDLED efficiency (such as the record efficiency devices) have generally arisen from enhancements in the QD PLQY (film PLQY in particular, which is generally lower than solution PLQY) via interface engineering of the gradient composition QD structure as seen in the trend of **Figure 2.1**.[22,50,52,78,122,125,131,146,153,154]

With all of the adjustments available to modify the ZnO / QD interface in order to tailor the electron injection, transport and exciton interactions, at this point the main limiting factor in QDLED performance lies in finding the optimal HTL and improving those properties for hole transport. While CdSe-based QDs possess a valence band energy level far deeper than commercially available organic HTLs, QDLEDs with the hybrid architecture incorporating an organic HTL still outperform all-inorganic QDLEDs. One such way to improve hole transport has been through the use of bilayer stepwise HTLs that combine a layer with good hole transport and another with good HOMO energy level matching with the QD valence band for better hole injection.[107,124,186,130,133,134,150,182–185] With this in mind, it seems odd that poly(9,9-dioctylfluorene-

co-N-(4-(3-methylpropyl))diphenylamine (TFB) is frequently utilized as a HTL in high efficiency QDLEDs, particularly in red and green devices. The root causes of their improved performance remain unclear given TFB's very shallow highest occupied molecular orbital (HOMO) energy level (-5.3 eV) compared to alternatives such as PVK (-5.8 eV), which has been reported to produce superior EQE when used in blue QDLEDs.[22,27,140–142,154,186,28,50,54,115,122,131,132,139] CBP (-6.0 eV) and 4,4′,4″-tris- (carbazol-9-yl)triphenylamine (TCTA) (-5.7 eV) are also commonly used thermally evaporated HTLs due to their reasonably deep HOMO energy levels but necessitate an upright device structure so that they are not damaged by subsequent solution processes.[23,78,123,127,129,171,182,187]

2.4 QDLED Stability and Electroluminescence Lifetime

As can be seen from **Figure 2.1**, there are far fewer reports on the lifetime of QDLEDs in comparison to the reports on EQE. The first major milestone in QDLED stability was achieved by Dai *et al*. in 2014 with their LT50 of 100,000 hours and EQE of 20.5%.[124] Now that high efficiency devices had been demonstrated, the next frontier would be achieving long EL lifetimes. While reports on the lifetime of various QDLEDs are not uncommon, very few studies have aimed at elucidating the root causes of their limited stability. As was noted previously, initial investigations have focused on the role of charge imbalance and subsequent Auger recombination that are caused in part by the large energy level mismatch between the valence band of the QD and the HOMO energy level of the HTL in device degradation. In general, the stability of QDLEDs has improved along with their EQE proving the importance of suppressing Auger recombination via meticulous design of gradient shell QDs and improving charge balance for both efficiency and stability.[26–28] In this case, the thermal energy resulting from the non-radiative Auger recombination is generally accepted to be the main material degradation route.[25] For devices with an upright architecture, environmental protection provided by the top ZnO layer is another common explanation for improved stability despite the fact that most lifetime tests are carried out in inert environments.[22,81] In this work, the term stability refers to the general degradation of QDLEDs which can occur through a variety of mechanisms and (EL) lifetime specifically refers to the LT50 characteristic and degradation of devices during electrical operation.

In 2015, Yang *et al*. extended the LT50 of red, green, and blue QDLEDs to 300,000 hours, 90,000 hours, and 1,000 hours, respectively.[22] This was done in an upright architecture utilizing $Cd_{1-x}Zn_xSe_{1-y}S_y$ compositional gradient QDs with ZnO and TFB. The authors investigated two different formulations, CdS-rich and ZnSe-rich intermediate compositions between the CdSe core and ZnS shell, finding that the ZnSe-rich QDs had more regular shapes, better size distribution, and self-assembly characteristics. The hole injection barrier is lower in the ZnSe-rich QDs due to the 0.2 eV shallower valence band of ZnSe *vs.* CdS,

improving charge balance and, therefore, QDLED efficiency and stability. The authors also noted that the large size of the QDs (~10 nm) as well as their gradient composition should suppress Auger recombination. Acharya *et al*. improved upon the red QDs in the previous work using the same structure and QDLED architecture, reporting a LT90 of 490 hours with an initial luminance of 2,550 cd m^{-2}.[132] This lifetime was remarkable for only a 10% drop in luminance, but after 430 hours there was a precipitous drop in luminance and the reason for this sudden degradation was unknown. After reporting a phenomenal LT50 of 2,260,000 hours for an initial luminance of 100 cd m^{-2} and LT95 of 2,300 hours for an initial luminance of 1,000 cd m^{-2} from red QDLEDs with a compositional gradient terminating with a ZnSe shell instead of ZnS, Cao *et al*. carried out a systematic investigation into the degradation of their devices.[115] The driving voltage of hole and electron single carrier devices over time was measured for the ZnSe shell that had good charge balance due to the reduced hole injection barrier and one with worse charge balance due to its ZnS shell. There was little difference between the electron-only devices over time but the hole-only device for the QDLED with worse charge balance experienced a much greater increase in driving voltage, pointing to hole current as a major factor affecting QDLED lifetime. With precise engineering of the very large size (~20 nm) QD through a CdSe / Cd$_x$Zn$_{1-x}$Se / ZnSe$_y$S$_{1-y}$ compositional gradient, Lim *et al*. effectively eliminated Auger recombination in their QDs.[78] This manifested in EQE that is relatively independent of driving current density meaning that there is negligible efficiency roll-off which is generally observed in many devices due to exciton-exciton (or exciton-polaron) interactions at high exciton density. As a result, their red QDLEDs utilizing ZnO and TCTA transport layers demonstrated a LT50 of 1,330,000 hours. Shen *et al*. also used compositionally graded QDs in their QDLEDs with TFB and ZnO transport layers, demonstrating LT50s of 1,600,000 hours for red and 1,760,000 hours for green with similar reasoning for their good stability.[28] While very good lifetimes have been demonstrated for red and green QDLEDs, the best LT50 for blue is several orders of magnitude less at 32,000 hours while many other reports are usually < 10,000 hours.[26] However, the device structure used to achieve this lifetime is quite interesting, especially since the performance red and green QDLEDs utilizing this structure were underwhelming. Instead of a traditional HTL, Khan *et al*. used a gradient hole injection layer consisting of the conductive polymer

poly(ethylenedioxythiophene):polystyrene sulfonate (PEDOT:PSS) and tetrafluoroethylene-perfluoro-3,6-dioxa-4-methyl-7-octene-sulfonic acid (PFI), which has been used as a work function modification layer in other works. This polymer mixture naturally segregates during the spincoating process to produce a gradient in the work function of the HIL from -5.2 eV at the cathode to -5.94 eV at the QD EML. The superior performance of the HIL mixture is attributed to the improvement in charge balance due to the HIL mixture's deeper work function in comparison to even PVK (-5.8 eV).

Recently, long-lifetime QDLEDs have been demonstrated with EQEs as low as 13.5%,[78] indicating that other factors aside from increasing charge balance and reducing Auger recombination must be involved. It is well-known that excitons are present in the organic HTL of hybrid QDLEDs and a significant body of work has focused on attempts to improve efficiency by recycling those excitons via energy transfer from emissive sensitizers near the QD / HTL interface.[111,188–191] This suggests that a significant number of electrons leaks from the QD emission layer into the HTL where they recombine with holes to form excitons. In the absence of some method of recycling, these excitons will relax non-radiatively. As organic layers are susceptible to damage by various exciton-mediated processes,[16,17,19,192–196] the non-radiative relaxation of excitons on the HTL will be ultimately detrimental to QDLED stability. In light of this, recent work has investigated the role of the HTL in QDLED degradation. Chang *et al*. found that the fast EL degradation that is often observed in QDLEDs during the early stages of electrical driving was correlated with a decrease in the PLQY of the QD emissive layer but that this correlation is not maintained in the longer term, in **Figure 2.2**(a).[197] The fast initial degradation mechanism is attributed to charging of the QDs as excess electrons occupy the conduction band which enhances the rate of Auger recombination in the emissive layer. The excess electron concentration in the QDs quickly saturates leading to a plateau in their PLQY, yet the IQE continues to degrade; an effect that is attributed to the formation of non-radiative recombination sites as a result of degradation in the HTL. In an investigation into the differences in stability between red (LT50 > 800 hours) and blue (LT50 ~4.5 hours) QDLEDs, Chen *et al*. observed the formation of cationic HTL degradation products in both QDLEDs but found that the HTL degradation could not explain the much

shorter blue device lifetime.[156] Instead, the faster degradation in blue QDLEDs was found to be associated with a faster increase in the capacitance transition voltage, as seen in **Figure 2.2**(b) and (c). The slight increase of the downward capacitance transition voltage after LT90 for the red QDLED is attributed to minor voltage increases that arise due to degradation of the HTL. However, the onset of increasing capacitance in the blue QDLED shifts toward a higher voltage and the maximum capacitance value increases after LT90 which indicates that significant charge accumulation at the ZnO / QD interface impedes electron injection into the QDs which escalates over time as seen in the further capacitance increases after LT50. This suggests that Auger recombination due to electron back transfer from the QD layer to ZnO and increasing charge accumulation when the conduction band energy of the QDs is shallower than that of ZnO was the main degradation process. More recently, the influence of the HTL on the QD emissive layer PLQY over time was investigated via exciton-induced degradation studies of QDLEDs under UV excitation rather than electrical driving in **Figure 2.2**(d).[198] By relying on photo-induced excitons, the effects of charge carriers (such as excessive charging of the QDs) become negligible and the exciton-induced degradation effects dominate. Results showed that the HTL material has a significant effect on the normalized QD PL intensity (analogous to PLQY) over time under continuous UV irradiation. Notably, the change in QD PL was found to generally follow the trend of the HTL susceptibility to exciton-induced degradation, indicating that degradation of the HTL can lead to a decrease in the QD PLQY and that degradation occurring close to the interface between QDs and the HTL is especially detrimental.
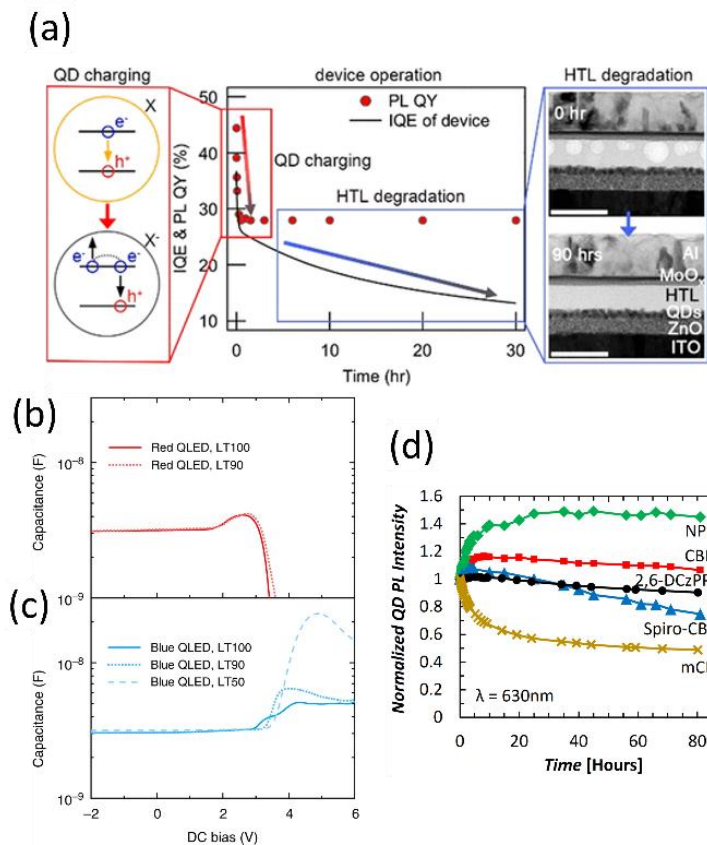
Figure 2.2 (a) Operation time-dependent traces of the internal quantum efficiency (IQE) of QDLEDs under a current density of 30 mA cm^{-2} (solid line), and the QD emissive layer PLQY in the same device (circle). Reproduced with permission.[197] Copyright 2018, American Chemical Society. Capacitance-voltage characteristics of (b) Red and (c) Blue QDLEDs in their initial state (LT100, solid line), after 10% degradation of their initial luminance (LT90, dotted line), and after 50% degradation of their initial luminance (LT50, dashed line). Reproduced with permission.[156] Copyright 2019, Nature Publishing Group. (d) Normalized QD PL intensity *vs.* time for QDLEDs with HTLs of N,N′-bis(naphthalen-1-yl)-N,N′-bis(phenyl)benzidine (NPB, diamond), CBP (square), 2,6-bis[3-(9H-carbazol-9-yl)phenyl]pyridine (2,6-DCzPPy, circle), 2,2',7,7'-tetrakis(carbazol-9-yl)-9,9-spirobifluorene (Spiro-CBP, triangle), or 1,3-bis(carbazol-9-yl)benzene (mCP, cross) under continuous UV irradiation. Reproduced with permission.[198] Copyright 2019, The Royal Society of Chemistry.

2.5   Motivation & Objectives

A great deal of work has been done on improving the synthesis of QDs to optimize their PLQY and emission characteristics, as discussed in the previous sections. By extending the stability of QDs themselves and reducing the degree to which Auger recombination occurs on QDs, recent QDLEDs have exhibited excellent efficiencies and long EL lifetimes. Although red QDLEDs have been demonstrated with LT50s of >1,000,000 hours for an initial luminance of 100 cd m^{-2}, many applications of these devices necessitate driving at higher luminance values. The aim of this work is to look beyond the QD synthesis enhancements and toward the other components of the device to identify and understand additional degradation mechanisms that may influence QDLED EL stability. In particular, since the materials used in this work are not novel and have been explored in many other works and since light emission occurs from the QDs, the interfaces between the transport layers and the QD EML have been identified as critical influences over QDLED performance, both in terms of efficiency and stability.

To this end, the following research objectives will be addressed:

1) Investigate the influence of the interface between the ETL and EML on QDLED performance by:

   a. Examining the effect of introducing a wide band gap polymer layer at this interface:

      i.   With respect to charge balance in the QDLED.

      ii. With respect to exciton quenching at this interface.

   b. Examining the role of this interface in long-term morphological stability:

      i.   With respect to the ETL processing parameters and characteristics.

      ii. With respect to the QD processing parameters and characteristics.

2) Investigate the influence of the interface between the EML and HTL on QDLED performance by:

   a. Examining the extent to which degradation of the HTL may affect QD PLQY:

      i.   With respect to exciton formation on the HTL during EL driving of devices.

      ii. With respect to photostability studies of fully- and partially-fabricated devices.

b. Examining the role of hole accumulation at the EML / HTL interface:

   i. With respect to the exciton formation and recombination zone within the HTL.

   ii. And identifying methods by which the accumulation at this interface may be reduced.

3) Investigate the influence of the interface between the HTL and HIL on QDLED performance by:

   a. Examining the extent to which degradation of the HTL may occur with respect to deposition of the HIL.

   b. Examining the barrier to hole injection into the HTL with respect to energy level matching between the HTL and HIL.

Chapter 3: Experimental Procedures

3.1   QDLED Fabrication

Unlike OLEDs, which have the benefit of complete deposition through thermal evaporation if desired, the QD layer in QDLEDs must be at least somewhat processed with solution-based techniques such as through spincoating, inkjet printing or transfer printing.[2] While beneficial for low-cost products, this can be detrimental to QDLED efficiency and stability.[2,80] The solution processing requirement adds another degree of inconsistency and complexity, imposing limits on the materials that can be used in certain devices as solvent orthogonality must be considered such that underlying layers are not destroyed.[22,80–82] Ultimately, this is a hurdle that must be overcome for both OLED and QDLED commercial relevance but should be kept in mind when analyzing performance, especially when comparing devices fabricated under different conditions.

The following chapter will outline the standard processing parameters and characterization techniques used in this work. However, due to optimization in the fabrication process and measurement setups over time, chapters 4-7 will specifically outline relevant differences in these parameters where applicable.

3.1.1   Material Selection

The first step in designing the QDLED fabrication process lies in material selection, as this will dictate the deposition order of each layer. As established in chapter 2, ZnO is the de facto ETL for QDLEDs and will be used in the devices studied in this work. The ZnO film is sol-gel synthesized with the following 3 components: a zinc precursor, a solvent, and a stabilizing agent. The zinc precursor can be an organic (acetate, acetylacetonate) or inorganic (nitrate, chloride, perchlorate) salt which dictates whether the solvent
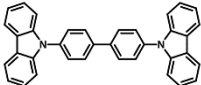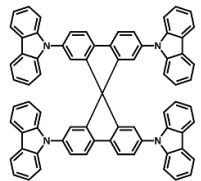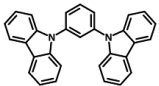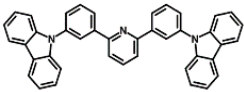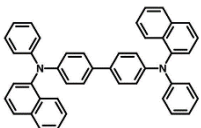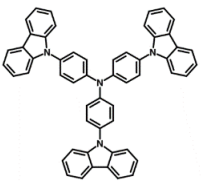
used is an alcohol (ethanol, methanol) or water, respectively.[199] Inorganic salts produce difficult-to-remove anionic species whereas organic salt contaminants easily decompose at low temperatures.[199] The salt also has an influence on the reaction with respect to how well it can stabilize the nanoparticles in solution to reduce coagulation and acetate has been shown to do this well.[199] It is for this reason that zinc acetate (ZnAc) is used as the precursor. The stabilizing agent monoethanolamine (MEA) improves solubility of the zinc complexes in alcohols to facilitate complete dissolution and the formation of a stable sol by hindering zinc hydroxide precipitation.[199] Intermediate species, such as zinc oxyacetate ($Zn_4O(Ac)_6$), zinc oxoacetate ($ZnO_{1-x}(AcO)_{2x}$) and hydroxide zinc acetate ($Zn_5(OH)_8(Ac)_2$), have been identified in literature to form through hydrolysis and inorganic polymerization of the precursors and are seemingly related to the carbon length-dependent solubility of ZnAc in a particular solvent.[199] Regardless, the intermediate products condense into colloidal wurtzite particles that grow via slow, controlled aggregation.[199] Not only do the choice of reagents factor into the final particle properties, but so too do reaction temperature, time, humidity, and concentration ratios.[199] In fact, the sol-gel synthesis process can be quite sensitive to changes in the reaction and deposition parameters. However, the optimal synthesis conditions for this work was found to be the addition of 197 mg ZnAc to 6 mL ethanol to which 54 mL of MEA is added and mixed at 800 RPM with a magnetic stirbar on a hotplate set to 45 °C for 40 min in a glovebox with a N_2 atmosphere. After passing though a 0.22 µm polypropylene filter, the resultant ZnO sol-gel should have a concentration of approximately 30 mg mL^{-1}. The annealing of the ZnO sol-gel film was initially carried out at 180 °C, higher than some QDs can withstand without degrading their PLQY, which necessitated an inverted structure so that ZnO could be deposited first.
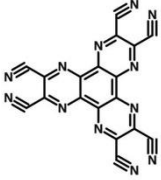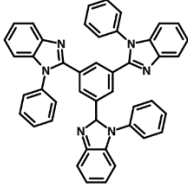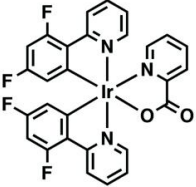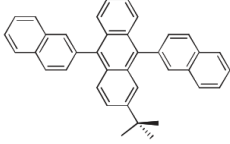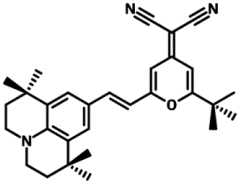
The inverted architecture allowed for the selection of a more diverse set of HTLs available from either solution deposition or thermal evaporation. Thermal evaporated HTLs were used in this work due in part to the ease of high-quality film depositions, but also for the ability to deposit multi-component films with precise compositions and the ability to use small molecule HTLs with deep HOMO levels such as CBP (-6.0 eV) whereas the deepest HOMO energy level of the polymer HTLs is PVK (-5.8 eV). In order to

investigate the effect of hole transport characteristics and interfaces on QDLED performance, several different HTLs are studied in this work which are detailed in **Table 3.1** below. To probe the extent to which excitons are formed in the HTL, the blue phosphorescent emitter FIrpic was often co-evaporated with CBP due to their similar HOMO and LUMO energy levels which should only have minor effects on charge transport through the QDLEDs. The blue fluorescent emitter 3-tert-butyl-9,10-di(naphth-2-yl)anthracene (TBADN) and the red fluorescent emitter 4-(dicyanomethylene)-2-t-butyl-6-(1,1,7,7-tetramethyljulolidyl-9-enyl)-4H-pyran (DCJTB) were also used as marking layers for similar intentions. Finally, in order to improve hole transport from the Al anode to the organic HTL, molybdenum trioxide (MoO_3) is typically used as a hole injection layer. However, an organic HIL alternative, 1,4,5,8,9,11-hexaazatriphenylene-hexanitrile (HATCN), has also been studied in this work. For the purpose of ZnO work function and interface modification, the wide band gap polymer polyethylenimine (PEI) was used.

Several different QDs were utilized in this work, all of which were purchased from commercial suppliers. Initially, green CdSe / CdS QD rods with an emission peak at 550 nm and 40 nm FWHM were purchased from Strem Chemicals (#48-1053, with > 80% PLQY and size of approximately 5 nm diameter × 20 nm width, passivated with hexadecylphosphonic acid ligands). Red CdSe / CdS QD rods with an emission peak at 626 nm and 40 nm FWHM were also purchased from Strem Chemicals (#48-1059, with > 80% PLQY and size of approximately 5 nm diameter × 20 nm width, passivated with hexadecylphosphonic acid ligands). The QD rod structure was initially chosen because they had the best PLQY of all commercially available QDs at the time but also provided potential benefits in self-alignment of the rods for a greater degree of horizontal optical dipole orientation. However, we found that the performance of our devices could be significantly improved by switching to red CdSe / ZnS QDs with an emission peak at 626 nm and 18 nm FWHM from Mesolight Inc. (Cd-QLED-630, with 74% PLQY and size of approximately 10-12 nm diameter, passivated with a mixture of oleic acid and octanethiol ligands). Illustrations of the spherical and rod-shape QD core/shell structures used in this work are depicted in **Figure 3.1**.

Table 3.1 Chemical name, molecular structure, HOMO and LUMO energy levels, band gap energy, and carrier mobility of the organic semiconductors studied in this work.

Chemical Name	Molecular Structure	HOMO Energy Level [eV]	LUMO Energy Level [eV]	Band Gap Energy [eV]	Carrier Mobility [cm^2 V^{-1} s^{-1}]
Hole Transport Layer					
4,4'-N,N'-dicarbazole-biphenyl **(CBP)**		-6.0 [200]	-2.9 [200]	3.1 [200]	1×10^{-3} [23]
2,2',7,7'-Tetrakis(carbazol-9-yl)-9,9-spirobifluorene **(Spiro-CBP)**		-5.8 [201]	-2.4 [201]	3.4 [201]	1×10^{-3} [200]
1,3-Bis(carbazol-9-yl)benzene **(mCP)**		-6.0 [202]	-2.5 [202]	3.5 [202]	5×10^{-4} [202]
2,6-bis[3-(9H-Carbazol-9-yl)phenyl]pyridine **(2,6-DCzPPy)**		-6.1 [203]	-2.6 [203]	3.5 [203]	2.2×10^{-6} [204]
N,N′-Bis(naphthalen-1-yl)-N,N′-bis(phenyl)benzidine **(NPB)**		-5.4 [107]	-2.4 [107]	3.0 [107]	1.6×10^{-3} [205]
4,4′,4″-tris-(carbazol-9-yl)triphenylamine **(TCTA)**		-5.7 [200]	-2.3 [200]	3.4 [200]	1.0×10^{-2} [206]

Hole Injection Layer					
1,4,5,8,9,11-hexaazatriphenylene-hexanitrile **(HATCN)**		-9.5 [207]	-5.5 [207]	4.0 [207]	N/A
Electron Transport Layer					
1,3,5-tris(2-N-phenylbenzimidazolyl)-benzene **(TPBi)**		-6.2 [200]	-2.7 [200]	3.5 [200]	3.0×10⁻⁵ [200]
Emissive Marking Layer					
bis(4,6-difluorophenylpyridinato-N,C2)picolinatoiridium **(FIrpic)**		-5.9 [165]	-3.0 [165]	2.9 [165]	N/A
3-tert-butyl-9,10-di(naphth-2-yl)anthracene **(TBADN)**		-5.8 [208]	-2.9 [208]	2.9 [208]	N/A
4-(dicyanomethylene)-2-t-butyl-6-(1,1,7,7-tetramethyljulolidyl-9-enyl)-4H-pyran **(DCJTB)**		-5.4 [209]	-3.2 [209]	2.2 [209]	N/A
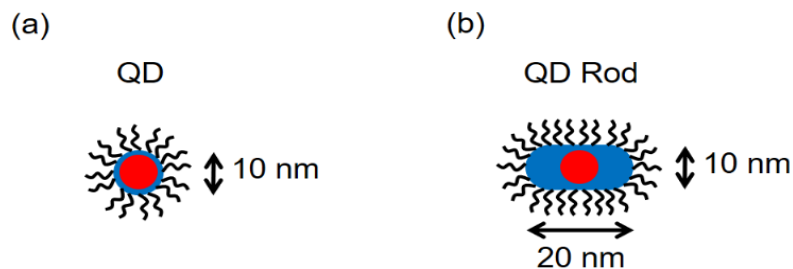
Figure 3.1 Illustrations of the core/shell structure of the (a) spherical and (b) rod-shape QDs used in this work.

3.1.2 Device Layout

A top-down perspective schematic of a completed device is depicted in **Figure 3.2**, illustrating the area covered by the emissive and transport layers as well as the intersection of top and bottom electrodes which defines the QDLED dimensions. Each QDLED studied in this work has been fabricated on a 50.8 mm × 50.8 mm glass substrate with pre-patterned ITO electrodes with approximately 100 nm thickness and 20 Ω $\square^{-1}$ resistivity. There are 7 ITO electrodes on two opposite sides of the substrate (14 in total) with a width of 2 mm used to define one dimension of the QDLED area. Toward the edge of the substrate, the width of each of those 14 ITO pads increases to 4 mm to improve the contact area with the test fixtures in the measurement systems. On either side of the sets of ITO electrodes are 7.4 mm thick ITO pads used as the counter electrode, bridged by a 100 nm thick layer of Al which defines the second dimension of the QDLED. The overlap of the bottom ITO electrode and the Al top electrode results in QDLEDs that are 2 mm × 2 mm. The emissive and transport layers are sandwiched between the two electrodes, with a thickness of approximately 100 nm. The rectangular feature in the ITO pad on the bottom left of the schematic is used to determine the orientation of the substrate.
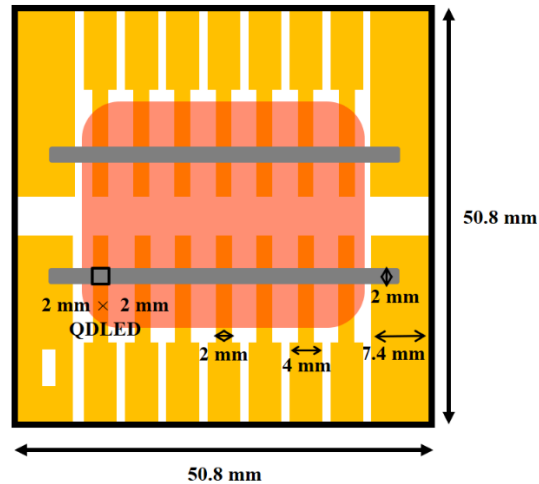
Figure 3.2 Schematic of the QDLED substrate layout used in this work.

3.1.3 Fabrication Process

The first step of QDLED fabrication is to clean the glass / ITO substrate (the convention used in this work will be to refer to consecutive layers in the order of their deposition) by vigorously rubbing the ITO pads with a cotton swab in a Micro-90 surfactant solution (1 wt% in DI water) to remove any residue from the ITO photolithography patterning process. The substrate is then sonicated in DI water for 10 min before rinsing in DI water, then isopropyl alcohol (IPA), and blow-dried with N_2 gas. The substrate is then baked at 80 °C for 10 min to remove any residual solvents. The substrate is then placed in the Trion Phantom II reactive-ion etching system for a 5 min inductively coupled plasma treatment with an O_2 gas flow of 20 sccm, a pressure of 20 Pa, and power of 100 W.

The ZnO solution is filtered through a 0.22 µm polypropylene filter again during the deposition on the substrate in a Laurell WS-400-6NPP-Lite spincoater. Our optimized QDLED fabrication process involves spincoating in ambient conditions at 1000 RPM for 60 s, then annealing at 150 °C for 30 min in air. The resulting film is 35 nm thick as measured by surface profilometer, and other thicknesses can be obtained by varying the mass of ZnAc and volume of MEA while keeping the ethanol volume constant during ZnO synthesis.

Several different QD film thicknesses are prepared in this work, depending on type of QD used, manufacturer of the QDs, and concentration of the QD solution. In general, the film is deposited via spincoating in a Vigor SciLab Single Station glovebox in a N_2 atmosphere at 2000 RPM for 60 s, then annealed at 50 °C for 30 min. Exposure of the QD film to air is minimized during the transfer of the substrate from the QD deposition glovebox to the thermal evaporation chamber for the remaining QDLED deposition steps by keeping the substrate in a vacuum-sealable aluminum container.

The organic semiconductors, MoO_3, and Al anode are all deposited by thermal evaporation in an Angstrom Engineering EvoVac evaporation chamber. The materials are evaporated at a rate of 1 Å s^{-1} as measured by a quartz crystal microbalance sensor at a pressure of at most 5×10^{-6} Torr.

3.2   QDLED Characterization

Once the QDLED fabrication process is completed, the devices are kept in a nitrogen atmosphere during the electrical and optical measurements as well as storage to reduce the effects of extrinsic degradation. Characterization of each set of devices generally encompasses current density-voltage-luminance (JVL) measurements, EL and PL spectral measurements, and EL stability measurements. Other characterization techniques such as delayed EL spectroscopy, transient photoluminescence (TrPL) spectroscopy, and UV photostability measurements are utilized to probe specific characteristics of the devices following the initial characterization measurements. Unless otherwise specified, all device tests are carried out in a test box under a N_2 gas atmosphere.

3.2.1   Current Density-Voltage-Luminance Characteristics

JVL measurements are performed by sweeping the driving voltage of the QDLED from 0 V to 8 V by an Agilent 4155C semiconductor parameter analyzer to record the current at each step. The current density is calculated by dividing the measured current by QDLED area (4 mm^2). The final voltage step approximately corresponds to 4 V above the driving voltage required to maintain a current density of 20 mA cm^{-2}. In cases where this driving voltage is greater than 4 V, the final sweep voltage is increased in correspondence to this value (i.e. for a QDLED with a driving voltage of 8 V, the voltage sweep extends to 12 V). The luminance is recorded by silicon photodiode connected to the semiconductor parameter analyzer to correlate each photocurrent value to the voltage step. Finally, the photocurrent is calibrated to a luminance value recorded at a driving current of 20 mA cm^{-2} by a Minolta Chroma Meter CS-100. The EQE of the QDLEDs were calculated as outlined by Okamoto *et al*. assuming a Lambertian emission distribution.[210]

3.2.2 Electroluminescence Stability

EL lifetime measurements are conducted via a Botest Systems GmbH OLT Lifetime Test System applying a constant current density of 20 mA cm^{-2} to the QDLEDs while a silicon photodiode records the luminance of the devices as a function of testing time. The real luminance of the QDLED over time is calibrated to the initial luminance as measured by a Minolta Chroma Meter CS-100. The driving voltage of the QDLED is also recorded as a function of testing time. In order to measure the LT50 of a device, the test is terminated when the luminance of the QDLED has reached 50% of its initial luminance value. In these measurements, there may be a "burn-in" period of up to several hours where the luminance increases over time as a result of initial changes in charge transport, charge balance, or interface quality under a constant current until the device reaches equilibrium which has been attributed to joule heating.[211] This time is not taken into account in the stability figures or metrics, and the lifetime is considered to begin from the peak luminance value.

3.2.3 Electroluminescence Spectroscopy

The EL emission spectra of the QDLEDs are measured by an Ocean Optics QE65000 spectrometer with a range of 350-750 nm, collected via an optical fiber. The QDLEDs are typically driven with a constant current density of 20 mA cm^{-2} unless otherwise specified. The light intensity measured by the spectrometer is normalized to the peak of interest which generally corresponds to the highest intensity peak (i.e. emission from the QD EML) to facilitate comparison between the different contributors to the EL spectrum.

3.2.4 Time-Resolved Delayed Electroluminescence Spectroscopy

The time-resolved delayed EL spectroscopy technique measures persistent luminescence from a device after the end of the electrical bias and thus gives information about residual charges and / or long-lived excited states. The delayed electroluminescence signal was measured with a R928 photomultiplier tube, amplified by a Keithley 428 Current Amplifier and recorded by a Tektronix TDS5054 Digital Phosphor Oscilloscope. In this technique, QDLEDs are driven with a forward bias square pulse supplied by a custom-built operational amplifier driven by a Stanford Research Systems DG535 Digital Delay / Pulse Generator to achieve a driving current of 20 mA cm^{-2} and allow prompt electroluminescence to reach steady state. A ThorLabs MC1000A optical chopper system is positioned between the QDLED and an optical fiber to block the detection of the prompt EL signal. The chopper is opened after the forward bias pulse terminates to begin recording the delayed EL signal. A schematic diagram of the delayed EL experimental setup and outline of time-resolved driving scheme, electroluminescence, and data acquisition are provided in **Figure 3.3**. This delay is sufficiently long for all allowable luminescent exciton relaxation processes to occur and is much larger than a typical QDLED electrical time constant,[120,212] rendering electrical transient effects negligible. Therefore, any measured EL signal will arise from radiative decay of excitons that are formed after the termination of the forward bias pulse. The prompt and delayed EL spectra are identical, as shown in **Figure 3.4** for a green QDLED, confirming that the QDs are the source of EL in both cases.

In general, the formation of excitons in the microsecond time scale in these QDLEDs can be attributed to two processes: (i) recombination of residual (trapped / accumulated) charges in the various device layers including the HTL that become mobile and capable of recombination, producing luminescence after the end of the forward bias pulse and / or (ii) triplet excitons created within the HTL that diffuse slowly and eventually reach the QDs, inducing their late excitation via energy transfer either directly from those triplet states (by a Dexter process) or by a Förster process from singlet intermediates produced by triplet-triplet annihilation (TTA).

In devices where process (i) is the dominant mechanism behind the delayed EL, the application of a reverse bias will lead to a permanent reduction in the delayed EL intensity and is sometimes accompanied by the appearance of a spike due to the redistribution of charges. Whereas, in devices where process (ii) is more dominant, the reverse bias will result in a temporary decrease in the delayed EL signal due to electric-field induced dissociation of excitons which recovers after the reverse bias has ended. To test for this effect, a 2.5 V reverse bias pulse is applied after the onset of the measurement, and its effect on the delayed EL intensity is monitored.
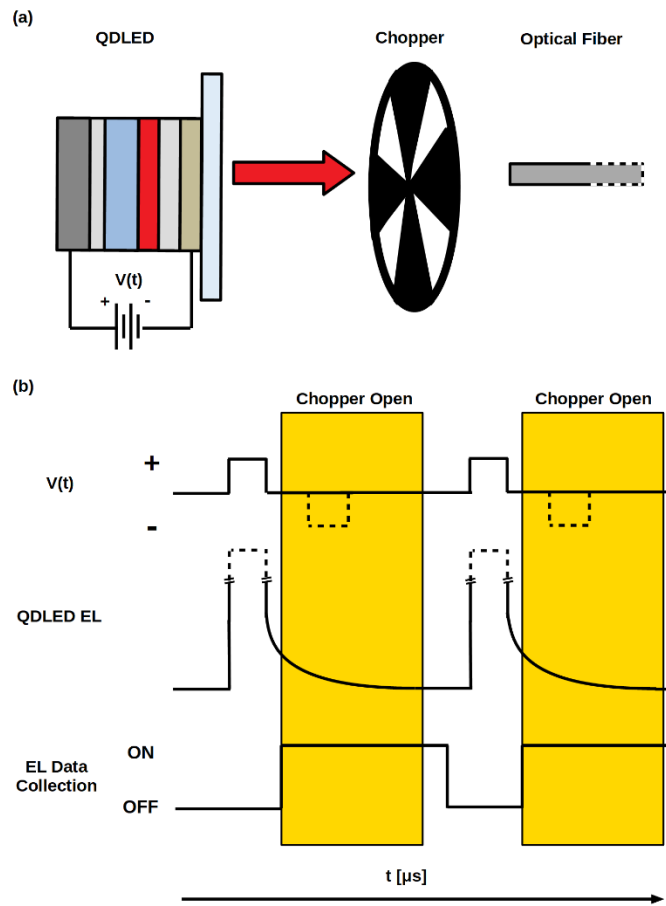
Figure 3.3 (a) Schematic representation of the delayed EL experimental setup. (b) An outline of time-resolved QDLED driving scheme, prompt and delayed EL, chopper position, and data acquisition throughout the delayed EL measurement.
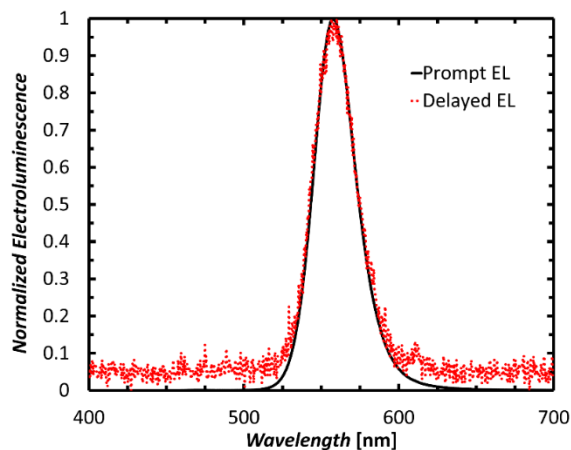
Figure 3.4 Normalized spectra for prompt (solid black) and delayed (dotted red) EL components.

3.2.5   Photoluminescence Spectroscopy

The PL emission spectra of the QDLEDs and other films are measured by an Ocean Optics QE65000 spectrometer with a range of 350-750 nm and collected via an optical fiber. PL is induced by illumination with a 200 W Hg-Xe lamp controlled with an Oriel 77200 monochromator to isolate certain peaks in the incident light emission spectrum. Generally, the Hg-Xe peaks near 330 nm, 365 nm, and 430 nm are used in this work for the different absorption spectra of the materials used herein. The intensity of light measured by the spectrometer is then normalized to the peak of interest which generally corresponds to the highest intensity peak (i.e. emission from the QD EML) to facilitate comparison between the different contributors to the PL spectrum of the specimen.

3.2.6   Time-Resolved Transient Photoluminescence Spectroscopy

TrPL decay was measured with an Edinburgh Instruments FL920 spectrometer equipped with a 375 nm peak emission EPL375 picosecond pulsed laser diode. The laser diode optically excites the sample, and the light emitted from the specimen at the target wavelength as a result of exciton recombination is

measured as a function of time elapsed from the initial excitation. A material's TrPL characteristic is correlated to the materials' exciton lifetime. Therefore, this technique can be utilized to elucidate the exciton quenching processes in devices, or energy transfer characteristics between two materials. This measurement technique is carried out under ambient conditions.

3.2.7 UV Photostability

Under electrical bias, charge carrier and exciton density and distribution all contribute to the degradation of QDLEDs. However, the UV photostability of QDLEDs has been measured in order to isolate the contribution of exciton-induced degradation to the devices from the contribution of charge carriers. Under UV irradiation, incident photons excite ground state electrons in the sample to form only singlet excitons. In these experiments, a 370 nm peak wavelength Analytik Jena UVL-18 handheld UV lamp with an irradiation power of 500 μW cm^{-2} is used as the excitation source. PL measurements of the specimen are measured by an Ocean Optics QE65000 spectrometer with a range of 350-750 nm and collected via an optical fiber over time. The peak emission of the specimen is normalized to the initial emission intensity to measure its change in intensity over time. Without the confounding factors of triplet excitons, charge carriers, and exciton-polaron interactions, the change in PL intensity over time can be attributed to the effects of singlet exciton formation and relaxation.

3.2.8 Surface Morphology & Roughness

A Veeco Nanoscope atomic force microscope (AFM) is used to characterize the surface morphology and roughness of deposited films. There are two characteristics of interest in the evaluation of roughness: peak-to-valley (R_{pv}) and root-mean-square (R_{rms}) roughness. R_{pv} represents the difference between the maximum and minimum heights in a given image whereas R_{rms} is the square root of the sum of squared film

heights over the entire measured area. Both roughness values are useful in characterization of a film surface as the R_{pv} may result in localized shorts through the following layer and R_{rms} can be taken to represent the global film roughness and is the roughness value generally reported on in literature. In this work, AFM images are taken from a 5 μm × 5 μm area and roughness values are taken from an average of at least 3 sample areas. This measurement technique is carried out under ambient conditions.

Chapter 4: The Role of the Interface Between the Electron Transport Layer and the Emissive Layer on QDLED Performance

This work has been published in Davidson-Hall, T. and Aziz, H., Nanoscale, vol. 10(5), pp. 2623-2631, 2018. It has been reproduced with permission from the publisher.

4.1 Introduction

Although the unique properties of colloidal QDs such as high PLQY, narrow EL spectra, and solution processability make them advantageous for use as the emissive material in light-emitting devices,[2,56,66,67,109,117,160] there are unique challenges to QDLEDs that arise from the structure of the QDs and their poor energy level alignment with the transport layers that lead to exciton quenching and inefficient devices; an issue that has been a focus of many recent works.[82,111,172,173,183,188,213–218,120,124,127,128,165,168–170] PEI and its modified derivative PEIE are two polymer interlayers that have been used in organic photovoltaics (OPVs),[219–222] OLEDs,[223–225] and more recently QDLEDs,[168–170,172,173,217,218] to improve overall device performance. Here, the enhancement has been largely attributed to a reduction in the work function of electrodes, leading to a significant improvement in electron collection or injection, respectively. The mechanism behind the reduction in work function energy level has been identified as a process in which the amines along the polymer backbone adsorbed onto the conductor surface undergo partial charge transfer, inducing an interfacial dipole that consequently leads to a shift in the vacuum level.[219–221,223,226] An approximate work function shift of 1 eV has been observed for PEIE regardless of the electrode or polymer layer thickness by Zhou *et al.*[219] On a sputtered ZnO film, Kim *et al.*[223] observed a significant thickness-dependence to the PEI with films thinner than 10 nm inducing a 2 eV depression of the work function. This shift in the work function is valuable for devices such as OLEDs and OPVs where the active layer typically has a LUMO energy level significantly shallower than the work function of the cathode.

Although the deep work function of ZnO (-4.4 eV)[223] is an issue for injection into the organic semiconductors, the deep conduction band energy level of CdSe-based quantum dots (-4.0 to -4.4 eV)[2,172,216,217] compares favorably for electron injection naturally. The energy level alignment between these layers is one of the reasons for the wide adoption of ZnO as the typical electron transporting layer in QDLEDs.[22] PEIE has been demonstrated to improve QDLED performance when used as an EIL between an ITO cathode and the QD EML in the inverted architecture,[217,218] and the incorporation of ZnO as an ETL led to further enhancements which were attributed to an improvement in electron injection into the QDs.[172] A recent study by Ding *et al.*[130] found that the PEI also improves the performance of the typical ZnO ETL in QDLEDs but identified that while the polymer can reduce the work function of ZnO, its insulating nature primarily inhibits electron injection into QDs leading to improved charge balance. As hole injection into the quantum dots is much more difficult comparably, inhibiting electron injection would improve charge balance within the device and can therefore lead to the improvement in efficiency.[124,128] Considering the conflicting explanations of the role of PEI and PEIE in enhancing the efficiency of QDLEDs, it therefore remains unclear what mechanism governs the efficiency enhancement of such devices. Furthermore, repercussions of PEI-based polymers on the EL lifetime of QDLEDs remain unknown.

In this work, we investigate and compare the effect of a PEI layer at the ZnO / QD interface to the typical device architecture as it pertains to electron transport and injection, EQE, exciton quenching, and EL lifetime. We find that the improvement in QDLED efficiency is accompanied by a corresponding increase in driving voltage. Although this has been attributed to a decrease in electron transport through the devices and a progression toward charge balance in literature,[130] through investigations making use of phosphorescent marking layers and delayed EL measurements we find that even thick PEI layers increase electron injection. Thus, the improvement in efficiency cannot be attributed to improved charge balance but rather to eliminating the non-radiative quenching of QD excitons by the ZnO layer. Furthermore, these enhancements come with negligible impact on the EL lifetime of the QDLEDs.

4.2   Experimental Details

4.2.1   Device Fabrication

The structure of QDLEDs studied here is depicted in **Figure 4.1** and fabricated on 80 nm thick ITO patterned glass substrates (Kintec) with 15 Ω $\square^{-1}$ sheet resistance cleaned and sonicated sequentially with Micro 90, DI water, and IPA solutions before treating with O_2 plasma for 5 min. ZnO sol-gel was prepared by adding 197 mg ZnAc (Sigma-Aldrich) to 54 µL MEA (Sigma-Aldrich) in 6 mL ethanol and mixing at 600 RPM for 40 min and a temperature of 45 ºC. The ZnO solutions were filtered through a 0.22 µm polypropylene filter, spincoated at a rotational speed of 1000RPM for 60 s, and annealed at 180 ºC for 30 min. PEI (Sigma-Aldrich) was diluted in 1-propanol and spincoated at a rotational speed of 5000 RPM for 60 s and annealed at 120 ºC for 10 min. Green CdSe / CdS quantum dot rods (Strem Chemicals #48-1053, with > 80% PLQY and size of approximately 5 nm diameter × 20 nm width, passivated with hexadecylphosphonic acid ligands) with a peak EL emission of 550 nm were diluted to 0.6 mg mL^{-1} in hexane and spincoated at a rotational speed of 2000 RPM for 30 s, then annealed at 50 ºC for 30 min. The absorption spectrum of the QD rods in solution, as well as photoluminescence spectra and transient photoluminescence lifetime of QDs in solution and film can be found in **Figure 4.2**. The remaining layers of CBP (Luminescence Technology), FIrpic (Luminescence Technology), MoO_3 (American Elements), and Al (Angstrom Engineering) were deposited at a rate of 0.1-2 Å s^{-1} in an Angstrom Engineering EvoVac thermal evaporation chamber at a base pressure of 5×10^{-6} Torr.
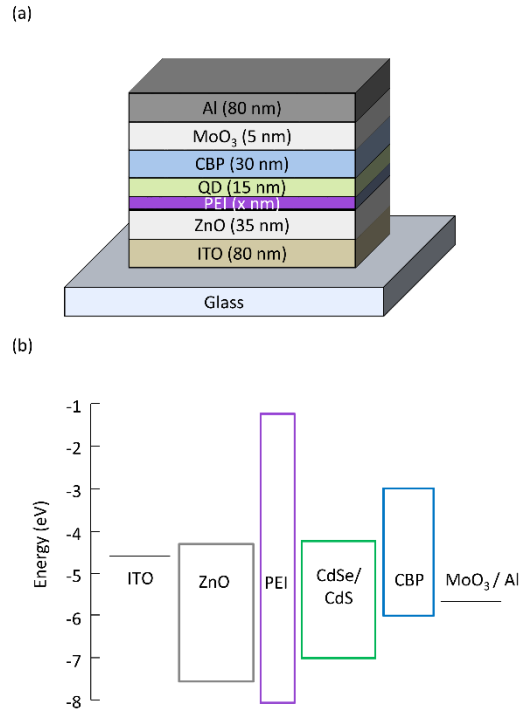
Figure 4.1 QDLED (a) structure and (b) energy level diagram where the values of each component layer have been derived from literature.[109,117,172,182,214–217,223,227]

4.2.2 Device Characterization

Luminance of the QDLEDs was measured with a Minolta Chroma Meter CS-100, and JVL measurements were carried out via an Agilent 4155C Semiconductor Parameter Analyzer connected to a silicon photodiode. EQEs were calculated as outlined by Okamoto *et al*. assuming a Lambertian emission distribution.[210] Spectral measurements of the QDLEDs were measured using an Ocean Optics QE65000 spectrometer. PL was induced by illumination with a 200 W Hg-Xe lamp controlled with an Oriel-77200 monochromator. Time-resolved delayed EL signal was measured with a R928 photomultiplier tube, amplified by a Keithley 428 Current Amplifier and recorded by a Tektronix TDS5054 Digital Phosphor Oscilloscope. Forward and reverse bias signals for delayed EL tests were supplied by a custom-built operational amplifier driven by a Stanford Research Systems DG535 Digital Delay / Pulse Generator

connected to a ThorLabs MC1000A Optical Chopper to eliminate the prompt EL signal. TrPL decay was measured with an Edinburgh Instruments FL920 spectrometer equipped with a 375 nm peak emission EPL375 picosecond pulsed laser diode. A Veeco Nanoscope AFM was used to characterize the morphology and surface roughness of deposited films. EL lifetime measurements were performed in a Botest Systems GmbH OLT Lifetime Test System with a constant driving current maintained at 20 mA cm^{-2}. During all device tests, aside from TrPL measurements, the QDLEDs were kept in a N$_2$ atmosphere.
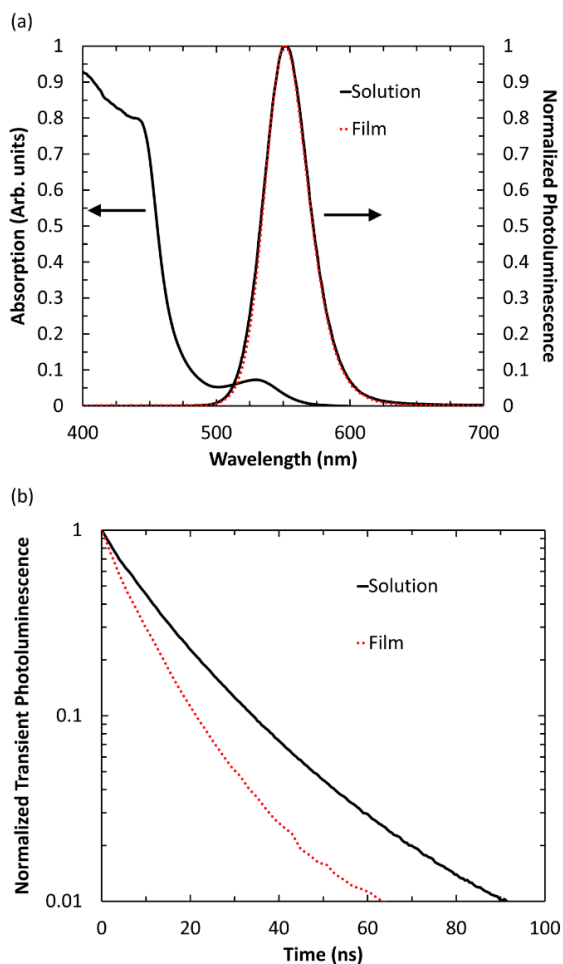
Figure 4.2 (a) Absorption spectrum of QD rods in solution and photoluminescence spectra of QD rods in solution (solid black) and film (dotted red). (b) Transient photoluminescence lifetime of QD rods in solution (solid black) and film (dotted red).

4.3   Results and Discussion

In the QDLEDs studied here, PEI was used as the polymer interlayer due to the greater modification in work function observed in literature compared to PEIE.[222,223] Four different device structures were fabricated with nominal PEI film thickness of 4 nm, 8 nm, 15 nm and 30 nm corresponding to solution concentrations of 0.25 mg mL^{-1}, 0.5 mg mL^{-1}, 1 mg mL^{-1}, and 2 mg mL^{-1}, and compared to a control device without the PEI interlayer (0 nm). The EQE versus current density characteristics of these devices are presented in **Figure 4.3**(a). The maximum EQE of the control structure was measured to be 4.5% and increased to 7.2% and 7% upon introduction of the 4 nm and 8 nm thick PEI layers, respectively, corresponding to enhancements by a factor of 1.6× and 1.5×. For the same devices, there is only a 10% increase in maximum luminance with the incorporation of PEI. The largest improvement in QDLED efficiency here occurs over the low current density regime where luminance levels typically desirable for use in display applications.[2] Increasing the PEI layer thickness to 15 nm and 30 nm leads to a decrease in the maximum EQE to 3.3% and 2.2%, respectively. **Figure 4.3**(b) shows the current density versus voltage (JV) and luminance versus voltage (LV) characteristics of these devices. As the PEI layer thickness increases, there is a shift in the JV characteristics toward higher driving voltages relative to the control structure, a conventional indication of a decline in carrier injection and / or transport through the devices. These results seem to oppose the common belief that the reduced ZnO work function via PEI will improve electron injection into CdSe-based quantum dots but are consistent with the recent findings that PEI improves charge balance by inhibiting electron injection.[130] However, an alternate argument exists whereby the increasing total thickness of QDLEDs with PEI effectively reduces the electric field intensity across the device during electrical driving with the same bias potential. Thus, the voltage required to reach the threshold electric field for carrier injection within the device increases with PEI thickness. Despite the increase in driving voltage that PEI layers introduce, devices with nominal PEI thickness up to 8 nm are more efficient than control devices which indicates that there is some benefit gained from the incorporation of a PEI layer. However, QDLEDs with PEI exhibit a decrease in the onset current of efficiency roll-off as

shown in **Figure 4.3**(a). The efficiency roll-off in QDLEDs can be attributed to TTA, exciton-polaron quenching, or Auger recombination which results in a loss of efficiency due to increased non-radiative recombination processes.[123,127] Auger recombination is a known issue within QDLEDs limiting the efficiency due to excess electron injection and charge imbalance.[2,24,70,112,123,166,227] Thus, as the PEI thickness increases and efficiency roll-off begins occurring at a reduced current density, there appears to be a charge imbalance within the device leading to enhanced non-radiative relaxation pathways for excitons. Moreover, the PEI layers significantly reduce the leakage current through devices, suggesting that the ZnO / QD interface is critical for optimizing device performance.
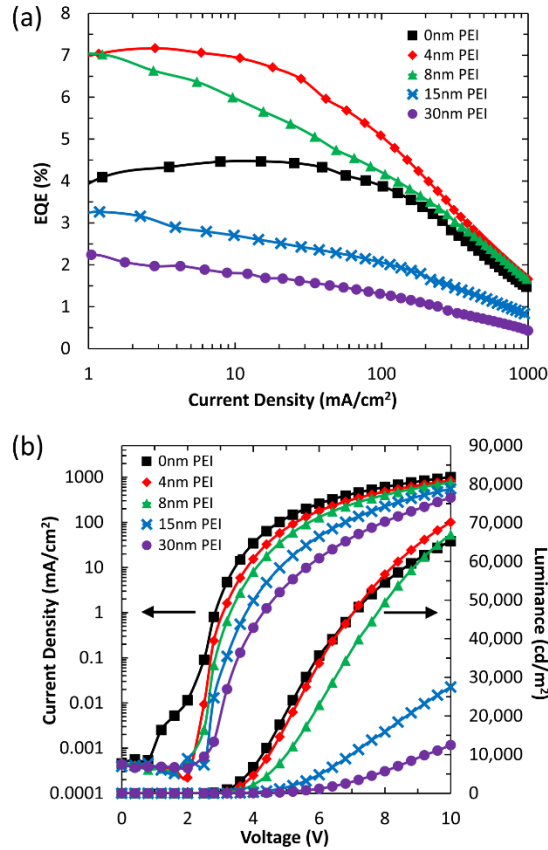
Figure 4.3 (a) EQE *vs.* current density and (b) Current density and luminance *vs.* voltage characteristics for devices with various PEI interlayer thicknesses.

To further investigate the effect of the PEI layer on charge distribution within the devices, a 5 nm luminescent marking layer consisting of the phosphorescent FIrpic emitter with a concentration of 20% in CBP was introduced in the device at the QD / HTL interface. The marking layer is used to probe shifts in the electron-hole recombination zone within the device structure due to the use of the PEI layers, and thereby uncover relative changes in the amount of electrons that have been injected past the QD EML into the HTL. Electrons in the HTL should easily recombine with accumulated holes at the QD / HTL interface given the large barrier to hole injection into the QDs, but any generated excitons would otherwise (i.e. without the marking layer) be difficult to resolve due to the low PLQY of the HTL material in comparison to the highly luminescent QDs. QDLEDs with PEI thickness ranging from 0 nm to 15 nm were fabricated with the FIrpic marking layer to understand the influence of PEI thickness on electron transport through the devices. Normalized EL spectra from devices containing the marking layer and 4, 8 and 15 nm thick PEI layers are presented in **Figure 4.4**. A spectrum from a device without a PEI layer is included as a reference (denoted by "0 nm PEI" in the figure). In addition, a spectrum from a device with neither the PEI layer nor the marking layer is also included (denoted by "0 nm, No Marking Layer" in the figure). A comparison of the last two spectra shows that the introduction of the marking layer leads to only a very small amount of FIrpic emission (Firpic emission intensity at 480 nm is only about 0.5% of the QD emission peak intensity) indicating that the marking layer does not significantly alter charge distribution or the location of the electron-hole recombination zone within the devices. Introducing PEI into the device structure increases the FIrpic contribution peak at 480 nm to the electroluminescence from 0.5% of the QD emission peak (0 nm PEI) to 2.2% (4 nm PEI), 2.5% (8 nm PEI), and 5.3% (15 nm PEI), which can be seen more clearly from the enlarged view in the figure inset. The increasing FIrpic:QD emission ratio indicates that PEI improves electron injection as more excitons are generated in the HTL beyond the EML even with the thicker PEI layers, leading to the decline in EQE observed in **Figure 4.3**(a) at the larger thicknesses. This contrasts with the notion that the increasing driving voltage discussed previously arises from a reduction in electron transport across the PEI layer. Rather, the driving voltage required to supply electric field across the device scales as a function of device thickness and occurs along with an increase in electron injection.

Therefore, although an increase in PEI thickness will lead to an increase in its resistance, the effect is offset by the increase in electric field at the contact. This may explain the shift in the recombination zone into the HTL.
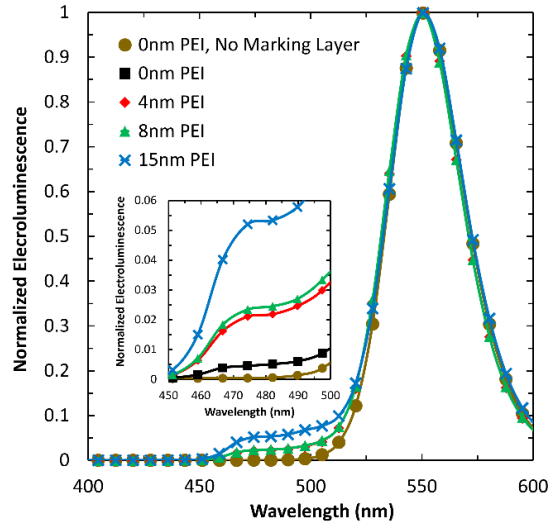
Figure 4.4 EL spectra of devices with a FIrpic marking layer and PEI thickness increasing from 0 nm to 15 nm, normalized to the QD emission peak at 550 nm. The inset figure is the same EL spectra zoomed in to accentuate the FIrpic contribution.

In order to confirm that the PEI layer does indeed increase electron injection within the QDLEDs, delayed EL measurements were performed using an experimental setup as described in section 3.2.4. **Figure 4.5**(a) shows the delayed EL intensity versus time characteristics collected from the QDLEDs with 0 nm, 4 nm, 8 nm, and 15 nm thick PEI layers. Clearly, the intensity of the delayed EL increases upon increasing the PEI layer thickness from 0 nm to 8 nm but plateaus from 8 nm to 15 nm. The normalized characteristics are provided in the inset and show that the delayed EL decay rates are essentially identical in all devices despite the different delayed EL intensities. The relative changes in delayed EL intensity with PEI thickness do not correlate with changes in prompt EL as seen from the different trends in **Figure 4.5**(b).
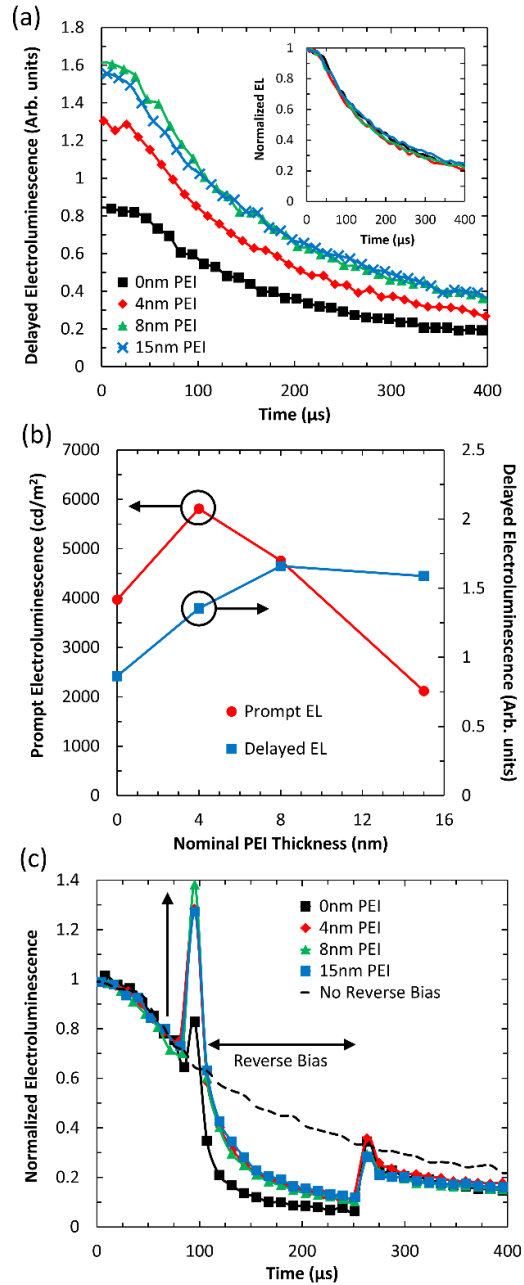
Figure 4.5 (a) Delayed electroluminescence of QDLEDs with PEI thickness from 0 nm to 15 nm. The inset figure is normalized to the maximum delayed electroluminescence signal. (b) Prompt and delayed electroluminescence as a function of PEI thickness. (c) Normalized delayed electroluminescence of QDLEDs with PEI thickness from 0 nm to 15 nm where a 2.5 V reverse bias is applied from 100 µs to 250 µs. The 0 nm PEI unbiased curve from (a) is included for reference.

This verifies that the observed delayed EL indeed has a different origin (i.e. it arises from the radiative decay of excitons that are formed after the termination of the forward bias pulse as noted earlier). In general, the formation of excitons in the µs time scale can be attributed to two factors: (i) recombination of residual

72

(trapped) charges in the device layers that become de-trapped, and hence become capable of recombination and producing luminescence after the end of the forward bias pulse and / or (ii) triplet excitons created within the CBP HTL during the forward bias pulse that diffuse slowly and eventually reach the QDs and induce their late excitation via energy transfer either directly from those triplet states (by a Dexter process) or by a Förster process from singlet intermediates produced by TTA. In previous work, it was shown that in devices where (i) is dominant, the application of a reverse bias leads to the appearance of a spike in delayed EL. This is because the reverse bias facilitates the detrapping of carriers and their drift back toward the QD layer. This significantly increases the rate at which these residual carriers recombine and materializes as a spike in the delayed EL curve at the onset of the reverse bias.

To test for this effect, a 2.5 V reverse bias pulse, 150 µs long, is applied 100 µs after the onset of the measurement, and the effect on the delayed EL intensity is monitored. **Figure 4.5**(c) shows the delayed EL characteristics from the same set of devices in this case. Delayed EL from a 0 nm PEI device without the application of the reverse bias is also included for reference. The traces were normalized to their initial value in order to facilitate comparisons between the relative spike intensity. Without PEI, there is only a small spike in delayed EL at the onset of the reverse bias. However, the spike increases significantly in devices with a PEI layer indicating that more residual charges exist in these devices. Notably, there is only a minor difference between the ratio of spike intensity to initial delayed EL signal in the three PEI-containing devices. Considering that the reverse bias is fixed at 2.5 V, the electric field across the devices decreases with increasing PEI thickness. The similar spike height in the PEI-containing devices therefore means that a similar residual charge recombination rate occurs at an increasingly lower field as the PEI layer thickness increases, suggesting that the number of residual charges must be increasing in the same direction. Considering that hole injection into the QD layer is generally inefficient due to the large energy hole injection barrier at the HTL / QD interface, it follows that those residual charges must be electrons in the QD layer or the HTL. It can be seen that a second smaller spike appears at the end of the reverse bias pulse, which once again can be attributed to the reorganization of residual charges upon removal of the bias

leading to another opportunity for increased electron-hole recombination. Following the second spike, there is a recovery of the delayed EL trace as the field-induced quenching of excitons that occurs during the reverse bias pulse is eliminated. However, the delayed EL recovers to a point below that of the trace without a reverse bias pulse. This suggests that the 2.5 V reverse bias field does not completely sweep out these residual charges. With the knowledge that the PEI layers induce a shift in the recombination zone into the HTL through the previous marking layer experiments and that hole injection from the HTL to QD layer is difficult, the increase in residual charges must therefore arise from PEI enhancing electron injection within QDLEDs.

Considering that PEI layers are found to improve rather than hinder electron injection, and result in excess residual electrons in the QD and hole transport layers as observed from the delayed EL measurements, the efficiency enhancement effect of PEI cannot be attributed to improved charge balance within the QDLEDs. Other factors must therefore be behind this effect. In regard to this, the quenching of excitons via charge transfer to trap states in ZnO or non-radiative Auger recombination has been established as a significant factor contributing to efficiency loss in QDLEDs.[2,82,120,123,128,214,216,227] Thus, incorporation of a wide band-gap polymer interlayer such as PEI is expected to reduce exciton quenching by the ZnO film and may therefore play a role in the enhancement of QDLED efficiency as Dai *et al*.[124] previously reported with a PMMA interlayer and Ding *et al*.[130] recently reported with PEI. To further probe the effects of PEI on the quenching of excitons by ZnO, 15 nm and 30 nm thick QD films were deposited onto both ZnO (A – 15 nm, B – 30 nm) and 8 nm PEI films coated on ZnO (C – 15 nm, D – 30 nm). **Figure 4.6**(a) depicts the PL spectra of the four multi-layer structures. As expected, the PL intensity is much greater for the 30 nm QD film compared to the 15 nm film. However, there is also a notable increase in PL intensity for both QD films when the PEI interlayer is introduced between the ZnO and QDs. An increase in QD PL intensity upon passivation of the ZnO film is indicative of a reduction in QD exciton quenching by ZnO. Further corroboration of this phenomenon is observed in **Figure 4.6**(b) which shows the TrPL behaviour of each film. **Table 4.1** collects the two stretched biexponential decay fitting parameters for the QD films'

TrPL for a quantitative measure of the improvements in exciton lifetime. The TrPL of structure A decays quickest out of the four films which is consistent with the proposition that this structure experiences the most quenching from ZnO. As this QD film is the thinnest, a greater proportion of the photoinduced excitons are within a Förster radius of the ZnO quenching sites. Increasing the QD layer thickness in structure B increases the exciton lifetime since the proportion of QDs within quenching range of the ZnO film decreases. Meanwhile, the addition of a PEI interlayer in structures C and D improves the exciton lifetime further by decreasing ZnO / QD contact area and increasing the distance between the two layers, ultimately leading to nearly identical decay curves. Improving exciton lifetime regardless of QD film thickness indicates that the PEI layer is capable of entirely passivating the ZnO interface to eliminate this source of exciton quenching and leading to an enhancement in QDLED efficiency.

Table 4.1 QD Film Structure and Exciton Lifetime Fitting Parameters

Film	QD Thickness [nm]	PEI Thickness [nm]	τ_1 [ns]	τ_2 [ns]
A	15	0	3.21	8.51
B	30	0	3.78	9.07
C	15	8	4.46	10.55
D	30	8	4.54	10.43
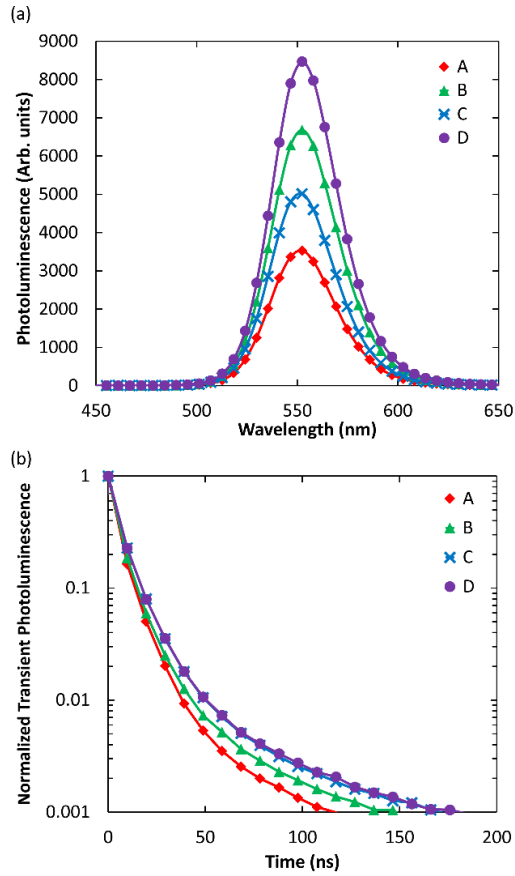
Figure 4.6 (a) Steady-state photoluminescence spectra from an excitation wavelength of 365 nm and (b) transient photoluminescence decay measurements at an emission wavelength of 560 nm for the A (red diamond), B (green triangle), C (blue cross), and D (purple circle) film structures.

Film roughness is an important parameter for good quality devices,[142,168,228] particularly when dealing with the very thin layers utilized in these QDLEDs. Films with large R_{pv} and R_{rms} roughness values can lead to shunts and large leakage currents within the device due to partial circumvention of the QD EML. To further probe the effects of introducing a PEI film into the QDLED structure, and whether the efficiency enhancement may in part be caused by a modification of the surface morphology of ZnO films by the PEI layers, AFM measurements were carried out. **Figure 4.7** presents AFM surface topography scans from a 35 nm ZnO film, and then following a sequential deposition of 8 nm PEI. The ZnO film is not quite as rough as many values reported in literature[23,178,183,223] with 0.9 nm R_{rms} and 10.12 nm R_{pv}, which may be due to the use of a sol-gel ZnO film as opposed to a ZnO nanoparticle film. However, there still remains

many points across the emissive area which will be affected by non-ideal electron injection at the ZnO peaks considering the emission layer is 15 nm thick within the QDLEDs. Sequential deposition of an 8 nm PEI layer reduces both the R_{rms} and R_{pv} to 0.65 nm and 6.54 nm, respectively. This finding is consistent with reports of smoother surface morphology after depositing polymers on nanoparticle films.[124,222,223] This reduction in film roughness through successive PEI deposition on ZnO films may perhaps be the main reason behind the significant reduction of the leakage current in the QDLEDs containing PEI layers observed in **Figure 4.3**(b). The reduction in leakage current may naturally be expected to contribute to the higher EQE attained upon using the PEI interlayer since it would reduce the leakage of unrecombined carriers to the counter electrode.
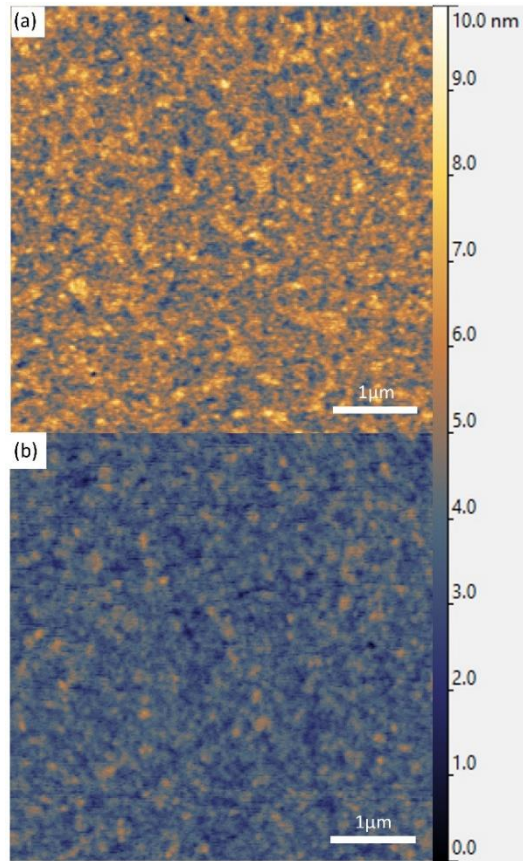
Figure 4.7 AFM images of ZnO film surface (a) before and (b) after coating with an 8 nm PEI film. The measurements are taken over a 5 µm square area with a height range of 10 nm.

While PEI improves device efficiency, its influence on QDLED stability has not yet been established but comes into question given the poorer charge balance within these devices. To this end, luminance and driving voltage of a control QDLED and a device with an 8 nm thick PEI structure were measured during continuous operation at a constant current of 20 mA cm^{-2}. **Figure 4.8** provides the change in normalized luminance (L / L_0) and increase in driving voltage ($V-V_0$) over time. By normalized luminance, the lifetime of the control device appears slightly longer. However, considering that the initial luminance of the PEI-modified device at 20 mA cm^{-2} is 20% greater (3370 cd m^{-2} for the control, and 4180 cd m^{-2} for the PEI interlayer device), the difference between the two lifetimes is negligible. Furthermore, there is an identical increase of 0.22 V for both devices at time of LT50. Thus, the PEI interlayer appears capable of improving QDLED efficiency without affecting stability. Given the shift toward further charge imbalance with the PEI layer, excess electrons do not seem to be the limiting factor to the stability of these devices.

In light of these findings, it can be concluded that electron transport through the device is not inhibited but rather enhanced when PEI is used in QDLEDs. Devices with a FIrpic marking layer exhibit a shift in the recombination zone away from the quantum dots and toward the HTL as PEI thickness increases. Delayed EL measurements confirm that PEI layers result in a greater concentration of residual electrons within the QDLEDs. As PEI thickness increases, the threshold current for efficiency roll-off decreases, providing further evidence that the electron concentration within the EML also increases and promotes Auger recombination. With this in mind, PEI still appears to improve QDLED performance as long as the layers are sufficiently thin and provide a minor increase in electron injection. The observed efficiency improvement despite a shift toward further charge imbalance is therefore attributed to the elimination of quenching via passivation of trap states at the ZnO / QD interface. Presumably, charge balance should be tied to the EL lifetime of QDLEDs, but the devices studied in this work exhibit an insignificant difference in stability compared to QDLEDs without a PEI layer. Although the devices investigated within this work utilized a PEI interlayer, we expect that a similar behavior would be observed for devices incorporating a PEIE interlayer as well given the similarities between the two materials.
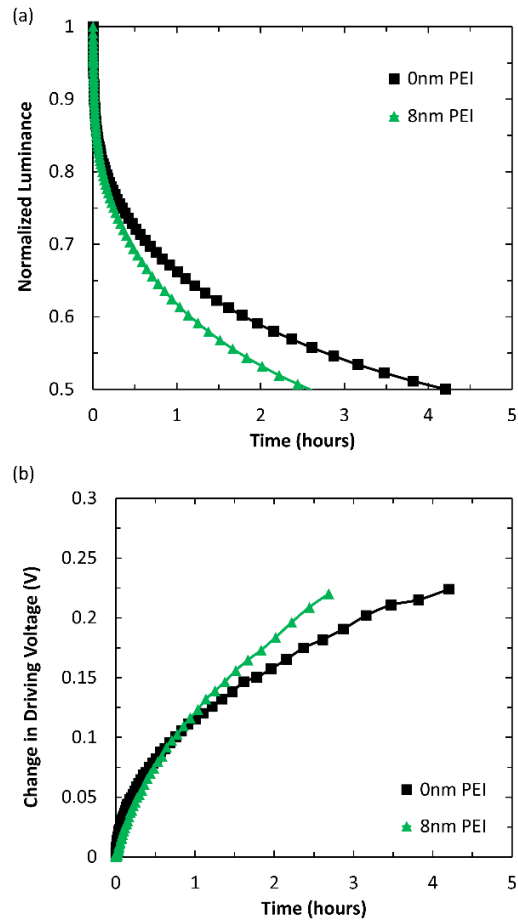
Figure 4.8 The change in luminance normalized to initial values (a) and absolute change in driving voltage (b) for control (black square) and 8 nm PEI EIL (green triangle) devices driven with constant 20 mA cm^{-2} current density. Initial luminance and driving voltage.

4.4   Conclusions

In conclusion, we have studied the effect of using a PEI interlayer in QDLEDs, finding the polymer to increase – rather than reduce – electron injection and thus exacerbate the poor charge balance within the devices. Introducing PEI is found to improve efficiency by up to 60% in QDLEDs over the control structure despite the observed increase in electron injection, but this enhancement cannot be attributed to the poorer charge balance. Although the improvement in the overall efficiency of QDLEDs from the PEI interlayer is accompanied by a rightward shift in JV characteristics compared to the ZnO ETL control device, this does not necessarily correspond to carrier injection within the devices as the driving voltage required for a given electric field increases along with device thickness. Probing the exciton recombination zone via luminescent marking layers shows that the PEI layers induce a shift away from the QD layer and into the HTL which is consistent with the increased electron injection. This has been further corroborated by delayed EL measurements identifying an increase in excess residual charges within devices that incorporate a PEI interlayer. Increasing the thickness of the PEI layer further enhances electron injection, shifting the recombination zone deeper into the HTL. We attribute the observed increase in QDLED efficiency despite the additional charge imbalance to the passivation of ZnO surface states that otherwise effectively quench excitons in the QD EML. Thus, there is a trade-off between PEI thickness and improvement of efficiency whereby thinner layers provide the best enhancement and thicker layers become detrimental to efficiency. Furthermore, an improvement in surface smoothness at the interface controlling electron injection into the QD film contributes to the improved performance through a reduction in leakage current. Although the maximum luminance is only improved by 10% with the inclusion of a PEI interlayer, the largest increase in efficiency occurs over the low driving current regime which is attractive for display applications. Remarkably, the inclusion of a PEI passivation layer does not appear to significantly affect the EL lifetime of QDLEDs indicating that the excess electrons may not be a limiting factor in the stability of such devices. These findings shed light not only on the benefits of using wide band gap interlayers in QDLEDs, but also on key design considerations for realizing enhanced efficiency in these devices.

Chapter 5: The Influence of the Electron Transport and Emission Layers on Morphological Stability of QDLEDs

This work has been published in Davidson-Hall, T., Elbaroudy, A., and Aziz, H., SPIE Optics+Photonics Organic and Hybrid Light Emitting Materials and Devices XXIII, vol. 11093, pp. 1109328, 2019. It has been reproduced with permission from the publisher.

5.1   Introduction

At the time of this work, improvements in device structure and materials had resulted in EQEs as high as 20.5%[124] and LT50 of 300,000 hours[22] for red CdSe-core QDLEDs. While most work on QDLEDs focuses on spherical QDs, the control over particle size and shape allows for the fabrication of rod-shaped shells on the QD core (QD Rods) among other form factors. Of particular interest to QDLEDs, QD Rod films have demonstrated similarly narrow PL emission with a capability for linearly polarized light emission as a result of aspect ratio and molecular alignment due to their unique shape.[163,229,230] Although QDLEDs utilizing QD Rod EMLs have only reached EQEs as high as 15.7%,[176] recent work in double-heterojunction shell QD Rods suggests that they may eventually surpass the performance of spherical QDs in the future.[7] Despite advances in QDLED stability, the lifetime of most QDLEDs remains inadequate for commercial applications.

To understand the limiting factors of QDLED stability, significant attention has been given to reducing charge imbalance and Auger recombination in the QDs which arises from the large energy level mismatch between the valence band of the QD core or shell and the HOMO energy level of the HTL that makes hole injection into the QDs difficult.[22,124,128,129,182,183,227,231] However, additional degradation phenomena within QDLEDs have received comparably minor attention. The standard method of quantifying QDLED stability is to measure the luminance of the device under constant electrical driving and usually comparing the time it takes to reach 50% of the initial luminance. However, when carrying out these measurements on our

QDLEDs we found that dark spot growth and changes in the emissive area appearance would occur regardless of electrical aging or storage in an inert N_2 atmosphere. These findings indicate that there is an inherent morphological influence on the degradation of these devices that must be understood and addressed in order to achieve highly stable QDLEDs. In this work, we have investigated the ETL and EML of the QDLED structure to identify the critical parameters affecting morphological stability.

5.2   Experimental Details

5.2.1   Device Fabrication

The QDLEDs studied here were fabricated on 100 nm thick ITO patterned glass substrates (Kintec) with 20 Ω $\square^{-1}$ sheet resistance, cleaned and sonicated sequentially with Micro 90, DI water, and IPA solutions before treating with O_2 plasma for 5 min. Our standard QDLED structure is ITO (100 nm) / ZnO (32 nm) / QD (50 nm) or QD Rod (15 nm) / CBP (60 nm) / MoO_3 (5 nm) / Al (100 nm), and the devices studied in this work will modify select layers by either replacing the material with another or varying the thickness and anneal temperature. 32 nm ZnO sol-gel films were prepared by adding 197 mg ZnAc (Sigma-Aldrich) to 54 µL MEA (Sigma-Aldrich) in 6 mL ethanol and mixing at 800 RPM for 40 min and a temperature of 45 ºC. The ZnO solutions were filtered through a 0.22 µm polypropylene filter, spincoated at a rotational speed of 1000 RPM for 60 s, and annealed at 150 ºC for 30 min. Red CdSe / ZnS QDs (Mesolight Inc. Cd-QLED-630, with 74% PLQY and size of approximately 10-12 nm diameter, passivated with hexadecylphosphonic acid ligands) with a peak EL emission wavelength of 626 nm and 18 nm FWHM were diluted to 4.17 mg mL^{-1} in octane, spincoated at a rotational speed of 500 RPM for 60 s, then annealed at 50 ºC for 30 min. Red CdSe / CdS QD Rods (Strem Chemicals #48-1059, with > 80% PLQY and size of approximately 5 nm diameter $\times$ 20 nm width, passivated with hexadecylphosphonic acid ligands) with a peak EL emission wavelength of 626 nm and 40 nm FWHM were diluted to 0.6 mg mL^{-1} in octane, spincoated at a rotational speed of 2000 RPM for 60 s, then annealed at 50 ºC for 30 min. The CBP (Angstrom Engineering), MoO_3 (Angstrom Engineering), and Al (Angstrom Engineering) were deposited at a rate of 0.1-2 Å s^{-1} in an Angstrom Engineering EvoVac thermal evaporation chamber at a base pressure of 5×10^{-6} Torr.

5.2.2 Device Characterization

Luminance of the QDLEDs was measured with a Minolta Chroma Meter CS-100, and JVL measurements were carried out via an Agilent 4155C Semiconductor Parameter Analyzer connected to a silicon photodiode. EL images of the QDLEDs during operation at 20 mA cm^{-2} current density were taken by a Google Pixel 2 camera through a Leica StereoZoom4 optical microscope with 30× magnification. The QDLEDs were kept in a N$_2$ atmosphere during all device tests. A Veeco Nanoscope AFM is used for nanoscale morphology characterization.

5.3   Results and Discussion

Although their aspect ratio imparts beneficial optical properties, the alignment of QD Rods can significantly increase film roughness and non-aligned films can have large interparticle distances.[232,233] Thus, in the interest of understanding the effect of the EML on morphological stability of QDLEDs, the size and shape of the QDs is a natural point of comparison. However, film thickness is another characteristic to consider for its influence of over QDLED efficiency, a parameter of equal importance as device stability. For all QDLEDs investigated in this work, devices with QD EMLs are more efficient than with QD Rods and have greater luminescence stability under constant electrical aging.

QDLEDs with varying thicknesses of QD (20 nm, 35 nm, 50 nm) and QD Rod (15 nm, 30 nm, 45 nm) films were fabricated in the standard device structure in order to identify the influence of the EML on QDLED morphological stability. The optoelectronic performance of the QDLEDs can be found in **Figure 5.1**. In general, the QDLEDs have the same turn-on voltage except for the 15 nm QD Rod device which has a slightly lower turn-on voltage. Furthermore, the JV characteristics of the QDLEDs are also very similar except for the 50 nm QD device which has poorer charge transport and the 15 nm QD Rod device which has improved charge transport. Thus, charge transport through the QDLEDs appears to improve as the EML thickness decreases for both QDs and QD Rods as evidenced by the sharper increase in currents at a given driving voltage. While the JV characteristics of the QD and QD Rod devices are similar, their efficiency exhibits opposite trends. For the QD devices, the current efficiency increases by 20% from a maximum of 10.3 cd A^{-1} to 12.3 cd A^{-1} as the EML thickness increases from 20 nm to 50 nm. Meanwhile, the current efficiency of QD Rod devices increases by 80% from 4.0 cd A^{-1} to 7.3 cd A^{-1} as the EML thickness decreases from 45 nm to 15 nm.

Initially, the 2 mm × 2 mm QDLED emissive area is homogeneous for both QD and QD Rod EMLs. While **Figure 5.1**(c) only depicts the emissive area for QDLEDs with a 20 nm QD and 15 nm QD Rod layer, the initial emissive area is uniform for all device structures investigated in this work. **Figure 5.1**(d)

shows the emissive area for the various EMLs after 120 hours of N$_2$ storage along with sample AFM images of the EML films. The roughness is very similar for 20 nm (3.86 nm RMS roughness) and 35 nm (3.87 nm RMS) for the QD films but decreases slightly for 50 nm (3.49 nm RMS). Conversely, the roughness of QD Rod films increases as the thickness increases from 15 nm (3.23 nm RMS) to 30 nm (3.87 nm RMS) to 45 nm (5.48 nm RMS). This trend in roughness follows the trend in dark spot growth for both type of EMLs, as the 50 nm QD and 15 nm QD Rod devices have far fewer dark spots when compared to the other devices. Conveniently, the QDLEDs that achieve optimal performance are the devices with the smoothest EML morphology and best emissive area stability. The AFM images of the QD Rods indicate that there is some degree of agglomeration within the EML that is not present in the QDs, which increases in severity as the thickness increases. However, this does not appear to have a significant effect on the emissive area stability as there is less dark spot coverage in the QD Rod devices compared to the QD EML.
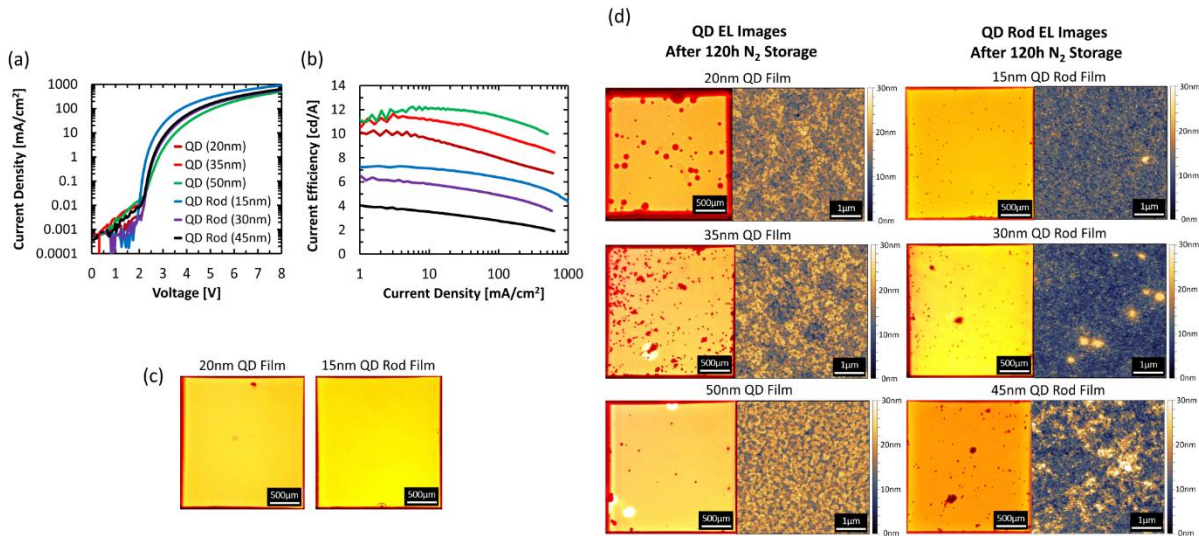
Figure 5.1 (a) Current density-voltage and (b) Current efficiency-current density curves for QDLEDs with varying thickness of QDs (20 nm, 35 nm, 50 nm) and QD Rods (15 nm, 30 nm, 45 nm). (c) Initial EL images of the emissive area for QDLEDs with a 20 nm QD layer and a 15 nm QD Rod layer. (d) Emissive area EL images of QDLEDs with varying thickness of QD (20 nm, 35 nm, 50 nm) and QD Rod (15 nm, 30 nm, 45 nm) EMLs after 120 hours of storage in a N$_2$ atmosphere and AFM images of each QD and QD Rod film.

Knowing that the EML morphology influences the intrinsic degradation of the QDLED emissive area, it is natural to suspect that the underlying ETL will also have an impact as a template for the subsequent depositions. To identify the influence of the ETL on QDLED morphological stability, QDLEDs with varying thicknesses of ZnO (15 nm, 24 nm, 32 nm, 41 nm, 50 nm) and annealing temperature (120 °C, 150 °C, 180 °C for 32 nm thickness) were fabricated with both QD and QD Rod EMLs. The optoelectronic performance of the QDLEDs with varying ZnO thickness can be found in **Figure 5.2**. For QD devices, increasing ZnO thickness appears to have little effect on the JV characteristics of QDLEDs aside from the leakage current at sub-turn on voltages. Although there is some variation to the degree of leakage current, it appears that in general increasing the ZnO thickness will also lead to increased leakage current, particularly for the 50 nm ZnO layer. The opposite trend is observed for QD Rod devices where increased ZnO thickness leads to a decrease in leakage current, but also a reduction in charge transport through the QDLEDs. These contrasting trends indicate that there is a difference in the mechanisms governing operation in the two sets of QDLEDs, especially after taking into account the optimal EML thickness differences between the devices. The ZnS shell of the QDs introduces a much larger energy barrier to injection compared to the CdS shell of the QD Rods which would be expected to reduce charge transport through the QD layer. However, the size and shape of the QD Rods can result in a more disordered film with larger rod-to-rod spacing if a good molecular alignment has not been achieved which can also negatively impact charge transport. Further, the thin QD Rod layer may be more susceptible to changes in the ETL whereas the thick QD layer has more of an influence over charge transport compared to that of the ETL. Both QD and QD Rod devices experience an increase in current efficiency with increasing ZnO thickness with the exception of the 50 nm QD device which may be adversely affected by the significant leakage current observed in this QDLED. For devices with a QD EML, a large leakage current is observed to reduce the current efficiency in the low current density regime where the leakage current dominates charge transport leading to more non-radiative recombination of excitons. However, at sufficiently high current density the current efficiency of these devices recovers.
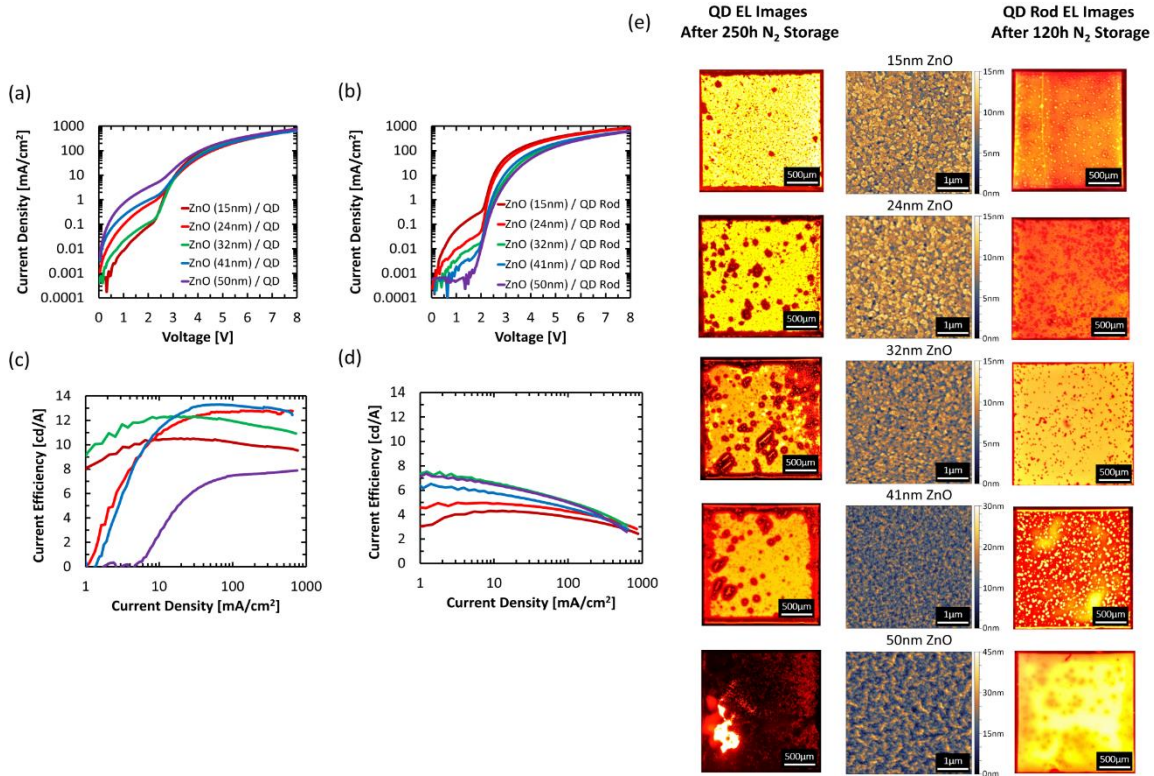
Figure 5.2 Current density-voltage curves for QDLEDs with varying thickness of the ZnO ETL (15 nm, 24 nm, 32 nm, 41 nm, 50 nm) and: (a) a 50 nm QD EML or (b) a 15 nm QD Rod EML. Current efficiency-current density curves for QDLEDs with varying thickness of the ZnO ETL (15 nm, 24 nm, 32 nm, 41 nm, 50 nm) and: (c) a 50 nm QD EML or (d) a 15 nm QD Rod EML. (e) Emissive area EL images of QDLEDs with varying ZnO ETL thickness (15 nm, 24 nm, 32 nm, 41 nm, 50 nm) and a 50 nm QD EML after 250 hours of storage in a N_2 atmosphere, or with a 15 nm QD Rod EML after 120 hours of storage in a N_2 atmosphere and AFM images of the ZnO surface for a given thickness.

Figure 5.2(e) shows the emissive area for the QDLEDs with various ZnO thicknesses after 250 hours of N_2 storage for devices with a QD EML and after 120 hours of N_2 storage for devices with a QD Rod EML, along with sample AFM images of the ZnO films. The roughness of ZnO films is generally consistent between 15 nm (1.92 nm RMS), 24 nm (1.81 nm RMS), and 32 nm (1.66 nm RMS) but begins to increase significantly as the ZnO thickness reaches 41 nm (3.89 nm RMS) and 50 nm (10.14 nm RMS). The 32 nm ZnO film is the smoothest by a slim margin, which may be a result of reaching sufficient thickness to smooth out the roughness of the underlying ITO film (2.81 nm RMS). While the thinner ZnO films are only slightly rougher than the 32 nm film, the thicker films are very rough. In this case, thick ZnO sol-gel films may not be as viable due to poor film quality. This notion is reflected in the EL images of the QDLEDs

88

where the thickest ZnO films exhibit a significant emissive area inhomogeneity. For the QD EML, most of the device area is non-emissive while the QD Rod emissive area appears hazy with bright and dark domains. As the ZnO thickness increases, so too does the degree of emissive area homogeneity degradation in QD devices. Interestingly, the 32 nm ZnO film is the only one in which the QD Rod EML retains some emissive area homogeneity. Thus, while the increase in ETL roughness does not appear to influence the QDLED optoelectronic characteristics there is a significant impact on the emissive area stability of the QD Rod devices.

The other ZnO parameter of interest with respect to the ETL influence on the morphological stability of QDLEDs is the annealing temperature. High annealing temperatures are acceptable for inverted devices fabricated on glass substrates but can degrade plastic substrates in flexible devices or the underlying organic and emissive layers in conventional device architectures. Optoelectronic performance of the QDLEDs with varying ZnO anneal temperatures can be found in **Figure 5.3**. For both QD and QD Rod devices, the annealing temperature of ZnO has little effect on charge transport through the QDLEDs and the QD Rod devices exhibit less leakage current. Meanwhile, the annealing temperature has a significant impact on the efficiency of QDLEDs. Increasing the annealing temperature results in a decrease in maximum current efficiency from 13.8 cd A^{-1} at 120 ºC to 12.3 cd A^{-1} at 150 ºC to 8.8 cd A^{-1} at 180 ºC for QD devices and 7.8 cd A^{-1} to 6.6 cd A^{-1} to 3.4 cd A^{-1} for QD Rod devices. Without a corresponding change in charge transport within these devices, the decreasing efficiency of these QDLEDs is likely a result of increased exciton quenching by ZnO at the ZnO / EML interface.
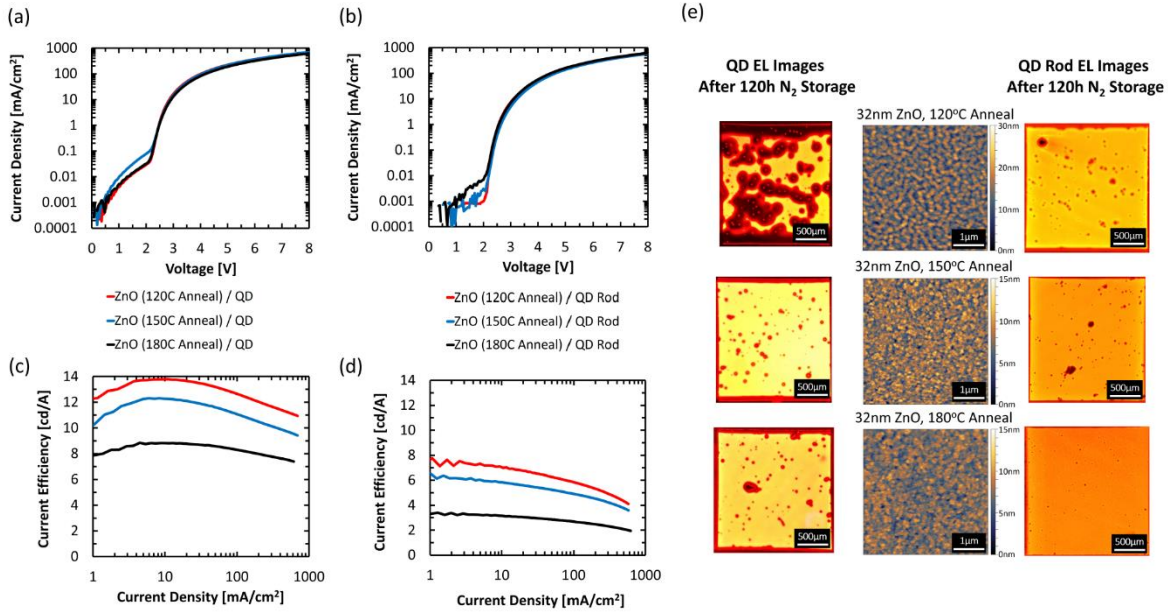
Figure 5.3 Current density-voltage curves for QDLEDs with a 32 nm ZnO ETL annealed at varying temperature (120 ºC, 150 ºC, 180 ºC) and: (a) a 50 nm QD EML or (b) a 15 nm QD Rod EML. Current efficiency-current density curves for QDLEDs with a 32 nm ZnO ETL annealed at varying temperature (120 ºC, 150 ºC, 180 ºC) and: (c) a 50 nm QD EML or (d) a 15 nm QD Rod EML. (e) Emissive area EL images of QDLEDs with a 32 nm ZnO ETL annealed at varying temperature (120 ºC, 150 ºC, 180 ºC) and a 50 nm QD EML, or a 15 nm QD Rod EML, after 120 hours of storage in a N_2 atmosphere and AFM images of the ZnO surface for a given anneal temperature.

Figure 5.3(e) depicts the QDLED emissive area for the various ZnO anneal temperatures after 120 hours of N_2 storage as well as AFM images of the ZnO films. The roughness of ZnO films is similar for 180 ºC (1.42 nm RMS) and 150 ºC (1.66 nm RMS) anneal temperatures but increases with an annealing temperature of 120 ºC (3.35 nm RMS). This roughness trend correlates with the trend of dark spot growth in the emissive area during N_2 storage, as the 120 ºC annealed ZnO results in much more non-emissive area when compared to the 150 ºC and 180 ºC annealed ZnO. Once again, the QD Rod devices appear to have better stability in the QDLED emissive area when compared to the QD devices. Although the increased roughness of the 120 ºC annealed ZnO does not have an effect on the charge transport characteristics of the QDLEDs, this may also be a contributing factor to the improved efficiency.

Roughness of the EML and ETL appears to be the primary factor behind morphological instability of QDLEDs, where a surface roughness greater than approximately 3.5 nm RMS is a critical threshold that

should not be exceeded. Although the previous sections highlight the sensitivity of QDLED emissive area stability to ETL and EML roughness, it is unlikely that the inorganic layers are experiencing a change in morphology. Meanwhile, organic OSCs are known to have poor intrinsic stability and are prone to crystallization.[13,234–236] Thus, the HTL appears to be the most likely source of this morphological instability.

5.4   Conclusions

We have studied the effect of the EML and ETL on the intrinsic morphological stability of QDLEDs, finding that dark spot growth and emissive area inhomogeneity primarily arise as a consequence of EML and ETL roughness. Degradation of QDLED emissive area homogeneity is observed to progress regardless of electrical driving or storage in an inert nitrogen atmosphere, highlighting the importance of addressing this issue for long-term operation of QDLEDs. EL images of QDLED emissive area after storage in N_2 for several days indicate that roughness of the ZnO and QD (or QD Rod) films is the primary characteristic of the EML and ETL which have an impact on morphological stability of QDLEDs. Despite their asymmetry, it appears that QD Rod films are comparable in roughness to the symmetric QDs but produce more morphologically stable QDLEDs. We suspect that this surface roughness induces crystallization in the organic HTL which leads to dark spots and inhomogeneity in the QDLED emissive area over time.

Chapter 6: The Role of Excitons Within the Hole Transporting Layer in QDLED Degradation

This work has been published in Davidson-Hall, T. and Aziz, H., Nanoscale, vol. 11(17), pp. 8310-8318, 2019. It has been reproduced with permission from the publisher.

6.1   Introduction

Significant progress in developing improved QD materials and device structures, including the use of inorganic (typically ZnO) materials for the electron transport layer and organic materials for the hole transport (HTM) layer, has drastically improved the performance of QDLEDs over the last two decades.[23,81,119,237] In this chapter, the distinction is made between the HTM and the HTL as much of the discussion will focus on the material itself. Nevertheless, the lifetime of most QDLEDs remains inadequate for commercial applications. In addressing the limited stability of QDLEDs, significant attention has been given to reducing charge imbalance and Auger recombination in the QDs, which ensue from defects in the QDs and the large energy level mismatch between the valence band of the QD core or shell and the HOMO energy level of the HTM that makes hole injection into the QDs difficult.[22,124,128,129,182,183,227,231] Recently, Chang *et al*.[197] pointed to a possible detrimental effect of electrons on HTMs of QDLEDs. Additional degradation phenomena within QDLEDs have received comparably minor attention.

In chapter 4, excitons were found to be present in the HTL under standard operating conditions of QDLEDs. These excitons arise from the drift of electrons past the QD emissive layer and their recombination with holes in the HTL.[171] Knowing that organic materials are susceptible to damage by excitons, a phenomenon that has been found to have a detrimental effect on the stability of organic layers in light-emitting devices,[195,238,239] the possibility of exciton-induced degradation of the HTM playing a role in the limited electroluminescence stability of QDLEDs must be considered. This notion is particularly compelling once the remarkable stability of the other layers is taken into consideration. QDs have exhibited

excellent intrinsic PL stability with recent accelerated aging tests of thick-shelled QD light-converting films retaining 100% of their initial PL intensity after accelerated aging for 9,000 hours, corresponding to a lifetime of 100,000 hours.[110] Meanwhile, ZnO and other metal oxides used as transport materials are known to generally have high chemical and electrical robustness.[22,23,81,216,240]

The objective of this work is to investigate the influence of HTMs on the stability of QDLEDs and to understand the role that excitons play with respect to degradation in these devices. We observe a significant difference in LT50 between QDLEDs that otherwise exhibit equivalent efficiency, charge transport and injection properties. Notably, we find that the PL stability of QDs can change upon changing the HTM (and the latter's susceptibility to damage by excitons), and that a correlation exists between that behavior and the EL stability of the QDLEDs. Although the measurements presented in this work primarily investigate photo-induced excitons, we demonstrate that excitons are similarly formed deep within the HTL during electrical bias, indicating that the same phenomena must also occur during normal QDLED operation. The results therefore reveal that the robustness of the HTM to exciton-induced degradation is a critical factor for QDLED stability.

6.2   Experimental Details

6.2.1   Device Fabrication

The QDLEDs studied here were fabricated on 100 nm thick ITO patterned glass substrates (Kintec) with 20 Ω $\square^{-1}$ sheet resistance, cleaned and sonicated sequentially with Micro 90, DI water, and IPA solutions before treating with O_2 plasma for 5 min. ZnO sol-gel was prepared by adding ZnAc (197 mg, Sigma-Aldrich) to MEA (54 µL, Sigma-Aldrich) in ethanol (6 mL, Sigma-Aldrich) and mixing at 600 RPM for 40 min and a temperature of 45 $^{\circ}$C. The ZnO solutions were filtered through a 0.22 µm polypropylene filter, spincoated at a rotational speed of 1000 RPM for 60 s, and annealed at 180 $^{\circ}$C for 30 min. Red CdSe / CdS quantum dot rods suspended in octane with a peak EL emission wavelength of 630 nm (0.6 mg mL^{-1}, Strem Chemicals #48-1059, with > 80% PLQY and size of approximately 5 nm diameter $\times$ 20 nm width, passivated with hexadecylphosphonic acid ligands) were spincoated at a rotational speed of 2000 RPM for 60 s, then annealed at 50 $^{\circ}$C for 30 min. The same deposition process was used for green CdSe / CdS quantum dot rods with a peak EL emission wavelength of 550 nm (0.6 mg mL^{-1}, Strem Chemicals #48-1053, with > 60% PLQY and size of approximately 5 nm diameter $\times$ 20 nm width, passivated with hexadecylphosphonic acid ligands). The organic CBP (Shanghai Han Feng Chemical Co.), NPB (Shanghai Han Feng Chemical Co.), Spiro-CBP (Luminescence Technology Corp.), 2,6-DCzPPy (EM Index), mCP (Jilin OLED Material Tech Co.), TPBi (Shanghai Han Feng Chemical Co.), TBADN (Luminescence Technology Corp.), DCJTB (Shanghai Han Feng Chemical Co.), MoO_3 HIL (Angstrom Engineering), and aluminum anode (Angstrom Engineering) were deposited at a rate of 0.1-2 Å s^{-1} in an Angstrom Engineering EvoVac thermal evaporation chamber at a base pressure of 5×10^{-6} Torr.

6.2.2 Device Characterization

Luminance of the QDLEDs was measured with a Minolta Chroma Meter CS-100, and JVL measurements were carried out via an Agilent 4155C Semiconductor Parameter Analyzer connected to a silicon photodiode. Spectral measurements of the QDLEDs were measured using an Ocean Optics QE65000 spectrometer. EQEs were calculated as outlined by Okamoto *et al*. assuming a Lambertian emission distribution.[210] PL was induced via irradiation with an Analytik Jena UVL-18 handheld ultraviolet lamp with 370 nm peak emission. TrPL decay was measured with an Edinburgh Instruments FL920 spectrometer equipped with a 375 nm peak emission EPL375 picosecond pulsed laser diode. Electroluminescence lifetime measurements were performed in a Botest Systems GmbH OLT Lifetime Test System with a constant driving current maintained at 20 mA cm^{-2}. During all device tests, aside from TrPL measurements, the QDLEDs were kept in a N_2 atmosphere.
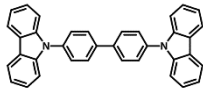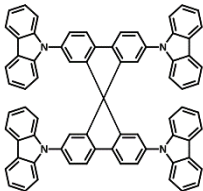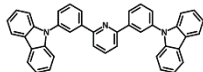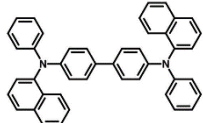
6.3   Results and Discussion

Initial investigations into the role of the hole transporting layer in QDLED stability were carried out by fabricating red-emitting devices with the same structure but different HTMs and comparing their EL performance. The general structure of these devices was: ITO (100 nm) / ZnO (35 nm) / QD (15 nm) / HTM (40 nm) / MoO_3 (5 nm) / Al (100 nm). CBP, Spiro-CBP, 2,6-DCzPPy, NPB, and mCP were selected for use as HTMs due to their range of HOMO energy levels. The key performance characteristics of these devices are detailed in **Table 6.1** along with the molecular structure, glass transition temperature, HOMO and band gap energy of each HTM, followed by the source curves in **Figure 6.1**. Devices utilizing a mCP HTM are omitted from the table and figure as the QDLEDs were inoperable due to the morphological and electrical instability of mCP as a HTM. QDLEDs utilizing CBP as the HTM result in the most efficient devices. The turn-on voltage for the CBP QDLED occurs at a bias roughly coinciding with the 2 eV band gap of a QD with 630 nm luminescence peak emission. Interestingly, the NPB QDLED exhibits a sub-bandgap turn-on voltage which has been attributed to Auger-assisted hole injection.[189] However, in this case the efficiency of such devices is much lower than those that do not exhibit sub-bandgap turn-on voltages, likely due to the shallow HOMO energy level of NPB which limits hole injection into the QDs. 2,6-DCzPPy and Spiro-CBP both produce QDLEDs with higher turn-on and driving voltages (at a current density of 20 mA cm^{-2}), compared to CBP QDLEDs. In the case of 2,6-DCzPPy, lower hole mobility and a deeper HOMO energy level may cause the rightward shift in current density-voltage (JV) characteristics. Given the molecular structure and energy level similarity between CBP and Spiro-CBP, the vast difference in QDLED performance is unexpected but appears to be a result of poor hole injection. Furthermore, the CBP QDLED also exhibits a significantly longer lifetime; an order of magnitude greater than the alternatives despite its higher initial luminance. An examination of the HTM's HOMO and glass transition temperature values reveals no clear correlation between these properties and the QDLED stability trends. There is, however, a weak inverse correlation between the band gap energy and the QDLED EL lifetimes where devices utilizing HTMs with larger band gaps demonstrate lower stability. Previous work has

97

identified a correlation between the band gap energy of organic materials and their propensity to undergo exciton-polaron induced aggregation.[19] Although these results show that the HTM has a significant influence on QDLED performance, the difference in stability may simply be due to variance in charge balance and / or exciton density in view that the devices have different JV and EQE characteristics.

Therefore, to test the effect of different HTMs on the stability of QDLEDs more accurately and rule out the confounding effects of differences in charge balance and / or exciton density, only devices with comparable JV behavior and efficiency should be compared. The efficiency and transport difference between the CBP and Spiro-CBP appears to arise from an injection issue at the Spiro-CBP / MoO_3 interface which can be remedied by introducing a 10 nm interstitial layer of CBP doped with 5% MoO_3. By selecting thicknesses of 30 nm for Spiro-CBP and 50 nm for CBP, the JV curves for both QDLED structures essentially coincide and exhibit almost equal turn-on and driving voltage with minimal leakage current as can be seen in **Figure 6.2**. Although the Spiro-CBP device has a slightly higher maximum EQE and more efficiency roll-off at high current density, the two QDLEDs exhibit similar EQE at 20 mA cm^{-2} driving current density. Given their coinciding characteristics, any differences in stability between these devices will not be primarily due to differences in charge balance or exciton density. **Figure 6.3** presents the EL stability test results from the CBP and Spiro-CBP devices optimized for matching performance, showing the changes in luminance and driving voltage over time at a driving current density of 20 mA cm^{-2}. The initial luminance of the two devices at this driving current were very similar, with values of 1450 cd m^{-2} and 1440 cd m^{-2} for the CBP and Spiro-CBP QDLEDs, respectively. In line with the results covered in **Table 6.1**, the device with a CBP HTM once again exhibits a LT50 that is an order of magnitude longer than that of its counterpart with a Spiro-CBP HTM. The CBP QDLED has a remarkably stable driving voltage throughout the testing period whereas the driving voltage of the Spiro-CBP QDLED structure experiences a rapid increase, especially in the first 3 hours. This rapid increase occurs in the same time frame during which the luminance decreased by 80%. These results indicate that QDLEDs incorporating Spiro-CBP are inherently less stable than comparable devices with CBP as the HTM.

Table 6.1 Notable performance characteristics of QDLEDs with CBP, Spiro-CBP, 2,6-DCzPPy, and NPB hole transporting layers, their molecular structure, glass transition temperature, HOMO and band gap energy

HTM	Molecular Structure	HOMO Energy Level [eV]	Band Gap Energy [eV]	Glass Transition Temperature [°C]	Turn-On Voltage [V]	Performance at 20 mA cm^{-2} Driving Current Density			
						Driving Voltage [V]	Luminance [cd m^{-2}]	EQE [%]	LT50 [h]
CBP		-6.0 [200]	3.1 [200]	62 [241]	2.09	2.82	760	3.5	13
Spiro-CBP		-5.8 [201]	3.4 [201]	240 [242]	4.17	7.68	140	0.7	< 1
2,6-DCzPPy		-6.1 [203]	3.5 [203]	102 [203]	2.82	5.04	340	1.5	< 1
NPB		-5.4 [107]	3.0 [107]	96 [243]	1.49	2.85	60	0.3	N/A

Knowing that excitons can damage organic materials to various extents, we investigate whether the differences in QDLED EL stability upon changing the HTM may be due to exciton-induced degradation effects. To this end, we study the effect of subjecting the QDLEDs with various HTMs to UV irradiation continuously, for 80 hours, while monitoring changes in the intensity of the QD and HTM PL spectra, which would mirror changes in their PLQY. QDLEDs with the general device structure of ITO (100 nm) / ZnO (35 nm) / QD (15 nm) / HTM (40 nm) / MoO$_3$ (5 nm) / Al (100 nm), were fabricated and tested, using CBP, Spiro-CBP, 2,6-DCzPPy, NPB, and mCP HTMs. A UV lamp with peak luminescence at a wavelength of 370 nm was used as an excitation source at an irradiation power of 500 µW cm^{-2}. Excitation at this wavelength can induce the formation of excitons in QDs, CBP, Spiro-CBP and NPB (which all have non-

negligible absorption at 370 nm), producing PL from both the QDs and the HTM in each case. However, there was no detectable HTM PL emission from 2,6-DCzPPy and mCP devices. One example of the spectral intensity change over time is presented in **Figure 6.4**(a) for the CBP QDLED, while similar figures for the other QDLED structures can be found in **Figure 6.5** (Spiro-CBP), **Figure 6.6** (NPB), **Figure 6.7** (2,6-DCzPPy), and **Figure 6.8** (mCP). The trends in QD and HTM peak PL over the entire 80-hour irradiation period can be found in **Figure 6.4**(b) and (c), respectively. To facilitate visualization of the changes in PLQY, the changes in peak intensity are normalized to both the initial intensity at t_0 and the excitation intensity. As can be seen from the figure, the QD PL intensity of the CBP QDLED exhibits a 16% increase in the first 10 hours and then starts to decrease slowly to 106% of the initial intensity by the 80-hour point. In contrast, the QD PL intensity for the NPB device increases rapidly by 40% over the first 10 hours of irradiation and then reaches a plateau at 145% of the initial PL intensity. There is a minor increase of 7% in QD PL intensity over the first few hours with a Spiro-CBP HTM, which gradually decreases to 75% by the end of the 80-hour measurement period. Meanwhile, the QD PL intensity for devices with a 2,6-DCzPPy HTM undergoes minimal changes over the first 10 hours of UV irradiation and ultimately degrades by 10% after 80 hours. Furthermore, the mCP QDLED exhibits an extreme degradation in QD PL by 35% over the initial 10 hours of UV irradiation which begins to slow toward an emission intensity equivalent to 48% of the initial value by the 80-hour mark. The stark difference between the PL trends of the five QDLEDs indicates that the HTM next to the QD layer has a significant influence on QD luminescence behavior over time.
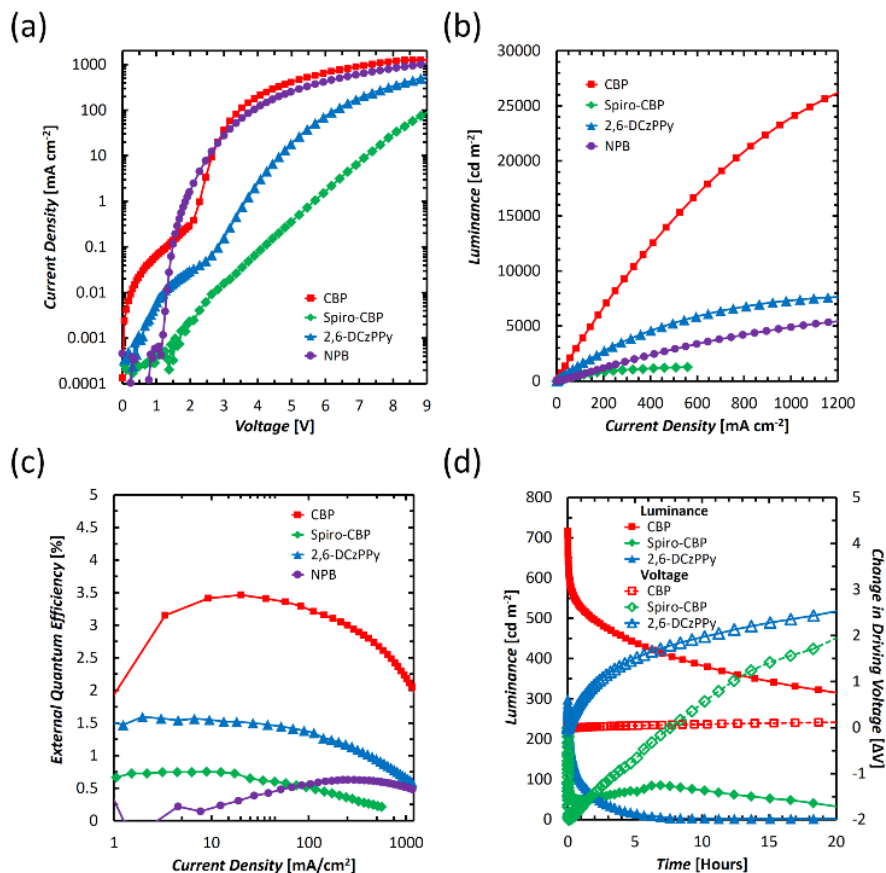
Figure 6.1 (a) Current density *vs.* voltage, (b) Luminance *vs.* current density, (c) EQE *vs.* current density, (d) Luminance (solid) and change in driving voltage (ΔV=V(t)-V$_0$) (dashed) EL lifetime curves for QDLEDs with CBP (red square), Spiro-CBP (green diamond), 2,6-DCzPPy (blue triangle), and NPB (purple circle) HTLs.
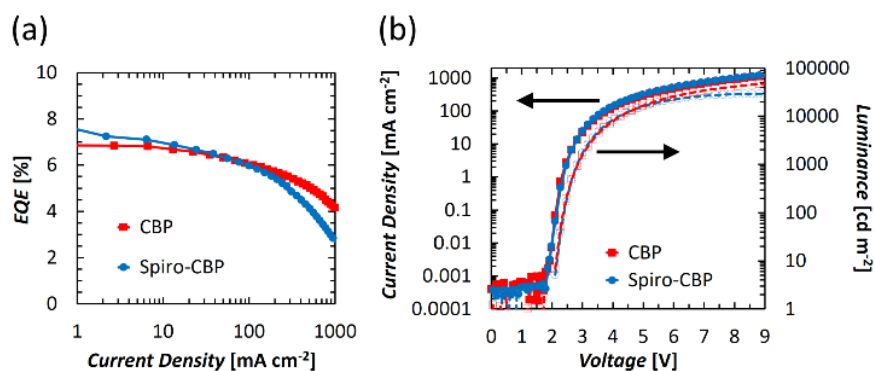
Figure 6.2 (a) EQE *vs.* current density, (b) Luminance (dashed) and current density (solid) *vs.* voltage characteristics for QDLEDs designed for matching performance with CBP (red square) and Spiro-CBP (blue circle) HTMs.
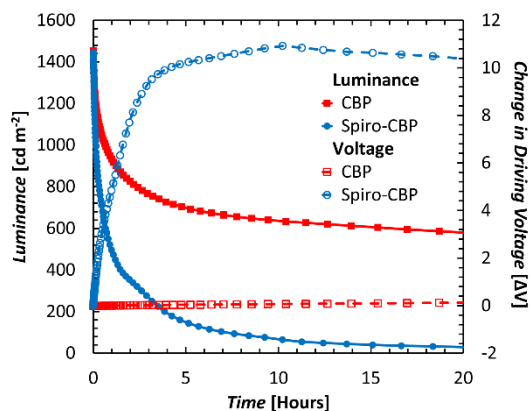
Figure 6.3 EL stability test results from the CBP (red square) and Spiro-CBP (blue square) QDLEDs optimized for matching performance, showing the changes in luminance (solid) and driving voltage ($\Delta V = V(t) - V0$) (dashed) over time at 20 mA cm^{-2} driving current density.

Unlike the trends observed in QD PL, there is a universal decrease in HTM PL intensity over time for the devices in which emission from the HTM could be detected. For CBP, there is a gradual decrease in PL intensity from a 9% decrease in the first 10 hours to a decrease of 25% after 80 hours. Similarly, NPB experiences an initial 7% decrease in PL intensity over 10 hours and decreases by 23% after 80 hours. However, there is a significant decrease in Spiro-CBP PL intensity over that same period, ultimately decreasing to 43% of the initial intensity. Therefore, although the PLQY of all HTMs appears to decrease over time, the magnitude of this decrease varies among the them, with Spiro-CBP exhibiting a much faster degradation in its PLQY compared to either CBP or NPB. The fact that the QD PL also degrades the fastest in case of the Spiro-CBP device and exhibits similar long-term trends for CBP and NPB devices further elucidates upon the influence of the HTMs on the QD layers.
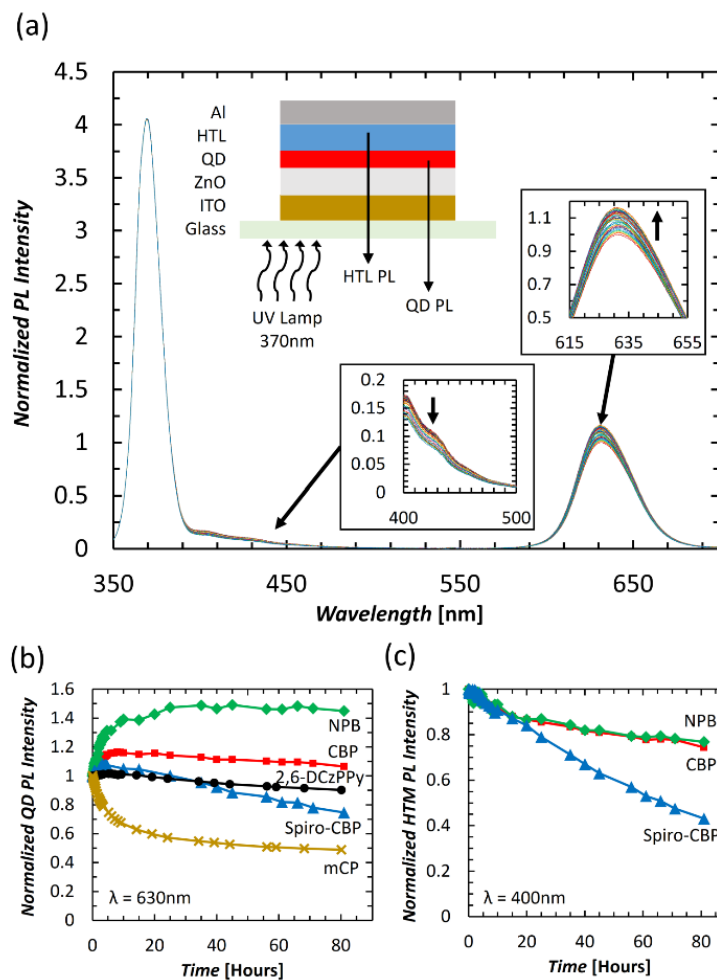
Figure 6.4 (a) PL spectra of a CBP QDLED over 80 hours of constant UV irradiation with insets indicating the device structure and source of measured PL emission (top), the change in measured CBP PL intensity (bottom), and QD PL intensity (right). (b) QD peak PL intensity *vs.* time and (c) HTM peak PL intensity *vs.* time for CBP (red square), NPB (green diamond), Spiro-CBP (blue triangle), 2,6-DCzPPy (black circle), and mCP (gold cross) QDLEDs subjected to constant UV irradiation. The 370 nm band corresponds to the UV excitation peak. 2,6-DCzPPy and mCP HTM bands could not be detected.

Seeing the similar trends of QD PL and HTM PL over time, two additional device configurations are fabricated and tested to further verify the correlation between them. Should the QD PL trend indeed depend on the HTM, one can expect the use of a very wide band gap material that absorbs only negligibly at the UV wavelength, and thus does not degrade appreciably by the UV irradiation, to lead to a more stable QD PL trend over time. Additionally, since any such dependence would be of an interfacial nature between the QD and HTM film, altering only the QD / HTM interface can be expected to strongly influence the QD PL

103

trend. Therefore, in these two devices the HTM was substituted with either 40 nm of TPBi or a Spiro-CBP (10 nm) / TPBi (30 nm) bilayer. The QD peak PL intensity trends of these devices are depicted in **Figure 6.9** and compared to the Spiro-CBP QDLED trend previously discussed while PL spectra source figures for the QDLED structures can be found in **Figure 6.10** (TPBi) and **Figure 6.11** (Spiro-CBP / TPBi). With a TPBi layer next to the QDs, there is a minor improvement in PL intensity by 7% within the first 10 hours followed by a slow decrease to the initial PL intensity over the subsequent 70 hours. Exciton-induced efficiency improvements in QDs have been observed elsewhere and are commonly attributed to photochemical annealing of lattice defects and the stabilization of surface traps.[71,244] Such effects are likely contributing to the QD PL intensity increases observed in **Figure 6.4**(b) as well. As TPBi absorbs negligibly at 370 nm, the small decrease in PL can be attributed to intrinsic UV-induced degradation of the QDs alone. Turning now to data from the Spiro-CBP / TPBi device, one can see that the decrease in QD PL is consistent with the results for Spiro-CBP alone which suggests that exciton-induced degradation of the HTM molecules within the first 10 nm from the QD / HTM interface are the most impactful on QD PL stability. However, the small differences between the two PL degradation trends suggests that there is an additional contribution to this behavior from molecules beyond the first 10 nm.
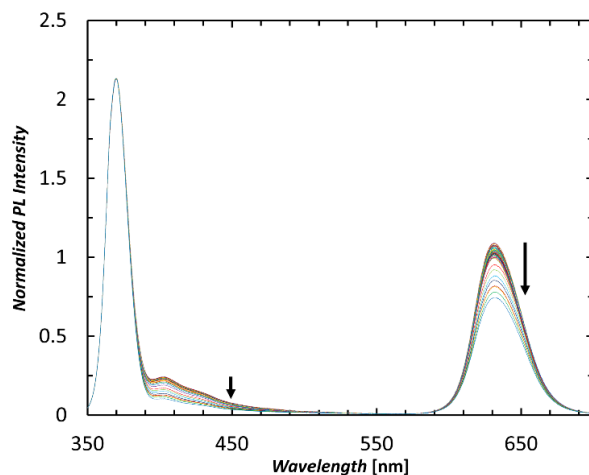
Figure 6.5 PL spectra for a QDLED with a Spiro-CBP HTL over 80 hours of constant UV irradiation.
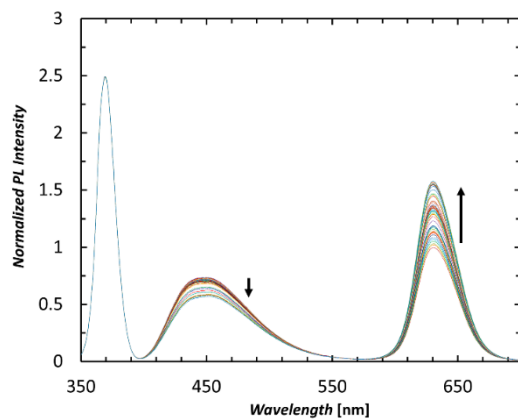
Figure 6.6 PL spectra for a QDLED with a NPB HTL over 80 hours of constant UV irradiation.
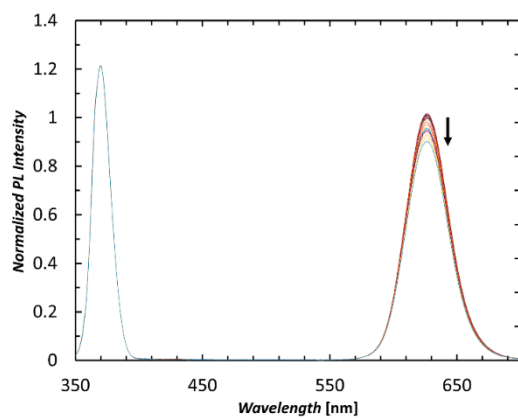
Figure 6.7 PL spectra for a QDLED with a 2,6-DCzPPy HTL over 80 hours of constant UV irradiation.
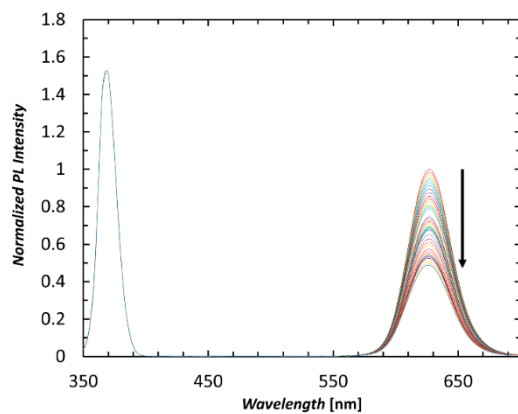
Figure 6.8 PL spectra for a QDLED with a mCP HTL over 80 hours of constant UV irradiation.
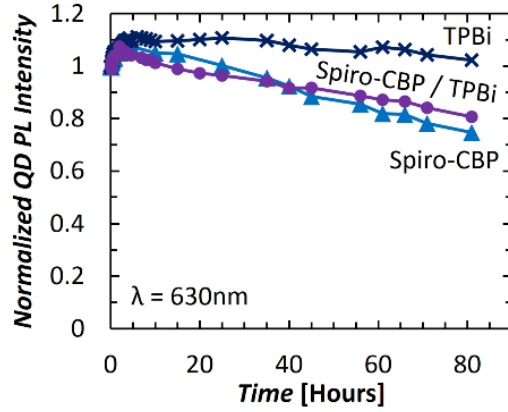
Figure 6.9 QD peak PL intensity *vs.* time for devices with Spiro-CBP (blue triangle), TPBi (dark blue cross), and Spiro-CBP / TPBi (purple circle) layers subjected to constant UV irradiation.
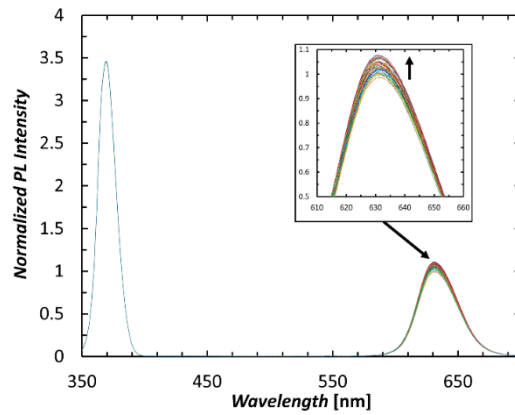
Figure 6.10 PL spectra for a QDLED with a TPBi spacer layer over 80 hours of constant UV irradiation.
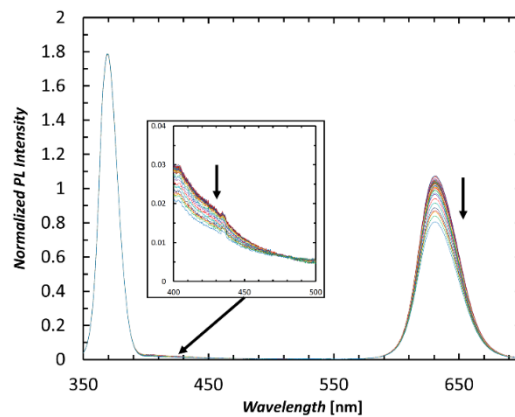
Figure 6.11 PL spectra for a QDLED with a Spiro-CBP / TPBi HTL over 80 hours of constant UV irradiation.

Clearly, since the only variable in the previous device structures is the HTM next to the QD layer, this must be the cause of the differences in the QD PL intensity over time trends among the devices. Furthermore, since this behavior is induced solely by photo-generated excitons, the QD PL degradation can be related directly to the effect of excitons on the HTMs and, as a result, on the PLQY of the QDs within the devices. It becomes therefore interesting to identify the mechanism by which changes in the PLQY of the HTM can affect the PLQY of the QDs and whether energy transfer between the two layers might be involved. Taking QD and HTM PL intensity behavior of the devices into consideration, two distinct trends can be identified. In the case of CBP and NPB QDLEDs, the QD PL intensity for both increases initially whereas the HTM PL intensity decreases which may be indicative of an improvement in transfer of excitons from the HTM to the QDs. Due to the short radius of energy transfer for excitons located on the HTM, this phenomenon will be highly dependent on the QD / HTM interface morphology. Although UV irradiation increases the surface temperature of the glass substrate by only 2 °C, excitation of the HTM molecules may supply enough energy to induce an effect similar to interface annealing that reduces the distance between the QDs and the HTM molecules. Annealing QDLEDs has been shown to improve energy transfer from a phosphorescent sensitizer to QDs due to a similar effect in literature.[188] The remarkable increase in QD PL intensity when next to NPB (much more than when next to TPBi, the latter being a case where there is necessarily no energy transfer from the organic material to the QD since TPBi does not absorb at 370 nm) suggests that there may be a significant contribution of QD PL due to energy transfer from NPB, which appears to become more efficient over time. Moreover, that the QD PL intensity does not appear to decrease for this QD / HTM combination may be indicative of an improved stability of devices incorporating NPB whereas even the CBP QDLED experienced some degree of QD PL deterioration after UV irradiation for 80 hours. While the NPB QDLEDs exhibit poor efficiency in our initial investigation, energy transfer may be a significant contributing factor to the high efficiency reported by Mashford *et al.*[82] upon using a NPB derivative. Similarly, the superior efficiency and EL stability of CBP QDLEDs is accompanied by an increase in QD PL intensity during UV irradiation, again providing evidence of a possible increase in energy transfer over time. In contrast, Spiro-CBP devices experience only a slight initial increase in QD PL

intensity in comparison, followed by much more rapid degradation than that observed with CBP, NPB, and 2,6-DCzPPy. While the initial increase in QD PL intensity may be due to increased energy transfer from Spiro-CBP to QDs, the long-term decrease in intensity may be attributed to the higher susceptibility of Spiro-CBP to exciton-induced degradation.[19] This results in the formation of quenching sites in the Spiro-CBP, which may quench the QDs in their vicinity, ultimately reducing the overall PLQY of the QD layer. Possible avenues of exciton-induced degradation in organic molecules include molecular aggregation[18,19,194] and chemical decomposition.[15,245,246] The former is accelerated by exciton-polaron interactions. While we do not expect optical excitation to produce a high concentration of polarons in the devices studied in this work, a recent report has observed polarons in a host-guest system due to the dissociation of excitons,[247] a mechanism that may help accelerate exciton-induced degradation. As both molecular aggregation and chemical decomposition lead to a deterioration of the HTM PLQY, QD PLQY and overall QDLED efficiency will also decrease. Although the effect of UV irradiation could not be analyzed for 2,6-DCzPPy and mCP HTMs with a 370 nm UV source, the degradation in QD PL intensity over time also corresponds to the observed trend in QDLED stability investigated earlier. QDLEDs with a mCP HTM did not live long enough to measure their performance before shorting, exhibiting extremely poor EL stability considerably worse than Spiro-CBP QDLEDs.

To further verify the conclusions drawn above regarding the influence of the exciton-induced degradation of HTMs on QD PLQY, we study the PL stability of separate QD and HTM films. For this purpose, 40 nm thick HTM films (of the same materials as before) coated on glass substrates directly and 15 nm thick QD films coated on top of 35 nm thick ZnO films on glass were fabricated and tested. All films underwent the same UV irradiation as the previous devices. The resulting PL peak intensity versus time curves, again normalized to the initial value at t_0, are depicted in **Figure 6.12** along with inset schematic depictions of the investigated sample structures, with PL spectra source curves in **Figure 6.13** (ZnO / QD) and **Figure 6.14** (CBP, NPB, Spiro-CBP, and Spiro-CBP / TPBi). The QD PL intensity from the ZnO / QD bilayer film increases by 5% over the first 10 hours with little change over the remaining 70 hours. In order

to compare this with the PL stability trend of the TPBi device considered earlier, the data is replotted in **Figure 6.12**(a). The two curves are remarkably similar as both experience a minor increase in QD PL over the first 10 hours of UV irradiation without significant degradation over the following 70 hours. This verifies that the presence of TPBi indeed has negligible effect on the QDs and little influence on PL stability. In contrast, and much like in the case of the QDLEDs, there is a distinguishable difference between the PL intensity of Spiro-CBP films and the other HTMs. Both CBP and NPB films exhibit minimal change in their PL over time, whereas PL from the Spiro-CBP and Spiro-CBP / TPBi films degrades by 9% and 13% over 80 hours of UV irradiation, respectively. It should be noted that these samples lack the reflective metal anode of the QDLEDs which may be a factor behind the slower degradation rate of the Spiro-CBP film compared to the Spiro-CBP QDLED in **Figure 6.4**. In this case, incident UV light only passes through the HTL once instead of multiple times within the weak microcavity of a QDLED. Nevertheless, these trends again show the higher susceptibility of Spiro-CBP to exciton-induced degradation compared to the NPB and CBP films.
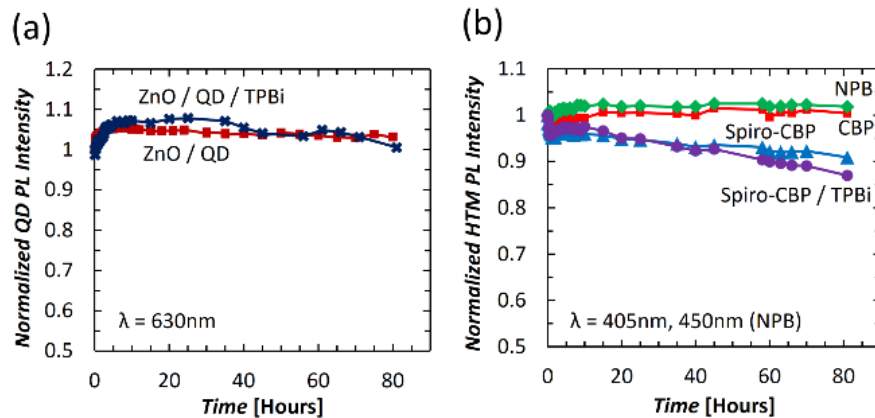
Figure 6.12 Peak PL intensity *vs.* time for the following films subjected to constant UV irradiation with 370 nm peak wavelength: (a) QD PL of a QD film deposited on ZnO (dark red square) and the QDLED structure with TPBi (dark blue cross); (b) HTM PL of CBP (red square), NPB (green diamond), Spiro-CBP (blue triangle), and Spiro-CBP / TPBi (purple circle) films deposited on glass.
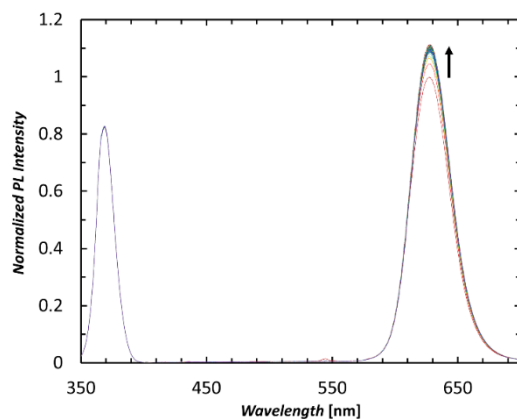
Figure 6.13 PL spectra for a QD film deposited on ZnO over 80 hours of constant UV irradiation.

We have hypothesized above that the initial increase in QD luminescence when in contact with NPB and CBP may be due to improved energy transfer from the HTL caused by an interface-annealing effect that leads to an increase in molecular density and proximity to the QDs. We have also proposed that the faster decline in QD PL when in contact with Spiro-CBP to exciton-induced degradation of the HTM that leads to a reduction in energy transfer from the HTL to the QD and / or the formation of sites that quench QD excitons due to energy transfer in the opposite direction (i.e. from the QDs to the HTM). Such processes however require that energy transfer between the QD and HTM molecules is efficient; an assumption that may be questionable given the QD shell thickness and ligand length. Therefore, to investigate the possibility of energy transfer from the HTM to QD, we fabricated structures consisting of 10 nm and 20 nm films of CBP, NPB, or Spiro-CBP deposited on a 15 nm QD film or alone on a glass substrate to investigate the energy transfer dynamics. TrPL measurements were performed on these films to investigate the time-resolved exciton recombination within the HTLs, which are presented in **Figure 6.15**. The TrPL results indicate that the exciton lifetime in the HTLs is shorter when in contact with QDs, consistent with energy transfer to QDs. There is also a clear relation between HTL thickness and exciton lifetime where thicker layers exhibit a longer exciton lifetime. This is expected since a greater number of excitons are created far enough away from QDs for energy transfer to occur. There is once again a similarity between CBP and NPB on QDs where the exciton lifetime of the 20 nm layers on QDs is only slightly longer than that of the

110

10 nm layers and both are shorter than the same films deposited on glass. The small increase in exciton lifetime indicates that the FRET radius of energy transfer from CBP and NPB to the QD film may be rather large (> 10 nm) such that increasing the HTL thickness results in energy transfer from these distant molecules. Conversely, the exciton lifetime for the 20 nm Spiro-CBP layer next to QDs is equivalent to those of the Spiro-CBP films deposited on glass whereas that of the 10 nm Spiro-CBP layer on the QD film is shorter. This trend in TrPL is indicative of a shorter FRET radius and suggests that, unlike the case of CBP and NPB, energy transfer from Spiro-CBP to the QD layer occurs almost exclusively from within the 10 nm slice directly in contact with the QDs.
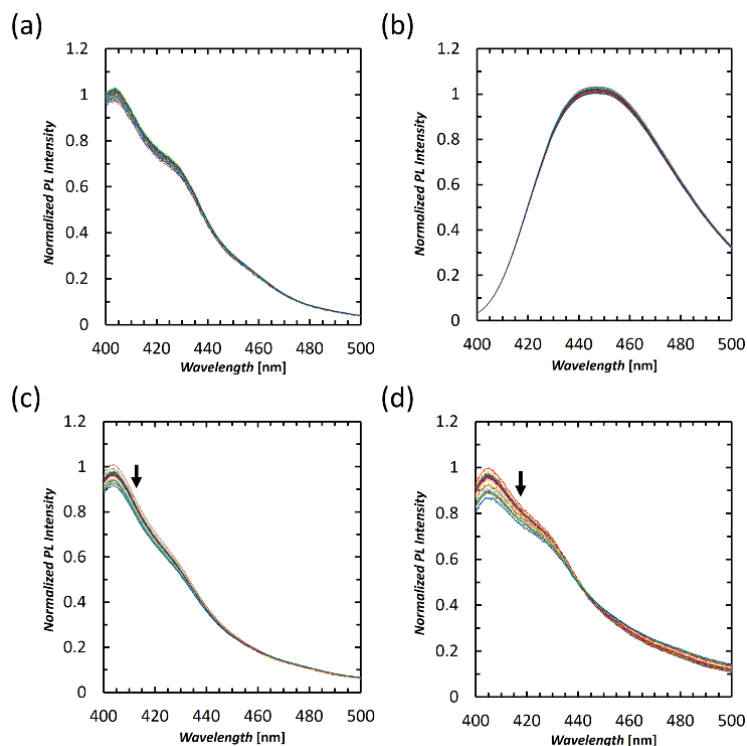
Figure 6.14 PL spectra for films of (a) CBP, (b) NPB, (c) Spiro-CBP, and (d) Spiro-CBP / TPBi over 80 hours of constant UV irradiation.

Having verified that efficient energy transfer from the HTL to the QD can indeed occur, we then investigate if energy transfer from the QD to possible quenchers within the HTL can also occur. For this purpose, two device structures utilizing green QDs deposited on a ZnO film followed by a layer composed

of either CBP alone or CBP doped with 20% DCJTB are studied. The red fluorescent emitter DCJTB is used as a model quencher owing to the sufficient overlap of its absorption spectrum and emission spectra of the QDs and CBP. Furthermore, due to the distinguishability of the green QDs and DCJTB PL spectra, the influence of the quenching layer on QD exciton lifetime can be observed. TrPL results from these samples are presented in **Figure 6.15**(d). Clearly a significant decrease in exciton lifetime of the green QDs when DCJTB is present in the HTM is observed, which indicates that QD excitons can be quenched by quenchers in the HTL. The results therefore prove that the formation of quenchers in the HTL, which may result of exciton-induced degradation, can indeed adversely affect the PLQY of the QDs.
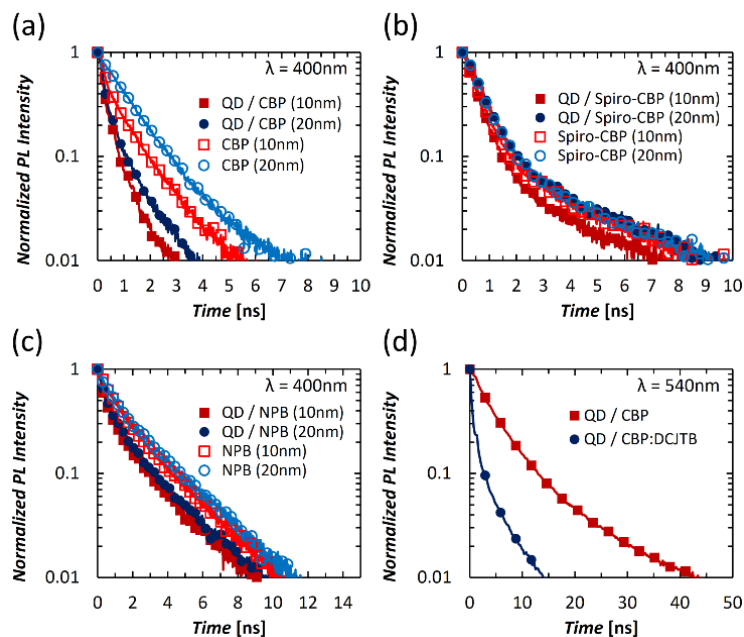
Figure 6.15 TrPL measurements for 10 nm (red square) and 20 nm (blue circle) films of (a) CBP, (b) Spiro-CBP, and (c) NPB deposited on glass with (dark, filled) and without (light, dashed) a QD layer in between. (d) TrPL measurements for green QDs deposited on ZnO with a subsequent CBP (dark red square) and CBP:DCJTB (dark blue circle) layer.

In the previous PL experiments, the UV irradiation results in the formation of excitons throughout the QD and HTLs of the QDLEDs. It becomes therefore important to determine if exciton formation under normal QDLED electrical driving similarly extends into the HTL. We have shown in chapter 4 that exciton

formation extends to at least 5 nm into the HTL from the QD / HTL interface, and that increasing electron injection from the ZnO will lead to an increase in their concentration within this slice.[171] To further investigate the extent of exciton formation within the HTL of QDLEDs under electrical driving, we fabricate and test QDLEDs that contain a fluorescent marking layer placed at different locations in their HTMs. TBADN, a blue fluorescent organic emitter with an emission peak of 460 nm and negligible overlap with the QD emission peak, is selected as the fluorescent marker. It has a HOMO energy level close to that of CBP (-5.8 eV and -6.0 eV for TBADN and CBP, respectively)[208,248] and therefore does not significantly trap holes or perturb charge transport in CBP. The general structure of the QDLEDs was ZnO (35 nm) / QD (15 nm) / CBP (x nm) / 90% CBP: 10% TBADN (5 nm) / CBP (35-x nm) / MoO_3 (5 nm) / Al (100 nm) for x values of 0, 10, 20, and 30. A reference device without a marking layer was also included for comparison. The EL spectra of these devices, normalized to the QD emission peak, are presented in **Figure 6.16**. There is a trend of decreasing TBADN EL intensity as the marking layer moves away from the QD / HTM interface from 0.5% of the QD peak intensity at 0 nm, to 0.3% at 10 nm away, and 0.1% at 20 nm and 30 nm away. However, even at 20 nm and 30 nm away from the QD layer, emission from TBADN can still be detected which indicates that excitons are created well into the HTL. That excitons can be formed well into the HTL during normal electrical driving of the QDLEDs indicates that exciton-induced degradation of HTLs must play a critical role in limiting their EL stability.
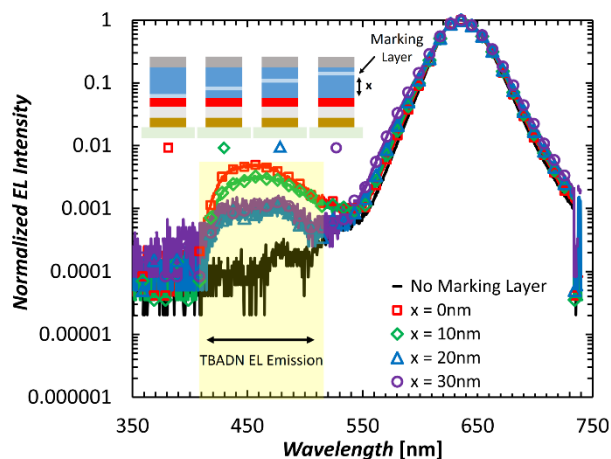
Figure 6.16 EL spectra of QDLEDs (normalized to the QD peak emission) with a TBADN marking layer inserted at 0 nm (red square), 10 nm (green diamond), 20 nm (blue triangle), and 30 nm (purple circle) within the CBP and compared to a control device without a TBADN marking layer (black).

The work presented here shows that exciton damage of the HTM can lead to significant degradation in the PLQY of QDs. Exciton-induced degradation of the HTM may lead to the generation of quenching sites at the QD / HTL interface, ultimately resulting in the non-radiative recombination of excitons and a loss of QDLED efficiency. These sites can quench QDs in their vicinity via energy transfer, thereby reducing the PLQY of the QD layer. Although these effects were demonstrated under stress by excitons only, we know that the presence of charges during normal electrical driving of these devices will accelerate HTM degradation due to exciton-polaron interactions.[18,19,192,249] These results nevertheless indicate that excitons alone can have an impact on QDLED stability in addition to the established degradation processes related to charge imbalance, defects, and Auger recombination. Furthermore, devices with otherwise identical performance may have significantly different EL stability due to the susceptibility of the HTM to exciton-induced degradation. Thus, not only are the energy levels and mobility of the HTL critical considerations for the design of QDLEDs, but the robustness of the HTM to exciton-induced degradation is also of vital importance for the long-term stability of QDLEDs.

6.4　Conclusions

We have studied the effect of exciton damage of the HTM on QDLED stability. Results show a correlation between the exciton-induced degradation of the HTM and poor device EL stability. The PLQY stability of QDs depends strongly on the chosen HTM, which are susceptible to degradation by excitons at different rates. Energy transfer from QDs to quenching molecules in the HTL may play a role in this effect, representing a pathway through which degradation of the HTM can negatively impact QD PLQY over time. The findings show that aside from its influence on device efficiency, energy transfer from the HTM to QDs is also an important factor to be considered for more stable QDLEDs. We identify that excitons are present deep within the HTL under typical bias conditions, indicating that exciton-induced degradation of the HTM is likely to contribute to poor QDLED stability. These findings reveal a new degradation mechanism centred around the HTL and its influence on QDLED stability.

Chapter 7: Improving QDLED Stability via the Implementation of a Cascading Hole Transport Layer

This work has been published in Davidson-Hall, T. and Aziz, H., ACS Appl. Mater. Interfaces, vol. 12(14), pp. 16782-16791, 2020. It has been reproduced with permission from the publisher.

7.1   Introduction

Improvements in QDLED stability are largely attributed to reducing charge imbalance and Auger recombination in the QDs, which arise from the large energy level mismatch between the valence band of the QD and the HOMO energy level of the HTL that makes hole injection into the QDs difficult.[22,70,121,124,128,129,182,183,231] Fabrication of QDs with thick shells and a graded compositional transition from core to shell has been successful in limiting the effects of non-radiative Auger recombination on QDLED performance.[22,78,123,148,177] In chapter 6, we have identified exciton-induced damage of the HTL as an important factor in QD PLQY degradation over time.[198] Chang *et al.* have also attributed the long-term luminance degradation of QDLEDs to degradation of the HTL.[197] Many QDLEDs with thermally evaporated HTLs utilize CBP because of its deep HOMO energy level and good hole mobility, which helps maximize hole injection into the deep valence band energy levels of QDs, leading to improved performance.[23,123,127–129,171,187,188,197,250] However, the low glass transition temperature of CBP (62 ℃)[241] raises questions regarding the long-term stability of such QDLEDs.

In this work, we utilize a cascading HTL (CHTL) structure with consecutive steps in the HOMO energy levels of each component which allows for good energy level matching at the QD / HTL interface for optimal hole injection while also introducing a more optimal hole transporting scenario for improved stability. We show that the CHTL can improve QDLED LT50 by 25×. Using this approach, we have obtained a LT50 of 864,000 hours for red QDLEDs using a conventional core / shell QD emitter while also

increasing the EQE to 11.1% compared to a device utilizing CBP alone as the HTL. Although there have been several reports of bilayer stepwise HTLs that demonstrate improvements in QDLED performance,[107,124,186,130,133,134,150,182–185] we have found that a three-layer CHTL utilizing CBP, TCTA, and NPB allows for fine control over hole accumulation and electron-hole recombination in QDLEDs. To the best of our knowledge, this represents the longest LT50 for QDLEDs utilizing conventional core / shell QDs, suggesting further stability enhancements may be possible if graded core-shell QDs are used in this QDLED architecture.

7.2 Experimental Details

7.2.1 Device Fabrication

The QDLEDs studied in this work were fabricated on 100 nm thick ITO patterned glass substrates (Kintec) with 20 Ω $\square^{-1}$ sheet resistance, cleaned and sonicated sequentially with Micro 90, DI water, and IPA solutions before treating with O_2 plasma for 5 min. ZnO sol-gel was prepared by adding ZnAc (197 mg, Sigma-Aldrich) to MEA (54 µL, Sigma-Aldrich) in ethanol (6 mL, Sigma-Aldrich) and mixing at 800 RPM for 40 min and a temperature of 45 ºC. The ZnO solutions were filtered through a 0.22 µm polypropylene filter, spincoated at a rotational speed of 1000 RPM for 60 s, and annealed at 150 ºC for 30 min. Red CdSe / ZnS quantum dots suspended in octane with a peak EL emission wavelength of 630 nm (4.17 mg mL^{-1}, Mesolight Inc. Cd-QLED-630, with 74% PLQY and approximately 10-12 nm in diameter, passivated with a mixture of oleic acid and octanethiol ligands) were spincoated at a rotational speed of 500 RPM for 60 s, then annealed at 50 ºC for 30 min. The organic CBP (Angstrom Engineering), NPB (Angstrom Engineering), TCTA (Luminescence Technology Corp.), FIrpic (Luminescence Technology Corp.), HATCN (Angstrom Engineering), MoO_3 (Angstrom Engineering), and Al anode (Angstrom Engineering) were deposited at a rate of 0.1-2 Å s^{-1} in an Angstrom Engineering EvoVac thermal evaporation chamber at a base pressure of 5×10^{-6} Torr.

7.2.2 Device Characterization

Luminance of the QDLEDs was measured with a Minolta Chroma Meter CS-100, and JVL measurements were carried out *via* an Agilent 4155C Semiconductor Parameter Analyzer connected to a silicon photodiode. Spectral measurements of the QDLEDs were measured using an Ocean Optics QE65000 spectrometer. EQE was calculated as outlined by Okamoto *et al.* assuming a Lambertian emission

distribution.[210] PL was induced *via* irradiation with a Newport 67005 200 W HgXe Arc Lamp equipped with a Jobin Yvon adjustable monochromator. EL lifetime measurements were performed in a Botest Systems GmbH OLT Lifetime Test System with a constant driving current maintained at 20 mA cm^{-2}. Time-resolved delayed EL signal was measured with a R928 photomultiplier tube, amplified by a Keithley 428 Current Amplifier and recorded by a Tektronix TDS5054 Digital Phosphor Oscilloscope. Forward and reverse bias signals for delayed EL tests were supplied by a custom-built operational amplifier driven by a Stanford Research Systems DG535 Digital Delay / Pulse Generator connected to a ThorLabs MC1000A Optical Chopper to eliminate the prompt EL signal. QDLEDs were stored in a N_2 atmosphere during all device tests.

7.3   Results and Discussion

Initial investigations into the effect of the HTL on QDLED performance were carried out by fabricating red-emitting devices with the following inverted structure: ITO (100 nm) / ZnO (35 nm) / QD (40 nm) / HTL (60 nm) / HIL / Al (100 nm). The HTL consists of a CBP (40 nm) / TCTA (10 nm) / NPB (10 nm) CHTL structure with either a MoO_3 (5 nm) or HATCN (10 nm) HIL to compare to the conventional QDLED with a CBP HTL and MoO_3 HIL. The energy level diagram of the device is depicted in **Figure 7.1**(a). Although CBP is used as a HTL for its very deep HOMO energy level (-6.0 eV) compared to TCTA (-5.7 eV) and NPB (-5.4 eV),[200] the barrier to hole injection at the QD / CBP interface is still much greater than the barrier to electron injection at the ZnO / QD interface. The mismatch in electron and hole injection efficiency inevitably leads to a charge imbalance within QDLEDs and an accumulation of holes in the HTL in the immediate vicinity of its interface with the QD layer, a phenomenon which is believed to be one of the main contributors to poor efficiency and degradation *via* non-radiative Auger recombination. The MoO_3 HIL is commonly used in organic and QDLEDs due to its very deep Fermi level, allowing for better hole injection into HTLs with deep HOMO energy levels such as CBP.[251] In contrast, the CHTL devices allow for the utilization of a wider variety of alternate HILs including those with shallower energy levels, such as HATCN, which would otherwise be difficult to use in order to avoid a large hole injection barrier at the HTL / HIL interface. **Figure 7.1**(b) and (c) depict the EL characteristics of the CBP / MoO_3, CHTL / MoO_3, and CHTL / HATCN QDLEDs. There is a distinct difference between the current density *vs.* voltage characteristics of the CBP device and CHTL devices where the CBP device exhibits both a lower turn-on voltage and increased charge transport (seen in the higher current at a given driving voltage) compared to the CHTL devices. In contrast, there is a much smaller difference in the charge transport characteristics between the CHTL devices as the HIL is changed from MoO_3 to HATCN, indicating that the characteristics are more strongly governed by hole transport across the HTL than by hole injection from the contact. The CHTL / HATCN device has a slightly lower turn-on voltage than the CHTL / MoO_3 device, likely due to better energy level alignment at the NPB / HIL interface. Although there is a slightly increased turn-on

voltage for the CHTL / MoO_3 device, it exhibits somewhat higher charge transport at higher driving voltages. Furthermore, the QDLEDs with MoO_3 HILs also have much higher leakage current than the CHTL / HATCN device. The luminance *vs.* voltage characteristics generally follow the same trends as their current density *vs.* voltage counterparts. The CHTL / HATCN devices exhibit the greatest maximum EQE (9.8%) compared to CBP / MoO_3 (9.4%) and CHTL / MoO_3 (9.0%), an effect that may be associated with their lower leakage current. Nevertheless, the three device architectures generally have comparable efficiency. CBP (60 nm) / HATCN and TCTA (40 nm) / NPB (20 nm) / HATCN devices were also investigated but resulted in comparably poor performance due to the large hole injection barriers from HATCN to CBP and from TCTA to the QD EML, as can be seen in **Figure 7.2**. **Figure 7.1**(d) shows that the EL spectra of the three QDLED structures have the same QD emission band, however there is a difference in a small emission band with a peak between 400 nm and 440 nm which can be attributed to emission from the HTL. The QDLEDs with a MoO_3 HIL have a similar HTL EL emission peak at 400 nm while the HATCN device has a HTL EL peak at 440 nm. The HTL EL band in the CBP / MoO_3 device can be directly attributed to CBP since it is the only source of blue emission in this device. However, the overlap of the emission spectra of CBP and TCTA, as shown in **Figure 7.3**, makes it difficult to determine if the HTL EL band of the CHTL / MoO_3 device arises from CBP, TCTA, or both. The appearance of a HTL EL band at a longer wavelength in the CHTL / HATCN device indicates that there is a large component of NPB emission, suggesting that there is a shift in electron-hole recombination zone away from the QD / CBP interface, likely due to the more difficult hole transport observed for the CHTL. This relative HTL contribution to the EL spectrum has negligible dependence on the driving voltage for both the CBP / MoO_3 and CHTL / HATCN QDLEDs in the range between 4 V and 7 V, as shown in **Figure 7.4**. Given the similarities in charge transport between the two CHTL devices, it follows that significant electron-hole recombination may also be occurring at the TCTA / NPB interface of the CHTL / MoO_3 device but that the resulting excitons are quenched by MoO_3 resulting in the absence of NPB emission in the EL spectrum.
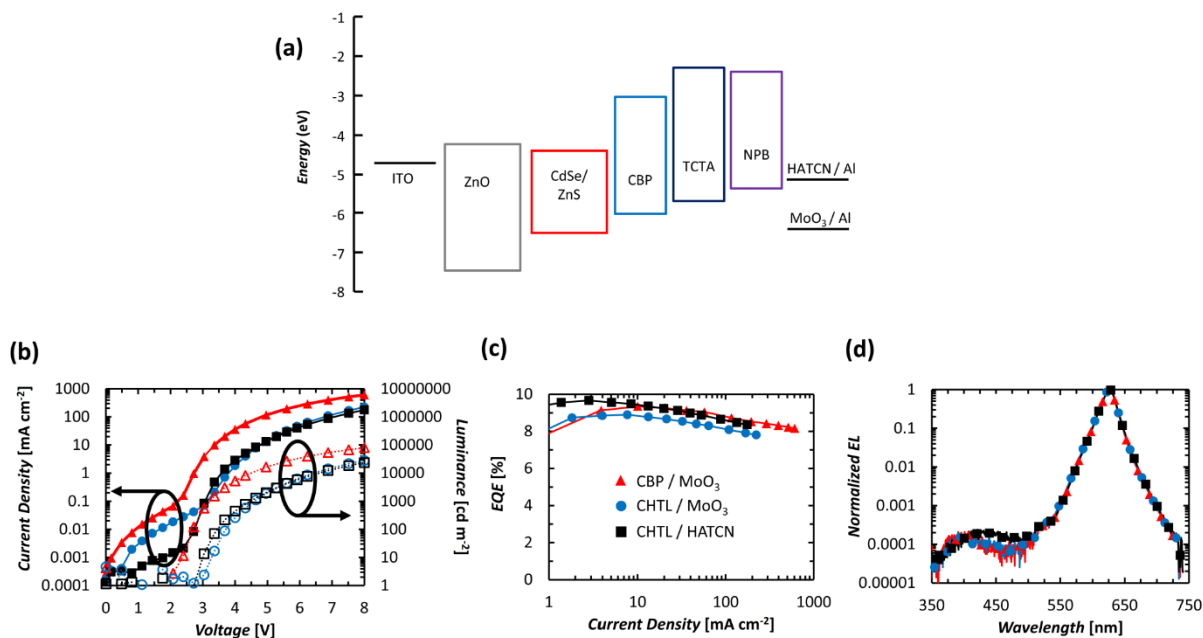
Figure 7.1 (a) Energy level diagram of the materials utilized in the QDLEDs in this work with energy levels taken from literature,[26,183,200,251] (b) Current density (solid) and luminance (dotted) *vs.* voltage characteristics, (c) EQE *vs.* current density characteristics, and (d) Normalized EL spectra of the CBP / MoO$_3$ (triangle), CHTL / MoO$_3$ (circle), and CHTL / HATCN (square) QDLEDs. The EL spectra are measured while driving the QDLEDs at 20 mA cm^{-2} current density which corresponds to driving voltages of 3.68 V, 5.22 V, and 5.28 V, respectively.
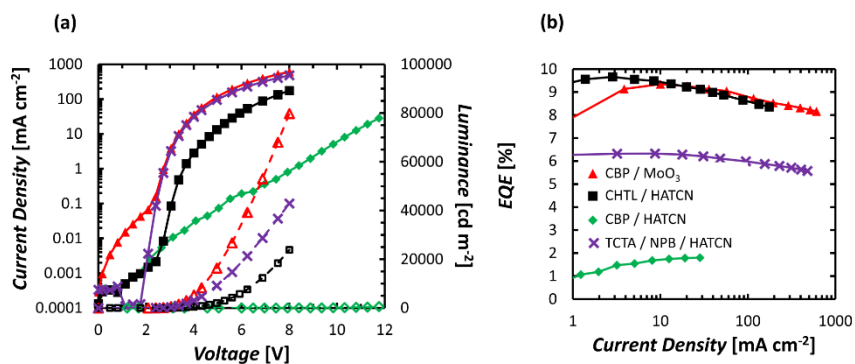
Figure 7.2 (a) Current density (solid) and luminance (dashed) *vs.* voltage and (b) EQE *vs.* current density characteristics of the CBP / MoO$_3$ (triangle), CHTL / HATCN (square), CBP / HATCN (diamond), and TCTA / NPB / HATCN (cross) QDLEDs.

122
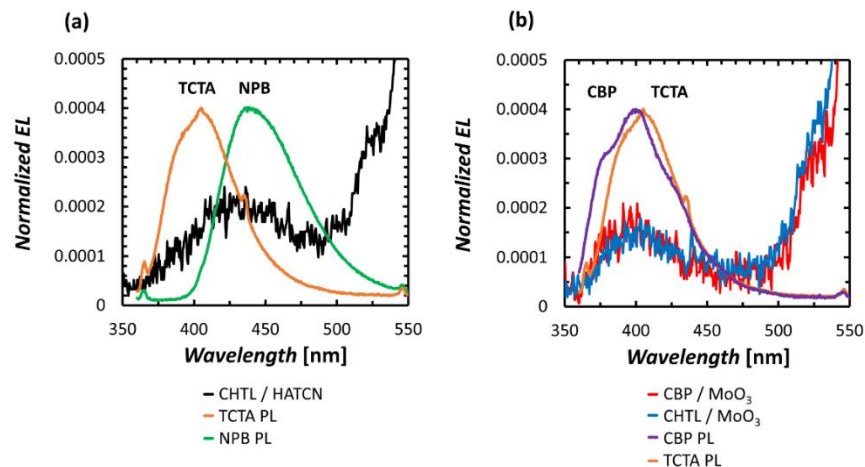
Figure 7.3 Zoomed-in EL spectra of HTL emission from (a) CHTL / HATCN (black) and (b) CBP / MoO₃ (red) and CHTL / MoO₃ (blue) QDLEDs, compared to the PL emission of TCTA (orange), NPB (green), and CBP (purple). The EL spectrum has been normalized to the maximum emission value of the QD peak wavelength.
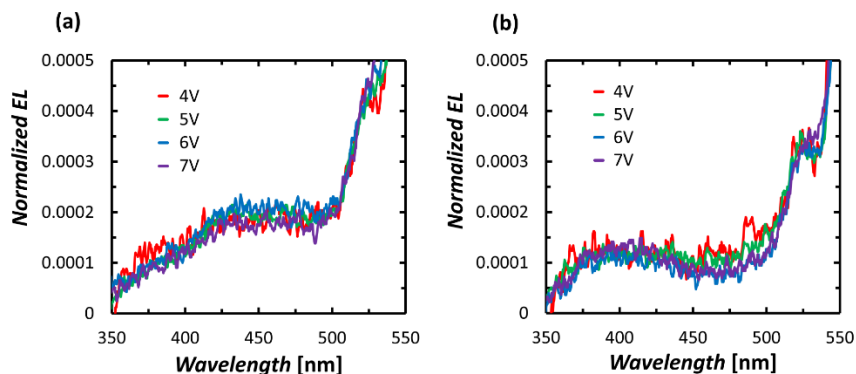
Figure 7.4 EL Spectra of HTL emission from (a) CHTL / HATCN and (b) CBP / MoO₃ QDLEDs, driven at 4 V (red), 5 V (green), 6 V (blue), and 7 V (purple) bias. The EL spectrum has been normalized to the maximum emission value of the QD peak wavelength.

Although the CHTL devices have comparable efficiency to the conventional CBP / MoO₃ device, this coincides with reduced hole transport and therefore expectedly inferior charge balance considering that hole injection from the HTL to the QD layer is generally established to be a limiting factor in QDLED performance. While it is surprising for a QDLED to be efficient despite poor charge balance, one can expect such a device to be less stable under electrical bias due to an increase in the non-radiative recombination processes leading to degradation of the QDs and organic HTL. With that expectation, we investigate the stability of the CHTL devices to understand the full impact of charge imbalance on QDLEDs. **Figure 7.5**

123

depicts the changes in luminance and driving voltage for CBP / MoO_3, CHTL / MoO_3, and CHTL / HATCN devices over time under continuous electrical driving at 20 mA cm^{-2}. Surprisingly, the CHTL / HATCN device is far more stable than either CBP / MoO_3 or CHTL / MoO_3 devices. The CHTL / HATCN device exhibits a LT50, of 825 hours (for a L_0 of 3,445 cd m^{-2}). This corresponds to a LT50 of 482,000 hours at a L_0 of 100 cd m^{-2} using the lifetime relation of $L_0^n LT50 = L_1^n LT50$ where n is the acceleration factor of 1.8 frequently calculated for QDLEDs.[28,78,115,116] The CHTL / HATCN LT50 is 15× longer than the 72 hour LT50 of CBP / MoO_3 (for a L_0 of 3,020 cd m^{-2}) which corresponds to a LT50 of 33,200 hours for a L_0 of 100 cd m^{-2} and 53× longer than the 31 hour LT50 of CHTL / MoO_3 hours (for a L_0 of 2,355 cd m^{-2}) which corresponds to a LT50 of 9,140 hours for a L_0 of 100 cd m^{-2}. The change in driving voltage (the driving voltage for the QDLED at a given time subtracted by its initial driving voltage) *vs.* time trends exhibit an opposite behavior with the CHTL / HATCN device showing the fastest increase in driving voltage over time. While driving voltage increases by 0.17 V over 31 hours in the CHTL / MoO_3 device, and by 0.54 V over 72 hours in the CBP / MoO_3 device, the driving voltage of the CHTL / HATCN device increases by 1.1 V over 31 hours, by 2.1 V over 72 hours, and by 7.8 V over the entire 825 hour period. Such an increase in driving voltage suggests that there is a significant buildup of charges in the CHTL / HATCN QDLED.
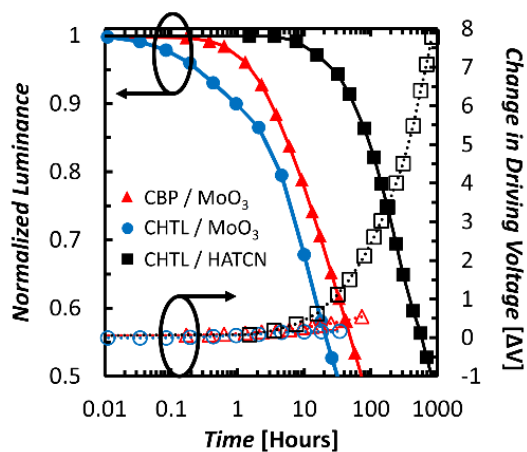
Figure 7.5 Normalized luminance *vs.* time (solid) and change in driving voltage *vs.* time (dotted) characteristics of the CBP / MoO_3 (triangle), CHTL / MoO_3 (circle), and CHTL / HATCN (square) QDLEDs under constant electrical driving at 20 mA cm^{-2} current density.

Clearly, the CHTL / MoO₃ and CHTL / HATCN devices have vastly different degradation behaviors in both luminance and voltage over time despite having similar charge transport and efficiency. This indicates that the HIL plays a significant role in the stability of QDLEDs, and that an improvement in stability can be achieved by utilizing a CHTL to allow for the substitution of MoO_3 with HATCN due to the shallow HOMO energy level of NPB. In fact, the CBP / MoO_3 device is more stable than the CHTL / MoO_3 device which suggests that the NPB / MoO_3 interface may be less stable than the CBP / MoO_3 interface. Given the poor performance of the CBP / HATCN QDLED, this device architecture is not suitable for comparison with the good stability of CHTL / HATCN devices. The EL stability of the bilayer HTL TCTA / NPB / HATCN QDLED depicted in **Figure 7.6** further illustrates the benefit of switching from MoO_3 to a HATCN HIL despite its comparably poor efficiency, exhibiting a LT50 of 570 hours (for L_0 = 2010 cd m^{-2}) which corresponds to an LT50 of 126,000 hours for a L_0 of 100 cd m^{-2}. Therefore, the improvement in EL stability is attributed to both the CHTL structure and the use of HATCN as a HIL. MoO_3 is widely used in upright device architectures where the bottom contact is the hole injecting contact, as opposed to the inverted structure utilized in these QDLEDs. In that case, MoO_3 will be deposited on ITO instead of on an organic HTL. In a study of inverted OLEDs, Zhao *et al.* reported that MoO_3 can penetrate into organic HTLs with depths proportional to the latter's thermal properties.[252] This phenomenon will lead to MoO_3-doping of the HTL and an increase in hole transport, but the high temperature deposition of MoO_3 may lead to thermal stresses in the underlying HTLs that contribute to the poor stability of the CBP / MoO_3 and CHTL / MoO_3 devices. In contrast, since HATCN is an organic material and can be evaporated at a lower temperature, thermal-induced degradation of the underlying layers is reduced. The critical question to answer, however, is what causes the large increase in driving voltage of the CHTL / HATCN device over time. In a multilayer HTL, one can expect hole conduction to be impeded by the hole injection barriers at the interlayer interfaces resulting from differences in the HOMO energy levels of the various materials. Hole transport across the CHTL therefore will not occur until the electric field at each interlayer interface is high enough to overcome the injection barrier. In this context, holes injected into the NPB layer will accumulate at the TCTA / NPB interface until the electric field across the remaining HTL thickness

becomes sufficient to overcome the energy barrier. The same process repeats at the CBP / TCTA interface. In both CHTL devices, the voltage required to overcome the hole accumulation at each interface is much greater than in the case of a CBP / MoO$_3$ interface which leads to their increased turn-on voltage. While the thermal doping of MoO$_3$ into CBP allows for hole injection with negligible energy barrier, each inter-layer interface of the CHTL introduces an injection barrier of approximately 0.3 eV due to the cascading HOMO energy levels of NPB (-5.4 eV), TCTA (-5.7 eV) and CBP (-6.0 eV).[200] Under steady-state conditions, holes accumulating at the QD / CBP interface reduce the electric field across the CBP layer and holes begin to accumulate at the CBP / TCTA and TCTA / NPB until the accumulated holes at the QD / CBP interface are depleted. Thus, the EL stability improvement observed in the CHTL / HATCN QDLED may be associated with a reduction in hole accumulation at the QD / HTL interface as a result of their accumulation at the other HTL interfaces further away from the QD layer. A schematic depiction of the differences between the steady-state charge accumulation of holes at the interfaces of each HTL within the CBP / MoO$_3$, CHTL / HATCN, and TCTA / NPB / HATCN QDLEDs is illustrated in **Figure 7.7**. The significant accumulation of holes further away from the QD / CBP interface in the CHTL / HATCN device is also consistent with the faster increase in driving voltage *vs.* time as a greater electric field is required to overcome the hole injection barriers.
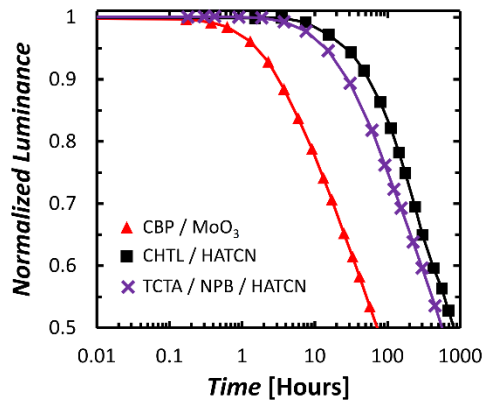
Figure 7.6 Normalized luminance vs. time characteristics of the CBP / MoO$_3$ (triangle), CHTL / HATCN (square), and TCTA / NPB / HATCN (cross) QDLEDs. The EL stability measurements were carried out under constant electrical driving at 20 mA cm^{-2} current density.
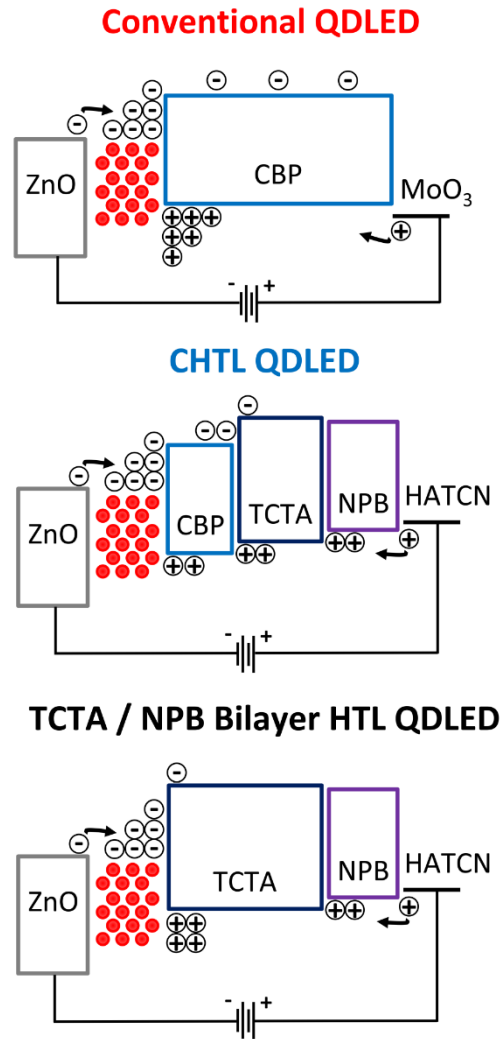
Figure 7.7 Charge accumulation schematic of CBP / MoO$_3$, CHTL / HATCN, and TCTA / NPB / HATCN QDLEDs under forward bias.

In order to better elucidate the effect of the CHTL and MoO$_3$ on QDLED performance and stability, hole-only devices containing the same HTLs were prepared and tested. The hole-only devices had the same structure as the QDLEDs except that the ZnO layer was substituted with another MoO$_3$ layer. The second MoO$_3$ layer restricts electron injection from the ITO cathode into the QD layer due to the deep Fermi level of MoO$_3$, resulting in the transport of only holes injected from the Al when the devices are under positive bias relative to the ITO. The current density *vs.* voltage characteristics of the three hole-only devices are presented in **Figure 7.8**, showing that they generally follow the same trend in charge transport observed in

Figure 7.1. The onset of conduction in the CBP hole-only device occurs at a lower voltage than either of the two CHTL devices with an order of magnitude greater current density at all driving voltages. In all three devices, the QD / CBP injection barrier limits the conduction of current across the devices and once the internal electric field increases enough to overcome this barrier the current density then rapidly increases at a rate of $J \propto V^n$ where J is current density, V is voltage, and n is equal to 12, consistent with trap-limited conduction where $n \geq 2$.[253] This onset however occurs at a higher voltage for the CHTL devices which can be ascribed to the successive hole injection barriers at the CBP / TCTA and TCTA / NPB interfaces. The difference in conduction onset voltages between CHTL / HATCN and CHTL / MoO$_3$ devices confirms that hole injection into NPB is more efficient from HATCN than it is from MoO$_3$. Nevertheless, at higher applied voltages the hole transport characteristics of the two CHTL devices become very similar and all three hole-only devices exhibit similar trap-limited current *vs.* voltage dependence trends with n equal to 5. Electrical aging measurements of the CBP / MoO$_3$ and CHTL / HATCN hole-only devices were performed by measuring the increase in driving voltage over time when driven at 20 mA cm^{-2} current density to help glean some insights into the effect of holes on the stability of the QDLEDs and are presented in **Figure 7.8**(b). Interestingly, the driving voltage *vs.* time trends for the hole-only devices follows an opposite order to that of the QDLEDs that were presented in **Figure 7.5**. Over the 50 hour period, the driving voltage of the CHTL / HATCN hole-only device experiences an increase of only 0.09 V which is much lower than in its corresponding QDLED. Meanwhile, the increase in driving voltage of the CBP / MoO$_3$ hole-only device was 0.50 V, similar to the driving voltage increase observed from the CBP / MoO$_3$ QDLEDs. This indicates that the fast increase in driving voltage of the CHTL-based QDLED occurs through a different mechanism than that in the CBP / MoO$_3$ device. The fast increase in voltage in the CHTL QDLED but not in the case of the corresponding hole-only device suggests that the behavior is caused by exciton-polaron interactions that are known to degrade organic / organic interfaces and result in similar increases in driving voltage.[16,17,19,192–195,254] The exciton-polaron degradation is exacerbated by the accumulation of holes at the inter-layer interfaces within the CHTL. The absence of excitons in the hole-only device limits this degradation process and, consequently, the device experiences a minimal increase in driving voltage under

constant electrical driving. On the other hand, the increase in driving voltage over time for the CBP hole-only and QDLEDs can be attributed in part to the damage caused by the high temperature thermal evaporation of the MoO_3 layer, although exciton-polaron interactions are expected to lead to degradation in the CBP / MoO_3 QDLEDs as well.

(a)

(b)
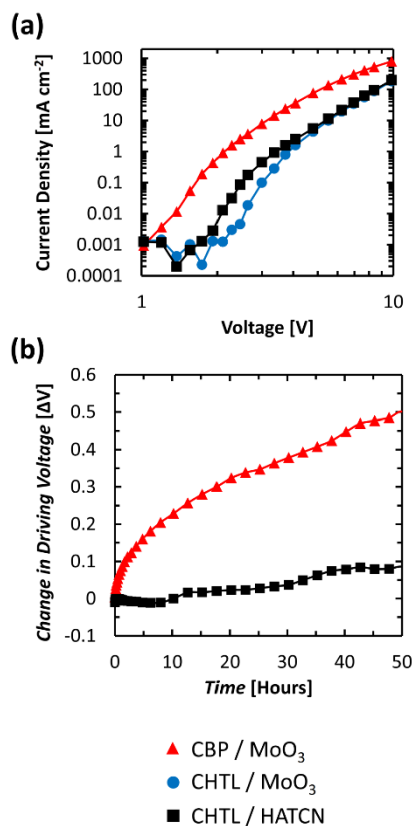
Figure 7.8 (a) Current density *vs.* voltage and (b) Change in driving voltage *vs.* time characteristics for the MoO_3 / QD / CBP / MoO_3 (triangle), MoO_3 / QD / CHTL / MoO_3 (circle), and MoO_3 / QD / CHTL / HATCN (square) hole-only devices under constant electrical driving at 20 mA cm^{-2} current density.

Knowing that the CHTL indeed reduces hole transport through the QDLED and that exciton-polaron interactions lead to degradation within those devices, investigating changes in the electron-hole recombination zone within the HTL becomes a critical aspect in the verification of the stability improvement mechanism imparted by the CHTL. In chapter 6, we identified that degradation of the HTL in the immediate vicinity of the QD layer by excitons can impact the latter's PLQY.[198] The NPB emission

in the CHTL / HATCN device EL spectra from **Figure 7.1** indicated that more excitons were present in the HTL further away from the QD / HTL interface than in the case of the CBP / MoO_3 device. However, these HTL emission bands were generally weak due to the low PLQY of CBP, TCTA, and NPB. Therefore, to probe the relative exciton density within the HTL, a 5 nm thick marking layer of CBP doped with 10% FIrpic, a blue organic phosphorescent emitter, was inserted 15 nm and 30 nm away from the QD / CBP interface as depicted in the schematic in **Figure 7.9**. FIrpic was chosen as the luminescent dopant for the marking layer because its EL occurs between 450 nm and 550 nm and is thus easy to distinguish from the EL of the QDs. In addition, its HOMO (-5.9 eV) and LUMO (-3.0 eV)[255] energy levels are close to those of CBP (-6.0 eV HOMO, -2.9 eV LUMO)[200] which may only minimally perturb charge distribution in the devices. The EL spectra of CHTL / HATCN and CBP / MoO_3 QDLEDs with the marking layers are depicted in **Figure 7.10**. By normalizing the EL intensity to the QD peak emission, the relative intensity of the marking layer emission at 500 nm can be compared as a fraction of the QD emission. The FIrpic emission in the CHTL / HATCN devices is an order of magnitude greater than that of the CBP / MoO_3 devices, confirming that the reduced hole transport through the CHTL results in a shift in electron-hole recombination within the HTL toward the anode. For the CHTL / HATCN device, the FIrpic emission is slightly greater for the $x = 30$ nm marking layer with an intensity of 1.38% of the normalized QD emission compared to 1.04% for $x = 15$ nm. In addition, there is an EL band in the $x = 15$ nm device between 350 nm and 450 nm corresponding to emission from the HTL, indicating the existence of a significant number of excitons within the CHTL closer to the anode that were not close enough to the marking layer for energy transfer to occur. Meanwhile, the CBP / MoO_3 marking layer devices exhibited relatively weak FIrpic emission amounting to only 0.26% for $x = 30$ nm and 0.46% for $x = 15$ nm. The relative heights of the bands suggest not only that are more excitons present in the CHTL of QDLEDs, but also that they are more spread out across the HTL, consistent with more distributed hole accumulation across the CHTL. Knowing that degradation of the HTL at the QD / HTL interface will lead to a reduction of the QD PLQY, reducing the hole accumulation in the immediate vicinity of the QD layer is likely the main factor behind the increased EL stability of the QDLEDs.
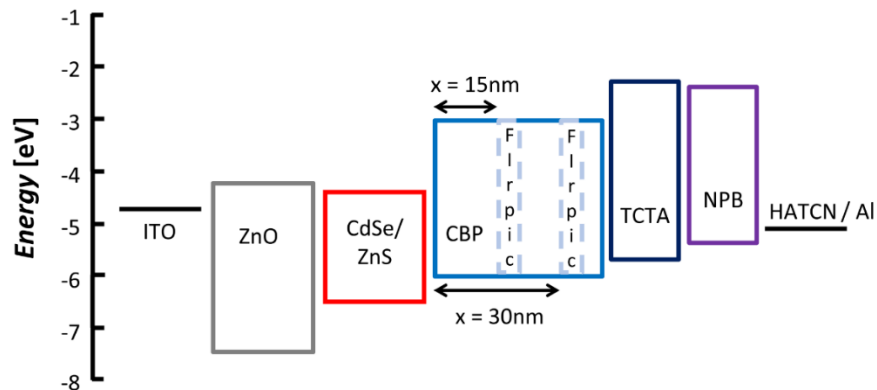
Figure 7.9 Energy level diagram schematic of the QDLEDs utilizing a 5 nm FIrpic marking layer, with distances of x = 15 nm and x = 30 nm away from the QD / HTL interface.
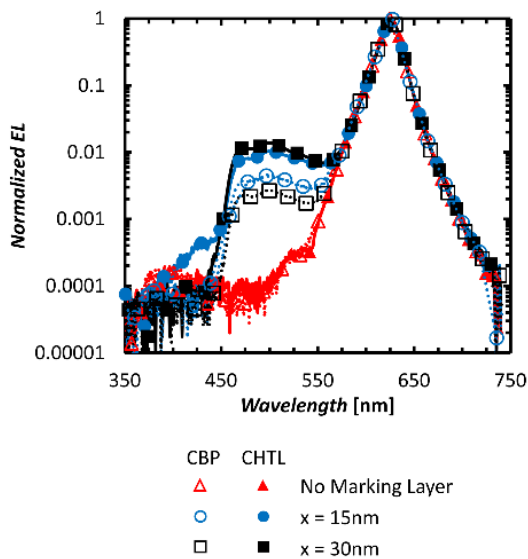
Figure 7.10 Normalized EL spectra of CHTL / HATCN (solid) and CBP / MoO$_3$ (dotted) QDLEDs with a 5 nm CBP:FIrpic [10%] marking layer inserted $x = 15$ nm (circle) and $x = 30$ nm (square) away from the QD / CBP interface and compared to the EL spectra of QDLEDs without a marking layer (triangle).

Seeing that introducing inter-layer hole accumulation interfaces away from the QD / HTL interface can improve QDLED stability, it becomes interesting to further investigate the effect of modulating the charge distribution within the CHTL by shifting the position of those interfaces. Therefore, we test the effect of changing the thickness of CBP, TCTA, and NPB layers while maintaining the same total HTL

thickness. Although we have observed limited emission from NPB in the CHTL / HATCN QDLED, the large LUMO energy level difference between CBP (-2.9 eV) and TCTA (-2.3 eV)[200] should confine most electrons that leak from the QD layer to the CBP layer. Therefore, three different CHTL-based QDLEDs were fabricated with a HATCN HIL and labeled with respect to their CBP layer thickness: CHTL-10 (CBP (10 nm) / TCTA (20 nm) / NPB (30 nm)), CHTL-20 (CBP (20 nm) / TCTA (20 nm) / NPB (20 nm)), and CHTL-40 (CBP (40 nm) / TCTA (10 nm) / NPB (10 nm)). The current density *vs.* voltage and EQE *vs.* current density characteristics of these QDLEDs are presented in **Figure 7.11** along with the CBP / MoO$_3$ QDLED investigated earlier. The CHTL charge transport increases and QDLED turn-on voltage decreases as the CBP thickness is reduced from 40 nm to 10 nm. In fact, the turn-on voltage of the CHTL-20 device is similar to that of the CBP / MoO$_3$ QDLED, and the turn-on voltage of the CHTL-10 device occurs at a lower driving voltage. The trend in CHTL turn-on voltage confirms the notion that moving the hole accumulation interfaces further away from the QD / HTL interface causes the turn-on voltage to increase. As the inter-layer HTL interface distance from the QD / CBP interface is reduced, the electric field required for hole injection becomes smaller which results in the lower turn-on voltage observed for the CHTL-10 and CHTL-20 devices compared to the CHTL-40 QDLEDs. Qiao *et al.* found that the hole mobility of the pristine HTLs follows the trend of TCTA > NPB > CBP and that the hole mobility of the materials can be improved by an order of magnitude with MoO$_3$-doping.[256] While the thermally doped CBP:MoO$_3$ appears to have the best hole transport, replacing a portion of the low mobility non-doped CBP layer with the higher mobility TCTA and NPB improves hole transport for the CHTL devices. Furthermore, increasing the hole transport through the HTL also appears to improve the efficiency of the QDLEDs from a maximum of 9.8% EQE for CHTL-40, to 10.6% for CHTL-20, and 11.1% for CHTL-10. In addition to the improvement in hole transport, the CHTL-20 and CHTL-10 stacks should confine excitons that are created in the CBP layer due to the leakage of electrons from the QD layer closer to the QD / CBP interface which may contribute to the enhanced efficiency *via* an increase in energy transfer from CBP to the QDs. Therefore, it is reasonable to conclude that the minor improvement in efficiency associated with the CHTL-40 QDLED over the CBP / MoO$_3$ device was achieved despite the worsening charge balance, and that improving charge

balance and confinement of excitons created in the CBP layer near the QD / CBP interface, such as in the CHTL-20 and CHTL-10 QDLEDs, may lead to further enhancements in efficiency.
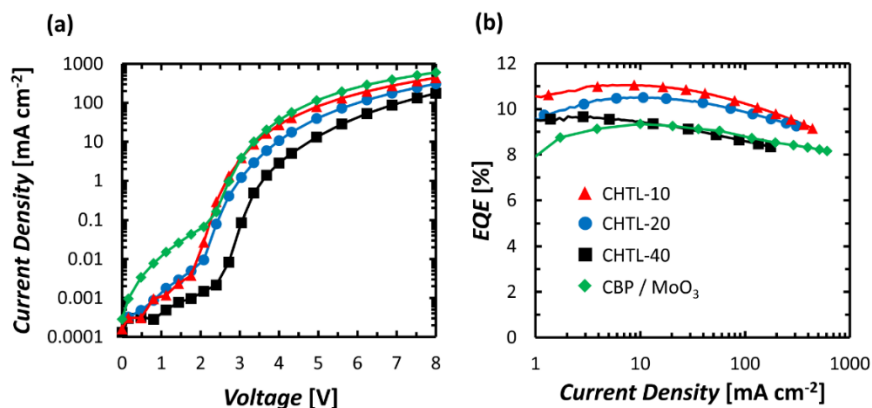
Figure 7.11 (a) Current density *vs*. voltage and (b) EQE *vs*. current density characteristics of the CHTL-10 (triangle), CHTL-20 (circle), CHTL-40 (square), and CBP / MoO₃ (diamond) QDLEDs.

Figure 7.12 depicts the normalized luminance and change in driving voltage *vs*. time trends of the three QDLEDs driven with 20 mA cm^{-2} constant current density. As can be seen from the figure, both EL and driving voltage stability of the devices are influenced by changing the thicknesses of the individual layers within the CHTL. This convincingly proves that the improvement is primarily due to changing the charge distribution within the HTL. It is therefore important to investigate the effect of changing the charge distribution within QDLEDs on their EL stability. Looking at the luminance decay rate of the three QDLEDs, one can identify two regimes: an initial fast degradation and a long-term slower degradation in luminance. In the initial fast degradation regime, the CHTL-10 device has the fastest rate of luminance decay followed by CHTL-20 and CHTL-40. Given that it is the device with the thinnest CBP layer that has the greatest degradation rate, the fast degradation may be driven by HTL degradation and Auger recombination at the QD / HTL interface due to the increased hole accumulation at this interface. Since the CHTL-40 device minimizes hole accumulation at the QD / HTL interface due to the accumulation of holes at the inter-layer HTL interfaces, it is least affected by this degradation mechanism. However, in the long-term degradation regime, the CHTL-40 device degrades fastest followed by CHTL-20 and CHTL-10. This

longer-term degradation mechanism may be driven by exciton-polaron interactions leading to degradation due to hole accumulation at the inter-layer HTL / HTL interfaces. Since hole transport is most impeded in the CHTL-40 device, it is expected that hole accumulation at the inter-layer HTL / HTL interfaces is more significant in this case. The shift in the degradation trends suggests a change in the dominant degradation mechanism between the three QDLED structures. The greater initial degradation of the CHTL-10 device results in the shortest LT50 of 530 hours (for a L_0 of 3,870 cd m^{-2}) compared to the 1,510 hour LT50 for the CHTL-20 QDLED (for a L_0 of 3,400 cd m^{-2}) and 825 hour LT50 for the CHTL-40 QDLED (for a L_0 of 3,445 cd m^{-2}). It is therefore possible that striking a balance between the two degradation mechanisms is behind the long EL half-life demonstrated by the CHTL-20 device. Ultimately, the CHTL-20 device has an LT50 equivalent to 864,000 hours (for a L_0 of 100 cd m^{-2}) after extrapolating the QDLED stability using the lifetime relation previously used, representing a 1.8× improvement over the CHTL-40 device and a 25× improvement over the CBP / MoO$_3$ device. Furthermore, CHTLs with better hole transport lead to a slower rise in voltage over time. In this regard, the CHTL with the thinnest CBP layer demonstrates the most stable voltage, giving further credence to the earlier conclusion that increasing the distance between the QD / HTL interface and interfaces where holes accumulate is behind the faster rate of driving voltage observed of the CHTL devices. The CHTL-10 device experiences an increase in driving voltage of only 0.7 V over 530 hours compared to the 8.6 V increase in driving voltage over 1510 hours for the CHTL-20 device and 7.8 V over 825 hours for the CHTL-40 device. Both the CHTL-20 and CHTL-40 devices experience a significant increase in driving voltage during the long-term degradation regime, but it takes much longer for the onset of this driving voltage increase to occur in the CHTL-20 QDLED. After 825 hours (corresponding to the LT50 of the CHTL-40 QDLED), the driving voltage of the CHTL-20 device has only increased by 3.0 V, while the driving voltage of the CHTL-40 device has increased by 7.8 V. Therefore, not only can the CHTL-20 architecture improve EL stability of QDLEDs, but it can also lead to enhancements in driving voltage stability as well.
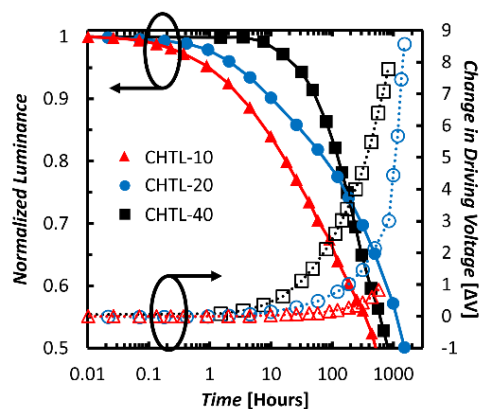
Figure 7.12 Normalized luminance *vs.* time (solid) and change in driving voltage *vs.* time (dotted) characteristics of the CHTL-10 (triangle), CHTL-20 (circle), and CHTL-40 (square) QDLEDs under constant electrical driving at 20 mA cm^{-2} current density.

In order to further verify that the CHTL shifts the accumulation of holes away from the QD / HTL interface, we also carry out delayed EL measurements on CBP / MoO$_3$ and CHTL-20 QDLEDs. The delayed EL of the QDLED with a bilayer HTL of TCTA / NPB and HATCN HIL discussed previously is also included in the comparison to investigate the effect of using a better electron blocking QD / HTL interface. The delayed EL measurements are performed using the experimental setup described in section 3.2.4. In the delayed EL technique, QDLEDs are driven with a 500 µs forward bias square pulse equivalent to the driving voltage required to achieve a driving current density of 20 mA cm^{-2} and allow prompt EL to reach steady state. An optical chopper system is activated to record the EL 50 µs following the end of the forward bias pulse. This delay is sufficiently long for all allowable luminescent exciton relaxation processes to occur and is much larger than a typical QDLED electrical time constant,[120,212] rendering electrical transient effects negligible. Therefore, any measured EL signal will arise from radiative decay of excitons that are formed after the termination of the forward bias pulse. **Figure 7.13**(a) depicts the delayed EL intensity signal versus time collected from the CBP / MoO$_3$, CHTL-20, and TCTA / NPB QDLEDs and the values obtained correspond to an amplified photovoltage corrected to the initial luminance of the measured device. The maximum delayed EL value for the CHTL-20 is 5× greater than the TCTA / NPB bilayer QDLED and 7.5× greater than the CBP / MoO$_3$ QDLED. These results suggest that more excitons in the CHTL-20 QDLED are able to recombine radiatively on the QD EML compared to the other two QDLED

135

structures, whereas excitons in the CBP / MoO$_3$ device are least capable of that. This trend correlates with the charge accumulation scheme proposed in **Figure 7.7** whereby the degree of hole accumulation at the QD / HTL interface in QDLEDs decreases in the following order: CBP / MoO$_3$ > TCTA / NPB > CHTL-20. In general, the formation of excitons in the microsecond time scale in these QDLEDs can be attributed to two processes: (i) recombination of residual (trapped / accumulated) charges in the various device layers including the HTL that become mobile and capable of recombination, producing luminescence after the end of the forward bias pulse and / or (ii) triplet excitons created within the HTL that diffuse slowly and eventually reach the QDs, inducing their late excitation via energy transfer either directly from those triplet states (by a Dexter process) or by a Förster process from singlet intermediates produced by TTA. Either way, a large portion of the delayed EL arises from excitons that originate in the HTL in the vicinity of the QD layer and subsequently diffuse to the QD EML, producing luminescence. As the presence of large space charges will quench these excitons, the higher delayed EL in the case of the CHTL QDLED directly points to reduced hole accumulation in the HTL in the vicinity of the QD / HTL interface.
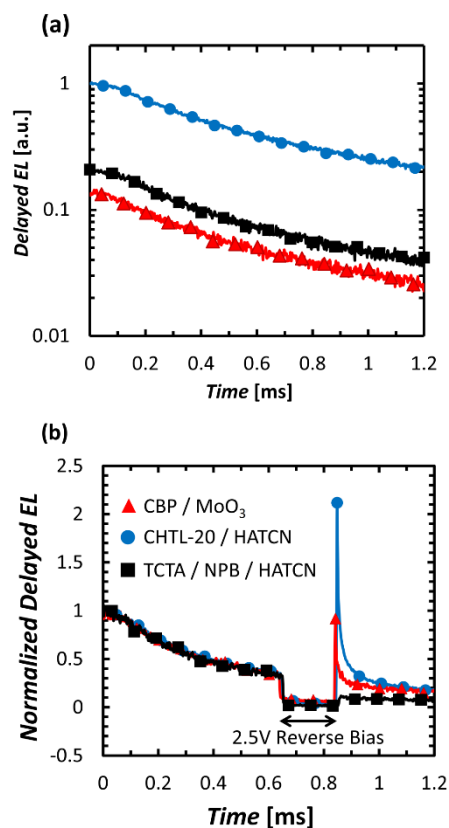
Figure 7.13 (a) Delayed EL of QDLEDs with HTLs consisting of CBP / MoO$_3$ (triangle), CHTL-20 / HATCN (circle), or TCTA / NPB / HATCN (square). (b) Normalized delayed EL of the same QDLEDs with a 2.5 V reverse bias applied from 650 µs to 850 µs.

We also investigate the effect of applying a 2.5 V reverse bias pulse, 200 µs long, applied 650 µs after the opening of the optical chopper on the delayed EL characteristics. It is known that in devices where process (i) is the dominant mechanism behind the delayed EL, the application of a reverse bias will lead to a permanent reduction in the delayed EL intensity and is sometimes accompanied by the appearance of a spike due to the redistribution of charges. Whereas, in devices where process (ii) is more dominant, the reverse bias will result in a temporary decrease in the delayed EL signal due to electric-field induced dissociation of excitons which recovers after the reverse bias has ended. **Figure 7.13**(b) shows the effect of the reverse bias on the delayed EL characteristics from the same set of devices. The data is normalized to the peak delayed EL value at $t = 0$ s in order to facilitate a comparison between the relative spike intensities. In all three QDLEDs, the application of a reverse bias leads to some permanent decrease in the delayed EL signal accompanied by a spike for the devices with CBP in their HTL. The delayed EL spike is 2.1× greater

than the initial delayed EL maximum value in the CHTL-20 QDLED whereas the spike for the CBP / MoO_3 QDLED is only 0.9× its initial delayed EL maximum value. This spike in delayed EL signal is a result of the cross-over of charge carriers that have been injected past the EML into the opposite charge transport layer and are now pushed back toward the EML. The recombination of leakage electrons in the CBP layer with the holes that accumulate at the QD / HTL interface is likely the source of this delayed EL spike. This mechanism is illustrated in **Figure 7.14** with a schematic depicting the direction of accumulated and trapped charge flow in the three QDLEDs of interest under the reverse bias. That leakage of electrons into the CBP layer is behind these spikes is evident from the absence of a spike when a more electron-blocking interface is used (*i.e.* the TCTA / NPB bilayer QDLED). This is corroborated via the current density *vs.* voltage curves in **Figure 7.11** where the CBP / MoO_3 devices exhibit much greater leakage currents compared to the CHTL QDLEDs as the electrons in the CBP layer may easily reach the anode, too far away from the QD EML for excitons to produce delayed EL. The large permanent non-reversible component of the TCTA / NPB QDLED can also be attributed to the lack of charge carrier cross-over during the reverse bias pulse, which would have otherwise given the charges additional recombination opportunities. The delayed EL results convincingly show that there are indeed differences in charge distribution across the HTL among these devices and that the CHTL has the least accumulation of charges in the vicinity of the QD / HTL interface.
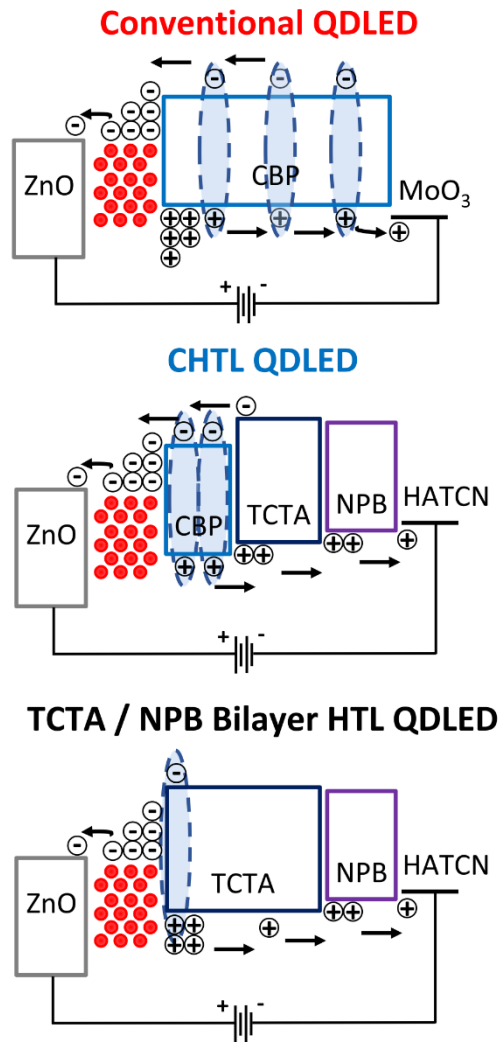
Figure 7.14 Schematic of CBP / MoO₃, CHTL / HATCN, and TCTA / NPB / HATCN QDLEDs under reverse bias, where arrows indicate the direction of flow for accumulated / trapped charges. The dashed areas indicate likely exciton formation spots which may lead to delayed EL.

7.4   Conclusions

We have studied the effect of the hole transport layer on the degradation of QDLEDs, finding that the stability can be improved by 25× by incorporating a multi-layer HTL stack with cascading HOMO energy levels compared to a conventional CBP / MoO_3 device. Using this approach, we have obtained a LT50 of 864,000 hours (for a L_0 of 100 cd m^{-2}) for red QDLEDs using a conventional core / shell QD emitter. The improvement in QDLED performance that arises from the CHTL structure is multi-faceted. First, the gradual reduction in HOMO energy level allows for the use of alternate HILs such as HATCN which do not damage the underlying organic layers during device fabrication. Second, the CHTL restricts the accumulation of holes at the QD / HTL interface and charging of the QD layer by introducing several inter-layer interfaces to inhibit excessive hole injection. This reduction in charge accumulation at the QD / HTL interface may inhibit the exciton-induced degradation of the HTL near this interface which has been shown to reduce the QD PLQY over time. Finally, the CHTL shifts the recombination zone of excitons within the HTL away from the QD emissive layer to limit quenching by degradation of the HTL. The CHTL QDLEDs also demonstrate an EQE enhancement of 18% from 9.4% to 11.1% over the conventional CBP / MoO_3 device. These findings shed light on the importance the hole transport layer on the stability of QDLEDs, providing a framework for controlling the factors that lead to degradation arising from the energy level mismatch at the QD / HTL interface which leads to an excessive accumulation of holes.

Chapter 8: Summary and Future Work

8.1   Summary

The research described in this thesis has elucidated the influence that the interfaces between each layer in the QDLED has in the performance of these devices, generally with a focus on their stability. While the ETL / EML interface plays a role in the overall performance of QDLEDs, the findings indicate that the HTL interfaces (both EML / HTL and HTL / HIL) have a much more significant impact over the efficiency and stability of these QDLEDs. The deep conduction and valence band energies of the CdSe-based QDs used in this work lead to an inherent charge imbalance within these devices as electrons are much easier to inject into the EML than holes. The use of organic semiconductors as the HTL is another reason for the greater significance of these interfaces as their initial amorphous morphology can induce crystallization over time due to thermal and electrical stresses in addition to the well-documented exciton-induced degradation of these materials in OLEDs. However, by investigating the effect that these degradation mechanisms have in the stability of QDLEDs and leveraging the multitude of organic semiconductors that exist for hole transport, an optimized HTL structure of organic materials with cascading HOMO energy levels has been demonstrated to improve the EL stability of QDLEDs by $25\times$ with an LT50 of up to 864,000 hours and also slightly improving the EQE to 11.1%. Although red CdSe-based QDs have been the emitter of focus in this work, these findings are expected to be applicable to other colours as well due to the inherent charge imbalance within these devices as the barrier to hole injection increases. While the barrier to electron injection also increases, there are many more tools available to improve electron injection into QDs such as the introduction of interfacial work function modification layers like PEI.

The main findings of this work are as follows:

In chapter 4, the role of the ETL / EML interface in QDLED performance was investigated by introducing the wide band gap work function modification layer PEI. While a $1.6\times$ improvement in maximum EQE was observed (from 4.5% to 7.2%), this coincided with an increase in electron injection from ZnO to the QD layer. Rather than a result of improved charge balance, this efficiency enhancement was attributed to a reduction in QD exciton quenching by the ZnO due to the passivation of surface states at this interface. An investigation into the increased electron injection effects by the introduction of a FIrpic marking layer at the EML / HTL interface showed that a greater concentration of excitons was present in the HTL. While this resulted in a negligible effect on the EL stability of these QDLEDs at the time, further experiments investigating the effect of excitons at the EML / HTL interface would identify these excitons as an issue for long-term QDLED stability. Ultimately, the main influence of the ETL / EML interface on QDLED performance lies in the exciton quenching effect of ZnO surface states which limits the QD film PLQY.

In chapter 5, the influence of the ETL and EML layers on morphological stability was investigated by a systematic study on the processing parameters of ZnO and the QDs for spherical and rod-shape QDs. While conducting EL stability measurements, an observation was made that dark spots and inhomogeneities in the QDLED emissive area would occur regardless of whether they had been aged under constant electrical current or merely left in a N_2 environment for the same duration of time. The morphological stability of the QDLEDs was evaluated by comparing the emissive area before and after storage in N_2 for a period of time as a function of varying the ZnO layer thickness and annealing time for different QD compositions and thicknesses. The main factor determining the degree of morphological degradation in emissive area homogeneity is the roughness of each layer. This is also a limitation in OLED morphological stability, as the organic semiconductors are prone to crystallization when deposited on rough surfaces. Therefore, even if the roughness increases at the ETL / EML interface, the propagation of this roughness through the QD layer can lead to a morphological degradation of the organic semiconductor. Therefore,

although rough layers are the catalyst of this morphological instability, it is the organic HTL that is the limiting factor in long-term morphological stability. Less roughness also generally correlated to better QDLED efficiency, and spherical CdSe / ZnS QDs also led to improved efficiency in comparison to rod-shape CdSe / CdS QDs.

In chapter 6, the role of degradation of the HTL on overall QDLED stability was further investigated through PL measurements from QDLEDs over time while irradiated with UV light. While QDLEDs with similar charge transport and efficiency can be fabricated with different HTLs having similar molecular structure (CBP and Spiro-CBP), these devices exhibit and order of magnitude difference in their LT50. From the work detailed in chapter 4, it is known that excitons are present in the HTL and exciton-induced degradation is a mechanism that has been explored extensively in OLED literature. Therefore, given that the major difference between the aforementioned QDLED structures is the organic HTL, the inherent stability of the HTLs was investigated. By measuring changes in the QD PL over time under constant UV illumination in devices with a variety of organic semiconductors, it became clear that the HTL has a significant influence over the loss in QD PLQY during aging. Further investigations of the exciton-induced degradation of each component layer in the devices found that while the QDs are relatively stable during the measurement period, the PLQY loss in the QDLEDs could be related to the individual PLQY loss of the organic layers. Since these measurements were carried out via photo-excitation only, it is expected that the observed degradation is related to excitons only and not via interactions with polarons which have been shown to degrade both QDs and organic materials in literature. Rather, it appears that exciton-induced degradation mainly affects the organic layers and it is the degradation of these organic molecules that lead to a loss in QD PLQY via quenching. It is therefore the exciton-induced degradation of the organic molecules at the QD / HTL interface that is particularly deleterious to QDLED stability.

In chapter 7, a three-layer HTL structure with cascading HOMO energy levels was investigated as a means to reduce hole accumulation at the QD / HTL interface. Although efficiency only increased marginally with the CHTL structure, these devices exhibited a significant improvement in EL stability.

143

With the optimized CHTL structure, a 25× enhancement in LT50 was observed with a lifetime of 864,000 hours. The improvement in QDLED performance that arises from the CHTL structure is multi-faceted. First, the gradual reduction in HOMO energy level allows for the use of alternate HILs such as HATCN which would not normally be able to inject holes into CBP and do not damage the underlying organic layers during device fabrication. Second, the CHTL restricts the accumulation of holes at the QD / HTL interface and charging of the QD layer by introducing several inter-layer HTL / HTL interfaces to inhibit excessive hole injection. This reduction in charge accumulation at the QD / HTL interface may inhibit the exciton-induced degradation of the HTL near this interface which has been shown to reduce the QD PLQY over time. Finally, the CHTL shifts the recombination zone of excitons within the HTL away from the QD EML to limit quenching by degradation of the HTL at the QD / HTL interface.

Therefore, in this work not only has a degradation mechanism affecting long-term EL stability of QDLEDs been identified and characterized, but a device structure which utilizes a cascading HTL with small gaps between each component's HOMO energy level and an organic HIL has been demonstrated that minimizes the effects of this mechanism on QDLED EL stability. These results were achieved with commercially available CdSe / ZnS QDs, allowing for further stability improvements with optimized QD compositions.

8.2   Future Work

While this work focuses on understanding the role of the interfaces in red QDLED performance, these findings should be applicable to QDs with other colours and compositions as well.

After finding that we can utilize a CHTL structure to significantly improve the lifetime of red QDLEDs, the natural extension of this work is to see if this technique can be used to improve the lifetime of green and blue QDLEDs as well. As detailed in chapter 3, red and green QDLED lifetimes have reached levels suitable for many applications yet blue QDLED lifetimes are still quite poor. Furthermore, while exciton recycling techniques that are used to transfer excitons from the HTL to the QD EML via luminescent sensitizers (i.e. FIrpic) can be useful in red and green QDLEDs, the necessary donor-acceptor specral overlap does not exist for blue QDLEDs. Therefore, we expect that HTL charge accumulation and exciton management may be even more important in blue QDLEDs.

Another benefit of the CHTL structure is the confinement of leakage electrons in a thinner CBP layer to reduce QDLED leakage current as fewer electrons reach the anode. This property of the CHTL could prove useful in the aforementioned exciton recycling via luminescent sensitizers as the CHTL may be used to confine the HTL excitons closer to the QD / HTL interface which, for these devices, is required for efficient energy transfer back to the QD EML.

As demonstrated in this work, the degradation of the organic layers can play a significant role in the EL stability of QDLEDs. If, indeed, this is a limiting factor in long-lifetime QDLEDs then it may be valuable to explore all-inorganic transport layer QDLEDs similar to the devices discussed in section 2.2. Although those devices were unable to achieve good performance comparable to the hybrid transport layer structures, recent work in this field has demonstrated QDLEDs with EQEs of up to 5.51% for red and 11.4% for green.[177,257] The best all-inorganic QDLED LT50 to date is 16,120 hours for green, orders of magnitude less than the record hybrid transport layer structure.[177] Efficiency, and especially stability, of these QDLEDs

is a seldom studied area so an understanding of the reason for these devices relatively poor efficiency and their degradation mechanisms could lead to a breakthrough in the field.

In order to meet the RoHS safety requirements for commercial applications of QDLEDs which limits the amount of Cd allowed in products, Cd-free QDs have become a recent avenue of interest in QDLED research. As mentioned in chapter 2, InP has become the leading alternative to CdSe-based QDs and have demonstrated > 95% PLQY and 16.9% EQE for red QDLEDs in literature.[47] However, the lifetime has not been reported for these state-of-the-art Cd-free QDLEDs which suggests that their stability may still be extremely poor. These QDs are expected to have shallower energy levels (-3.8 eV conduction band, -5.9 eV valence band energies for red QDs)[48] than CdSe-based QDs, so hole accumulation may not be as much of an issue for these devices. While the CHTL may not be the solution to the stability of Cd-free QDLEDs, the degradation mechanisms affecting these devices are currently unexplored and an understanding of these effects will be valuable to both the scientific and commercial communities.

References

(1)   Bera, D.; Qian, L.; Tseng, T.-K.; Holloway, P. H. Quantum Dots and Their Multimodal Applications: A Review. *Materials (Basel).* **2010**, *3* (4), 2260–2345. https://doi.org/10.3390/ma3042260.

(2)   Shirasaki, Y.; Supran, G. J.; Bawendi, M. G.; Bulović, V. Emergence of Colloidal Quantum-Dot Light-Emitting Technologies. *Nat. Photonics* **2013**, *7* (1), 13–23. https://doi.org/10.1038/nphoton.2012.328.

(3)   Dai, X.; Deng, Y.; Peng, X.; Jin, Y. Quantum-Dot Light-Emitting Diodes for Large-Area Displays: Towards the Dawn of Commercialization. *Adv. Mater.* **2017**, *29* (14), 1607022. https://doi.org/10.1002/adma.201607022.

(4)   Yang, Z.; Gao, M.; Wu, W.; Yang, X.; Sun, X. W.; Zhang, J.; Wang, H.-C.; Liu, R.-S.; Han, C.-Y.; Yang, H.; et al. Recent Advances in Quantum Dot-Based Light-Emitting Devices: Challenges and Possible Solutions. *Mater. Today* **2019**, *24*, 69–93. https://doi.org/10.1016/j.mattod.2018.09.002.

(5)   Pietryga, J. M.; Park, Y.-S.; Lim, J.; Fidler, A. F.; Bae, W. K.; Brovelli, S.; Klimov, V. I. Spectroscopic and Device Aspects of Nanocrystal Quantum Dots. *Chem. Rev.* **2016**, *116* (18), 10513–10622. https://doi.org/10.1021/acs.chemrev.6b00169.

(6)   Owen, J.; Brus, L. Chemical Synthesis and Luminescence Applications of Colloidal Semiconductor Quantum Dots. *J. Am. Chem. Soc.* **2017**, *139* (32), 10939–10943. https://doi.org/10.1021/jacs.7b05267.

(7)   Jiang, Y.; Cho, S.-Y.; Shim, M. Light-Emitting Diodes of Colloidal Quantum Dots and Nanorod Heterostructures for Future Emissive Displays. *J. Mater. Chem. C* **2018**, *6* (11), 2618–2634. https://doi.org/10.1039/C7TC05972H.

(8)   Moon, H.; Lee, C.; Lee, W.; Kim, J.; Chae, H. Stability of Quantum Dots, Quantum Dot Films, and Quantum Dot Light-Emitting Diodes for Display Applications. *Adv. Mater.* **2019**, *31* (34), 1804294. https://doi.org/10.1002/adma.201804294.

(9)   Chen, H.-W.; Lee, J.-H.; Lin, B.-Y.; Chen, S.; Wu, S.-T. Liquid Crystal Display and Organic Light-Emitting Diode Display: Present Status and Future Perspectives. *Light Sci. Appl.* **2018**, *7* (3), 17168–17168. https://doi.org/10.1038/lsa.2017.168.

(10)   Reineke, S. Complementary LED Technologies. *Nat. Mater.* **2015**, *14* (5), 459–462. https://doi.org/10.1038/nmat4277.

(11)   Shin, H.; Park, K.; Takasugi, S.; Choi, S.-H.; Jeong, Y.; Choi, H.; Kim, I.-J.; Kim, H.; Lee, H.; Oh, C. 45-2: Advanced OLED Display Technologies for Large-Size Semi-Flexible TVs. *SID Symp. Dig. Tech. Pap.* **2016**, *47* (1), 609–612. https://doi.org/10.1002/sdtp.10759.

(12)   Burrows, P. E.; Bulovic, V.; Forrest, S. R.; Sapochak, L. S.; McCarty, D. M.; Thompson, M. E. Reliability

and Degradation of Organic Light Emitting Devices. *Appl. Phys. Lett.* **1994**, *65* (23), 2922–2924. https://doi.org/10.1063/1.112532.

(13)   Aziz, H.; Popovic, Z. D. Degradation Phenomena in Small-Molecule Organic Light-Emitting Devices. *Chem. Mater.* **2004**, *16* (23), 4522–4532. https://doi.org/10.1021/cm040081o.

(14)   Kondakov, D. Y. Device Degradation. In *OLED Fundamentals: Materials, Devices, and Processing of Organic Light-Emitting Diodes*; Gaspar, D. J., Polikarpov, E., Eds.; CRC Press, 2015; pp 339–364.

(15)   Kondakov, D. Y.; Lenhart, W. C.; Nichols, W. F. Operational Degradation of Organic Light-Emitting Diodes: Mechanism and Identification of Chemical Products. *J. Appl. Phys.* **2007**, *101* (2), 024512. https://doi.org/10.1063/1.2430922.

(16)   Giebink, N. C.; D'Andrade, B. W.; Weaver, M. S.; Brown, J. J.; Forrest, S. R. Direct Evidence for Degradation of Polaron Excited States in Organic Light Emitting Diodes. *J. Appl. Phys.* **2009**, *105* (12), 124514. https://doi.org/10.1063/1.3151689.

(17)   Wang, Q.; Aziz, H. Degradation of Organic/Organic Interfaces in Organic Light-Emitting Devices Due to Polaron–Exciton Interactions. *ACS Appl. Mater. Interfaces* **2013**, *5* (17), 8733–8739. https://doi.org/10.1021/am402537j.

(18)   Wang, Q.; Aziz, H. Exciton-Polaron-Induced Aggregation of Organic Electroluminescent Materials: A Major Degradation Mechanism in Wide-Bandgap Phosphorescent and Fluorescent Organic Light-Emitting Devices. *Adv. Opt. Mater.* **2015**, *3* (7), 967–975. https://doi.org/10.1002/adom.201400640.

(19)   Wang, Q.; Sun, B.; Aziz, H. Exciton-Polaron-Induced Aggregation of Wide-Bandgap Materials and Its Implication on the Electroluminescence Stability of Phosphorescent Organic Light-Emitting Devices. *Adv. Funct. Mater.* **2014**, *24* (20), 2975–2985. https://doi.org/10.1002/adfm.201303840.

(20)   Lee, J.-H.; Chen, C.-H.; Lee, P.-H.; Lin, H.-Y.; Leung, M.; Chiu, T.-L.; Lin, C.-F. Blue Organic Light-Emitting Diodes: Current Status, Challenges, and Future Outlook. *J. Mater. Chem. C* **2019**, *7* (20), 5874–5888. https://doi.org/10.1039/C9TC00204A.

(21)   Hanson, G. W. Models of Semiconductor Quantum Wells, Quantum Wires, and Quantum Dots. In *Fundamentals of Nanoelectronics*; Pearson/Prentice Hall, 2008; pp 280–314.

(22)   Yang, Y.; Zheng, Y.; Cao, W.; Titov, A.; Hyvonen, J.; Manders, J. R.; Xue, J.; Holloway, P. H.; Qian, L. High-Efficiency Light-Emitting Devices Based on Quantum Dots with Tailored Nanostructures. *Nat. Photonics* **2015**, *9* (4), 259–266. https://doi.org/10.1038/nphoton.2015.36.

(23)   Kwak, J.; Bae, W. K.; Lee, D.; Park, I.; Lim, J.; Park, M.; Cho, H.; Woo, H.; Yoon, D. Y.; Char, K.; et al. Bright and Efficient Full-Color Colloidal Quantum Dot Light-Emitting Diodes Using an Inverted Device Structure. *Nano Lett.* **2012**, *12* (5), 2362–2366. https://doi.org/10.1021/nl3003254.

(24)   Peng, H.; Jiang, Y.; Chen, S. Efficient Vacuum-Free-Processed Quantum Dot Light-Emitting Diodes with Printable Liquid Metal Cathodes. *Nanoscale* **2016**, *8* (41), 17765–17773. https://doi.org/10.1039/C6NR05181B.

(25)   Jin, X.; Chang, C.; Zhao, W.; Huang, S.; Gu, X.; Zhang, Q.; Li, F.; Zhang, Y.; Li, Q. Balancing the Electron and Hole Transfer for Efficient Quantum Dot Light-Emitting Diodes by Employing a Versatile Organic Electron-Blocking Layer. *ACS Appl. Mater. Interfaces* **2018**, *10* (18), 15803–15811. https://doi.org/10.1021/acsami.8b00729.

(26)   Khan, Q.; Subramanian, A.; Ahmed, I.; Khan, M.; Nathan, A.; Wang, G.; Wei, L.; Chen, J.; Zhang, Y.; Bao, Q. Overcoming the Electroluminescence Efficiency Limitations in Quantum-Dot Light-Emitting Diodes. *Adv. Opt. Mater.* **2019**, *7* (20), 1900695. https://doi.org/10.1002/adom.201900695.

(27)   Song, J.; Wang, O.; Shen, H.; Lin, Q.; Li, Z.; Wang, L.; Zhang, X.; Li, L. S. Over 30% External Quantum Efficiency Light-Emitting Diodes by Engineering Quantum Dot-Assisted Energy Level Match for Hole Transport Layer. *Adv. Funct. Mater.* **2019**, *29* (33), 1808377. https://doi.org/10.1002/adfm.201808377.

(28)   Shen, H.; Gao, Q.; Zhang, Y.; Lin, Y.; Lin, Q.; Li, Z.; Chen, L.; Zeng, Z.; Li, X.; Jia, Y.; et al. Visible Quantum Dot Light-Emitting Diodes with Simultaneous High Brightness and Efficiency. *Nat. Photonics* **2019**, *13* (3), 192–197. https://doi.org/10.1038/s41566-019-0364-z.

(29)   Davidson-Hall, T.; Aziz, H. Perspective: Toward Highly Stable Electroluminescent Quantum Dot Light-Emitting Devices in the Visible Range. *Appl. Phys. Lett.* **2020**, *116* (1), 010502. https://doi.org/10.1063/1.5134090.

(30)   Chuang, S. L. Optical Processes in Semiconductors. In *Physics of Photonic Devices*; John Wiley & Sons Ltd, 2009; pp 347–410. https://doi.org/10.1149/1.2404256.

(31)   Xu, X.; Weaver, M. S. Small Molecule Fundamentals. In *OLED Fundamentals: Materials, Devices, and Processing of Organic Light-Emitting Diodes*; Gaspar, D. J., Polikarpov, E., Eds.; CRC Press, 2015; pp 127–146.

(32)   Barltrop, J. A.; Coyle, J. D. Excited States. Production and Time-Independent Properties. In *Principles of Photochemistry*; John Wiley & Sons Ltd, 1982; pp 11–63.

(33)   Barltrop, J. A.; Coyle, J. D. Excited States: Time-Dependent Phenomena. In *Principles of Photochemistry*; John Wiley & Sons Ltd, 1982; pp 64–100.

(34)   Hanson, G. W. Free and Confined Electrons. In *Fundamentals of Nanoelectronics*; Pearson/Prentice Hall, 2008; pp 87–133.

(35)   Brus, L. Electronic Wave Functions in Semiconductor Clusters: Experiment and Theory. *J. Phys. Chem.* **1986**, *90* (12), 2555–2560. https://doi.org/10.1021/j100403a003.

(36)   Hanson, G. W. Particle Statistics and Density of States. In *Fundamentals of Nanoelectronics*; Pearson/Prentice Hall, 2008; pp 265–285.

(37)   Efros, A. L.; Efros, A. L. Interband Light Absorption in Semiconductor Spheres. *Sov. Phys. Semicond.* **1982**, *16* (7), 772–775.

(38)   Brus, L. E. Electron–Electron and Electron-hole Interactions in Small Semiconductor Crystallites: The Size Dependence of the Lowest Excited Electronic State. *J. Chem. Phys.* **1984**, *80* (9), 4403–4409. https://doi.org/10.1063/1.447218.

(39)   Norris, D. J. Electronic Structure in Semiconductor Nanocrystals: Optical Experiment. In *Nanocrystal Quantum Dots*; Klimov, V. I., Ed.; CRC Press, 2010; pp 63–96.

(40)   Norris, D. J.; Bawendi, M. G. Measurement and Assignment of the Size-Dependent Optical Spectrum in CdSe Quantum Dots. *Phys. Rev. B* **1996**, *53* (24), 16338–16346. https://doi.org/10.1103/PhysRevB.53.16338.

(41)   Norris, D. J.; Efros, A. L.; Rosen, M.; Bawendi, M. G. Size Dependence of Exciton Fine Structure in CdSe Quantum Dots. *Phys. Rev. B* **1996**, *53* (24), 16347–16354. https://doi.org/10.1103/PhysRevB.53.16347.

(42)   Sercel, P. C.; Efros, A. L. Band-Edge Exciton in CdSe and Other II–VI and III–V Compound Semiconductor Nanocrystals − Revisited. *Nano Lett.* **2018**, *18* (7), 4061–4068. https://doi.org/10.1021/acs.nanolett.8b01980.

(43)   Peng, X.; Wickham, J.; Alivisatos, A. P. Kinetics of II-VI and III-V Colloidal Semiconductor Nanocrystal Growth: "Focusing" of Size Distributions. *J. Am. Chem. Soc.* **1998**, *120* (21), 5343–5344. https://doi.org/10.1021/ja9805425.

(44)   Riehle, F. S.; Bienert, R.; Thomann, R.; Urban, G. A.; Krüger, M. Blue Luminescence and Superstructures from Magic Size Clusters of CdSe. *Nano Lett.* **2009**, *9* (2), 514–518. https://doi.org/10.1021/nl080150o.

(45)   Čapek, R. K.; Lambert, K.; Dorfs, D.; Smet, P. F.; Poelman, D.; Eychmüller, A.; Hens, Z. Synthesis of Extremely Small CdSe and Bright Blue Luminescent CdSe/ZnS Nanoparticles by a Prefocused Hot-Injection Approach. *Chem. Mater.* **2009**, *21* (8), 1743–1749. https://doi.org/10.1021/cm900248b.

(46)   Jang, E.; Jang, H.; Kang, H. A.; Cho, O. 67-1: Invited Paper : Environmentally Friendly Quantum Dots for Display Applications. *SID Symp. Dig. Tech. Pap.* **2017**, *48* (1), 980–983. https://doi.org/10.1002/sdtp.11824.

(47)   Ippen, C.; Guo, W.; Zehnder, D.; Kim, D.; Manders, J.; Barrera, D.; Newmeyer, B.; Hamilton, D.; Wang, C.; Hotz, C.; et al. High Efficiency Heavy Metal Free QD-LEDs for next Generation Displays. *J. Soc. Inf. Disp.* **2019**, *27* (6), 338–346. https://doi.org/10.1002/jsid.780.

(48)   Hahm, D.; Chang, J. H.; Jeong, B. G.; Park, P.; Kim, J.; Lee, S.; Choi, J.; Kim, W. D.; Rhee, S.; Lim, J.; et al. Design Principle for Bright, Robust, and Color-Pure InP/ZnSe x S 1– x /ZnS Heterostructures. *Chem. Mater.* **2019**, *31* (9), 3476–3484. https://doi.org/10.1021/acs.chemmater.9b00740.

(49)   Kim, Y.; Ham, S.; Jang, H.; Min, J. H.; Chung, H.; Lee, J.; Kim, D.; Jang, E. Bright and Uniform Green Light Emitting InP/ZnSe/ZnS Quantum Dots for Wide Color Gamut Displays. *ACS Appl. Nano Mater.* **2019**, *2* (3), 1496–1504. https://doi.org/10.1021/acsanm.8b02063.

(50)   Wang, A.; Shen, H.; Zang, S.; Lin, Q.; Wang, H.; Qian, L.; Niu, J.; Song Li, L. Bright, Efficient, and Color-Stable Violet ZnSe-Based Quantum Dot Light-Emitting Diodes. *Nanoscale* **2015**, *7* (7), 2951–2959. https://doi.org/10.1039/C4NR06593J.

(51)   Shi, Y.-L.; Liang, F.; Hu, Y.; Zhuo, M.-P.; Wang, X.-D.; Liao, L.-S. High Performance Blue Quantum Dot Light-Emitting Diodes Employing Polyethylenimine Ethoxylated as the Interfacial Modifier. *Nanoscale* **2017**, *9* (39), 14792–14797. https://doi.org/10.1039/C7NR04542E.

(52)   Wang, O.; Wang, L.; Li, Z.; Xu, Q.; Lin, Q.; Wang, H.; Du, Z.; Shen, H.; Li, L. S. High-Efficiency, Deep Blue ZnCdS/Cd x Zn 1−x S/ZnS Quantum-Dot-Light-Emitting Devices with an EQE Exceeding 18%. *Nanoscale* **2018**, *10* (12), 5650–5657. https://doi.org/10.1039/C7NR09175C.

(53)   Zhong, Z.; Zou, J.; Jiang, C.; Lan, L.; Song, C.; He, Z.; Mu, L.; Wang, L.; Wang, J.; Peng, J.; et al. Improved Color Purity and Efficiency of Blue Quantum Dot Light-Emitting Diodes. *Org. Electron.* **2018**, *58* (April), 245–249. https://doi.org/10.1016/j.orgel.2018.04.014.

(54)   Li, D.; Bai, J.; Zhang, T.; Chang, C.; Jin, X.; Huang, Z.; Xu, B.; Li, Q. Blue Quantum Dot Light-Emitting Diodes with High Luminance by Improving the Charge Transfer Balance. *Chem. Commun.* **2019**, *55* (24), 3501–3504. https://doi.org/10.1039/C9CC00230H.

(55)   Wang, F.; Sun, W.; Liu, P.; Wang, Z.; Zhang, J.; Wei, J.; Li, Y.; Hayat, T.; Alsaedi, A.; Tan, Z. Achieving Balanced Charge Injection of Blue Quantum Dot Light-Emitting Diodes through Transport Layer Doping Strategies. *J. Phys. Chem. Lett.* **2019**, *10* (5), 960–965. https://doi.org/10.1021/acs.jpclett.9b00189.

(56)   Dabbousi, B. O.; Rodriguez-Viejo, J.; Mikulec, F. V.; Heine, J. R.; Mattoussi, H.; Ober, R.; Jensen, K. F.; Bawendi, M. G. (CdSe)ZnS Core−Shell Quantum Dots: Synthesis and Characterization of a Size Series of Highly Luminescent Nanocrystallites. *J. Phys. Chem. B* **1997**, *101* (46), 9463–9475. https://doi.org/10.1021/jp971091y.

(57)   Danek, M.; Jensen, K. F.; Murray, C. B.; Bawendi, M. G. Synthesis of Luminescent Thin-Film CdSe/ZnSe Quantum Dot Composites Using CdSe Quantum Dots Passivated with an Overlayer of ZnSe. *Chem. Mater.* **1996**, *8* (1), 173–180. https://doi.org/10.1021/cm9503137.

(58)   Hoener, C. F.; Allan, K. A.; Bard, A. J.; Campion, A.; Fox, M. A.; Mallouk, T. E.; Webber, S. E.; White, J. M. Demonstration of a Shell-Core Structure in Layered Cadmium Selenide-Zinc Selenide Small Particles by x-Ray Photoelectron and Auger Spectroscopies. *J. Phys. Chem.* **1992**, *96* (9), 3812–3817. https://doi.org/10.1021/j100188a045.

(59)   Hines, M. A.; Guyot-Sionnest, P. Synthesis and Characterization of Strongly Luminescing ZnS-Capped CdSe

Nanocrystals. *J. Phys. Chem.* **1996**, *100* (2), 468–471. https://doi.org/10.1021/jp9530562.

(60)   Tian, Y.; Newton, T.; Kotov, N. A.; Guldi, D. M.; Fendler, J. H. Coupled Composite CdS−CdSe and Core−Shell Types of (CdS)CdSe and (CdSe)CdS Nanoparticles. *J. Phys. Chem.* **1996**, *100* (21), 8927–8939. https://doi.org/10.1021/jp951965l.

(61)   Kortan, A. R.; Hull, R.; Opila, R. L.; Bawendi, M. G.; Steigerwald, M. L.; Carroll, P. J.; Brus, L. E. Nucleation and Growth of CdSe on ZnS Quantum Crystallite Seeds, and Vice Versa, in Inverse Micelle Media. *J. Am. Chem. Soc.* **1990**, *112* (4), 1327–1332. https://doi.org/10.1021/ja00160a005.

(62)   Peng, X.; Schlamp, M. C.; Kadavanich, A. V.; Alivisatos, A. P. Epitaxial Growth of Highly Luminescent CdSe/CdS Core/Shell Nanocrystals with Photostability and Electronic Accessibility. *J. Am. Chem. Soc.* **1997**, *119* (30), 7019–7029. https://doi.org/10.1021/ja970754m.

(63)   Murray, C. B.; Norris, D. J.; Bawendi, M. G. Synthesis and Characterization of Nearly Monodisperse CdE (E = Sulfur, Selenium, Tellurium) Semiconductor Nanocrystallites. *J. Am. Chem. Soc.* **1993**, *115* (19), 8706–8715. https://doi.org/10.1021/ja00072a025.

(64)   Herron, N.; Wang, Y.; Eckert, H. Synthesis and Characterization of Surface-Capped, Size-Quantized Cadmium Sulfide Clusters. Chemical Control of Cluster Size. *J. Am. Chem. Soc.* **1990**, *112* (4), 1322–1326. https://doi.org/10.1021/ja00160a004.

(65)   Kim, S.; Bawendi, M. G. Oligomeric Ligands for Luminescent and Stable Nanocrystal Quantum Dots. *J. Am. Chem. Soc.* **2003**, *125* (48), 14652–14653. https://doi.org/10.1021/ja0368094.

(66)   McBride, J.; Treadway, J.; Feldman, L. C.; Pennycook, S. J.; Rosenthal, S. J. Structural Basis for Near Unity Quantum Yield Core/Shell Nanostructures. *Nano Lett.* **2006**, *6* (7), 1496–1501. https://doi.org/10.1021/nl060993k.

(67)   Chen, Y.; Vela, J.; Htoon, H.; Casson, J. L.; Werder, D. J.; Bussian, D. A.; Klimov, V. I.; Hollingsworth, J. A. "Giant" Multishell CdSe Nanocrystal Quantum Dots with Suppressed Blinking. *J. Am. Chem. Soc.* **2008**, *130* (15), 5026–5027. https://doi.org/10.1021/ja711379k.

(68)   Mahler, B.; Spinicelli, P.; Buil, S.; Quelin, X.; Hermier, J.-P.; Dubertret, B. Towards Non-Blinking Colloidal Quantum Dots. *Nat. Mater.* **2008**, *7* (8), 659–664. https://doi.org/10.1038/nmat2222.

(69)   Vela, J.; Htoon, H.; Chen, Y.; Park, Y.-S.; Ghosh, Y.; Goodwin, P. M.; Werner, J. H.; Wells, N. P.; Casson, J. L.; Hollingsworth, J. A. Effect of Shell Thickness and Composition on Blinking Suppression and the Blinking Mechanism in 'Giant' CdSe/CdS Nanocrystal Quantum Dots. *J. Biophotonics* **2010**, *3* (10–11), 706–717. https://doi.org/10.1002/jbio.201000058.

(70)   Lee, K.-H.; Lee, J.-H.; Kang, H.-D.; Park, B.; Kwon, Y.; Ko, H.; Lee, C.; Lee, J.; Yang, H. Over 40 Cd/A Efficient Green Quantum Dot Electroluminescent Device Comprising Uniquely Large-Sized Quantum Dots.

ACS Nano **2014**, *8* (5), 4893–4901. https://doi.org/10.1021/nn500852g.

(71)   Manna, L.; Scher, E. C.; Li, L. S.; Alivisatos, A. P. Epitaxial Growth and Photochemical Annealing of Graded CdS/ZnS Shells on Colloidal CdSe Nanorods. *J. Am. Chem. Soc.* **2002**, *124* (24), 7136–7145. https://doi.org/10.1021/ja025946i.

(72)   Talapin, D. V.; Mekis, I.; Götzinger, S.; Kornowski, A.; Benson, O.; Weller, H. CdSe/CdS/ZnS and CdSe/ZnSe/ZnS Core−Shell−Shell Nanocrystals. *J. Phys. Chem. B* **2004**, *108* (49), 18826–18831. https://doi.org/10.1021/jp046481g.

(73)   Xie, R.; Kolb, U.; Li, J.; Basché, T.; Mews, A. Synthesis and Characterization of Highly Luminescent CdSe−Core CdS/Zn 0.5 Cd 0.5 S/ZnS Multishell Nanocrystals. *J. Am. Chem. Soc.* **2005**, *127* (20), 7480–7488. https://doi.org/10.1021/ja042939g.

(74)   Bae, W. K.; Char, K.; Hur, H.; Lee, S. Single-Step Synthesis of Quantum Dots with Chemical Composition Gradients. *Chem. Mater.* **2008**, *20* (2), 531–539. https://doi.org/10.1021/cm070754d.

(75)   Lim, J.; Jeong, B. G.; Park, M.; Kim, J. K.; Pietryga, J. M.; Park, Y.-S.; Klimov, V. I.; Lee, C.; Lee, D. C.; Bae, W. K. Influence of Shell Thickness on the Performance of Light-Emitting Devices Based on CdSe/Zn 1-X Cd X S Core/Shell Heterostructured Quantum Dots. *Adv. Mater.* **2014**, *26* (47), 8034–8040. https://doi.org/10.1002/adma.201403620.

(76)   Brus, L. Quantum Crystallites and Nonlinear Optics. *Appl. Phys. A Solids Surfaces* **1991**, *53* (6), 465–474. https://doi.org/10.1007/BF00331535.

(77)   Hollingsworth, J. A.; Klimov, V. I. "Soft" Chemical Synthesis and Manipulation of Semiconductor Nanocrystals. In *Nanocrystal Quantum Dots*; Klimov, V. I., Ed.; CRC Press, 2010; pp 1–62.

(78)   Lim, J.; Park, Y.-S.; Wu, K.; Yun, H. J.; Klimov, V. I. Droop-Free Colloidal Quantum Dot Light-Emitting Diodes. *Nano Lett.* **2018**, *18* (10), 6645–6653. https://doi.org/10.1021/acs.nanolett.8b03457.

(79)   Panda, S. K.; Hickey, S. G.; Waurisch, C.; Eychmüller, A. Gradated Alloyed CdZnSe Nanocrystals with High Luminescence Quantum Yields and Stability for Optoelectronic and Biological Applications. *J. Mater. Chem.* **2011**, *21* (31), 11550. https://doi.org/10.1039/c1jm11375e.

(80)   Shibata, M.; Sakai, Y.; Yokoyama, D. Advantages and Disadvantages of Vacuum-Deposited and Spin-Coated Amorphous Organic Semiconductor Films for Organic Light-Emitting Diodes. *J. Mater. Chem. C* **2015**, *3* (42), 11178–11191. https://doi.org/10.1039/C5TC01911G.

(81)   Qian, L.; Zheng, Y.; Xue, J.; Holloway, P. H. Stable and Efficient Quantum-Dot Light-Emitting Diodes Based on Solution-Processed Multilayer Structures. *Nat. Photonics* **2011**, *5* (9), 543–548. https://doi.org/10.1038/nphoton.2011.171.

(82)   Mashford, B. S.; Stevenson, M.; Popovic, Z.; Hamilton, C.; Zhou, Z.; Breen, C.; Steckel, J.; Bulovic, V.;

Bawendi, M.; Coe-Sullivan, S.; et al. High-Efficiency Quantum-Dot Light-Emitting Devices with Enhanced Charge Injection. *Nat. Photonics* **2013**, *7* (5), 407–412. https://doi.org/10.1038/nphoton.2013.70.

(83)   Hatwar, T.; Kondakova, M.; Giesen, D.; Spindler, J. OLED Materials and Device Architectures for Full-Color Displays and Solid-State Lighting. In *Organic Electronics: Materials, Processing, Devices and Applications*; So, F., Ed.; CRC Press, 2009; pp 433–509. https://doi.org/10.1201/9781420072914-c14.

(84)   Kim, S.-Y.; Jeong, W.-I.; Mayr, C.; Park, Y.-S.; Kim, K.-H.; Lee, J.-H.; Moon, C.-K.; Brütting, W.; Kim, J.-J. Organic Light-Emitting Diodes with 30% External Quantum Efficiency Based on a Horizontally Oriented Emitter. *Adv. Funct. Mater.* **2013**, *23* (31), 3896–3900. https://doi.org/10.1002/adfm.201300104.

(85)   Minaev, B.; Baryshnikov, G.; Agren, H. Principles of Phosphorescent Organic Light Emitting Devices. *Phys. Chem. Chem. Phys.* **2014**, *16* (5), 1719–1758. https://doi.org/10.1039/C3CP53806K.

(86)   Efros, A. L. Fine Structure and Polarization Properties of Band-Edge Excitons in Semiconductor Nanocrystals. In *Nanocrystal Quantum Dots*; Klimov, V. I., Ed.; CRC Press, 2010; pp 97–132.

(87)   Spanhel, L.; Haase, M.; Weller, H.; Henglein, A. Photochemistry of Colloidal Semiconductors. 20. Surface Modification and Stability of Strong Luminescing CdS Particles. *J. Am. Chem. Soc.* **1987**, *109* (19), 5649–5655. https://doi.org/10.1021/ja00253a015.

(88)   van Sark, W. G. J. H. M.; Frederix, P. L. T. M.; Bol, A. A.; Gerritsen, H. C.; Meijerink, A. Blueing, Bleaching, and Blinking of Single CdSe/ZnS Quantum Dots. *ChemPhysChem* **2002**, *3* (10), 871–879. https://doi.org/10.1002/1439-7641(20021018)3:10<871::AID-CPHC871>3.0.CO;2-T.

(89)   Qin, W.; Guyot-Sionnest, P. Evidence for the Role of Holes in Blinking: Negative and Oxidized CdSe/CdS Dots. *ACS Nano* **2012**, *6* (10), 9125–9132. https://doi.org/10.1021/nn303396c.

(90)   Park, Y.-S.; Bae, W. K.; Pietryga, J. M.; Klimov, V. I. Auger Recombination of Biexcitons and Negative and Positive Trions in Individual Quantum Dots. *ACS Nano* **2014**, *8* (7), 7288–7296. https://doi.org/10.1021/nn5023473.

(91)   Jain, A.; Voznyy, O.; Hoogland, S.; Korkusinski, M.; Hawrylak, P.; Sargent, E. H. Atomistic Design of CdSe/CdS Core–Shell Quantum Dots with Suppressed Auger Recombination. *Nano Lett.* **2016**, *16* (10), 6491–6496. https://doi.org/10.1021/acs.nanolett.6b03059.

(92)   Vaxenburg, R.; Rodina, A.; Lifshitz, E.; Efros, A. L. Biexciton Auger Recombination in CdSe/CdS Core/Shell Semiconductor Nanocrystals. *Nano Lett.* **2016**, *16* (4), 2503–2511. https://doi.org/10.1021/acs.nanolett.6b00066.

(93)   Hou, X.; Kang, J.; Qin, H.; Chen, X.; Ma, J.; Zhou, J.; Chen, L.; Wang, L.; Wang, L.-W.; Peng, X. Engineering Auger Recombination in Colloidal Quantum Dots via Dielectric Screening. *Nat. Commun.* **2019**, *10* (1), 1750. https://doi.org/10.1038/s41467-019-09737-2.

(94)   Park, Y.-S.; Lim, J.; Makarov, N. S.; Klimov, V. I. Effect of Interfacial Alloying versus "Volume Scaling" on Auger Recombination in Compositionally Graded Semiconductor Quantum Dots. *Nano Lett.* **2017**, *17* (9), 5607–5613. https://doi.org/10.1021/acs.nanolett.7b02438.

(95)   Chepic, D. I.; Efros, A. L.; Ekimov, A. I.; Ivanov, M. G.; Kharchenko, V. A.; Kudriavtsev, I. A.; Yazeva, T. V. Auger Ionization of Semiconductor Quantum Drops in a Glass Matrix. *J. Lumin.* **1990**, *47* (3), 113–127. https://doi.org/10.1016/0022-2313(90)90007-X.

(96)   Efros, A. L.; Kharchenko, V. A.; Rosen, M. Breaking the Phonon Bottleneck in Nanometer Quantum Dots: Role of Auger-like Processes. *Solid State Commun.* **1995**, *93* (4), 281–284. https://doi.org/10.1016/0038-1098(94)00760-8.

(97)   Klimov, V. I.; Mikhailovsky, A. A.; McBranch, D. W.; Leatherdale, C. A.; Bawendi, M. G. Quantization of Multiparticle Auger Rates in Semiconductor Quantum Dots. *Science (80-.).* **2000**, *287* (5455), 1011–1013. https://doi.org/10.1126/science.287.5455.1011.

(98)   Pietryga, J. M.; Zhuravlev, K. K.; Whitehead, M.; Klimov, V. I.; Schaller, R. D. Evidence for Barrierless Auger Recombination in PbSe Nanocrystals: A Pressure-Dependent Study of Transient Optical Absorption. *Phys. Rev. Lett.* **2008**, *101* (21), 217401. https://doi.org/10.1103/PhysRevLett.101.217401.

(99)   García-Santamaría, F.; Brovelli, S.; Viswanatha, R.; Hollingsworth, J. A.; Htoon, H.; Crooker, S. A.; Klimov, V. I. Breakdown of Volume Scaling in Auger Recombination in CdSe/CdS Heteronanocrystals: The Role of the Core−Shell Interface. *Nano Lett.* **2011**, *11* (2), 687–693. https://doi.org/10.1021/nl103801e.

(100)   Greenham, N. C. Electrical Properties of Semiconductor Nanocrystals. In *Nanocrystal Quantum Dots*; Klimov, V. I., Ed.; CRC Press, 2010; pp 235–280.

(101)   Tse, S.; Cheung, C.; So, S. Charge Transport and Injection in Amorphous Organic Semiconductors. In *Organic Electronics: Materials, Processing, Devices and Applications*; So, F., Ed.; CRC Press, 2009; pp 61–109. https://doi.org/10.1201/9781420072914-c3.

(102)   Li, L.; Meller, G.; Kosina, H. Charge Injection Model in Organic Light-Emitting Diodes Based on a Master Equation. In *Simulation of Semiconductor Processes and Devices 2007*; Grasser, T., Selberherr, S., Eds.; Springer Vienna: Vienna, 2007; pp 377–380.

(103)   Baranovskii, S. D.; Rubel, O.; Jansson, F.; Österbacka, R. Description of Charge Transport in Disordered Organic Materials. In *Organic Electronics*; Springer, 2010; pp 45–71. https://doi.org/10.1007/12 2009 2.

(104)   Li, L.; Kosina, H. Charge Transport in Organic Semiconductor Devices. In *Organic Electronics*; Meller, G., Grasser, T., Eds.; Springer, 2010; pp 301–323. https://doi.org/10.1007/12 2009 14.

(105)   Wu, W.-F.; Chiou, B.-S. Effect of Annealing on Electrical and Optical Properties of RF Magnetron Sputtered Indium Tin Oxide Films. *Appl. Surf. Sci.* **1993**, *68* (4), 497–504. https://doi.org/10.1016/0169-4332(93)90233-

2.

(106) Ahmed, N. M.; Sabah, F. A.; Abdulgafour, H. I.; Alsadig, A.; Sulieman, A.; Alkhoaryef, M. The Effect of Post Annealing Temperature on Grain Size of Indium-Tin-Oxide for Optical and Electrical Properties Improvement. *Results Phys.* **2019**, *13* (December 2018), 102159. https://doi.org/10.1016/j.rinp.2019.102159.

(107) Wang, H. C.; Zhang, H.; Chen, H. Y.; Yeh, H. C.; Tseng, M. R.; Chung, R. J.; Chen, S.; Liu, R. S. Cadmium-Free InP/ZnSeS/ZnS Heterostructure-Based Quantum Dot Light-Emitting Diodes with a ZnMgO Electron Transport Layer and a Brightness of Over 10 000 Cd M−2. *Small* **2017**, *13* (13), 1–7. https://doi.org/10.1002/smll.201603962.

(108) Tang, C. W.; VanSlyke, S. A. Organic Electroluminescent Diodes. *Appl. Phys. Lett.* **1987**, *51* (12), 913–915. https://doi.org/10.1063/1.98799.

(109) Schlamp, M. C.; Peng, X.; Alivisatos, A. P. Improved Efficiencies in Light Emitting Diodes Made with CdSe(CdS) Core/Shell Type Nanocrystals and a Semiconducting Polymer. *J. Appl. Phys.* **1997**, *82* (11), 5837–5842. https://doi.org/10.1063/1.366452.

(110) Kang, Y.; Song, Z.; Jiang, X.; Yin, X.; Fang, L.; Gao, J.; Su, Y.; Zhao, F. Quantum Dots for Wide Color Gamut Displays from Photoluminescence to Electroluminescence. *Nanoscale Res. Lett.* **2017**, *12* (1), 1–8. https://doi.org/10.1186/s11671-017-1907-1.

(111) Mutlugun, E.; Guzelturk, B.; Abiyasa, A. P.; Gao, Y.; Sun, X. W.; Demir, H. V. Colloidal Quantum Dot Light-Emitting Diodes Employing Phosphorescent Small Organic Molecules as Efficient Exciton Harvesters. *J. Phys. Chem. Lett.* **2014**, *5* (16), 2802–2807. https://doi.org/10.1021/jz5012669.

(112) Anikeeva, P. O.; Madigan, C. F.; Halpert, J. E.; Bawendi, M. G.; Bulović, V. Electronic and Excitonic Processes in Light-Emitting Devices Based on Organic Materials and Colloidal Quantum Dots. *Phys. Rev. B* **2008**, *78* (8), 085434. https://doi.org/10.1103/PhysRevB.78.085434.

(113) Achermann, M.; Petruska, M. A.; Kos, S.; Smith, D. L.; Koleske, D. D.; Klimov, V. I. Energy-Transfer Pumping of Semiconductor Nanocrystals Using an Epitaxial Quantum Well. *Nature* **2004**, *429* (6992), 642–646. https://doi.org/10.1038/nature02571.

(114) Féry, C.; Racine, B.; Vaufrey, D.; Doyeux, H.; Cinà, S. Physical Mechanism Responsible for the Stretched Exponential Decay Behavior of Aging Organic Light-Emitting Diodes. *Appl. Phys. Lett.* **2005**, *87* (21), 213502. https://doi.org/10.1063/1.2133922.

(115) Cao, W.; Xiang, C.; Yang, Y.; Chen, Q.; Chen, L.; Yan, X.; Qian, L. Highly Stable QLEDs with Improved Hole Injection via Quantum Dot Structure Tailoring. *Nat. Commun.* **2018**, *9* (1), 2608. https://doi.org/10.1038/s41467-018-04986-z.

(116) Zeng, Q.; Xu, Z.; Zheng, C.; Liu, Y.; Chen, W.; Guo, T.; Li, F.; Xiang, C.; Yang, Y.; Cao, W.; et al. Improving

Charge Injection via a Blade-Coating Molybdenum Oxide Layer: Toward High-Performance Large-Area Quantum-Dot Light-Emitting Diodes. *ACS Appl. Mater. Interfaces* **2018**, *10* (9), 8258–8264. https://doi.org/10.1021/acsami.7b19333.

(117)   Colvin, V. L.; Schlamp, M. C.; Alivisatos, A. P. Light-Emitting Diodes Made from Cadmium Selenide Nanocrystals and a Semiconducting Polymer. *Nature* **1994**, *370* (6488), 354–357. https://doi.org/10.1038/370354a0.

(118)   Mattoussi, H.; Radzilowski, L. H.; Dabbousi, B. O.; Thomas, E. L.; Bawendi, M. G.; Rubner, M. F. Electroluminescence from Heterostructures of Poly(Phenylene Vinylene) and Inorganic CdSe Nanocrystals. *J. Appl. Phys.* **1998**, *83* (12), 7965–7974. https://doi.org/10.1063/1.367978.

(119)   Stouwdam, J. W.; Janssen, R. A. J. Red, Green, and Blue Quantum Dot LEDs with Solution Processable ZnO Nanocrystal Electron Injection Layers. *J. Mater. Chem.* **2008**, *18* (16), 1889. https://doi.org/10.1039/b800028j.

(120)   Caruge, J. M.; Halpert, J. E.; Wood, V.; Bulović, V.; Bawendi, M. G. Colloidal Quantum-Dot Light-Emitting Diodes with Metal-Oxide Charge Transport Layers. *Nat. Photonics* **2008**, *2* (4), 247–250. https://doi.org/10.1038/nphoton.2008.34.

(121)   Yang, Z.; Wu, Q.; Lin, G.; Zhou, X.; Wu, W.; Yang, X.; Zhang, J.; Li, W. All-Solution Processed Inverted Green Quantum Dot Light-Emitting Diodes with Concurrent High Efficiency and Long Lifetime. *Mater. Horizons* **2019**, *6* (10), 2009–2015. https://doi.org/10.1039/C9MH01053J.

(122)   Wang, L.; Lin, J.; Hu, Y.; Guo, X.; Lv, Y.; Tang, Z.; Zhao, J.; Fan, Y.; Zhang, N.; Wang, Y.; et al. Blue Quantum Dot Light-Emitting Diodes with High Electroluminescent Efficiency. *ACS Appl. Mater. Interfaces* **2017**, *9* (44), 38755–38760. https://doi.org/10.1021/acsami.7b10785.

(123)   Bae, W. K.; Park, Y.-S.; Lim, J.; Lee, D.; Padilha, L. A.; McDaniel, H.; Robel, I.; Lee, C.; Pietryga, J. M.; Klimov, V. I. Controlling the Influence of Auger Recombination on the Performance of Quantum-Dot Light-Emitting Diodes. *Nat. Commun.* **2013**, *4* (1), 2661. https://doi.org/10.1038/ncomms3661.

(124)   Dai, X.; Zhang, Z.; Jin, Y.; Niu, Y.; Cao, H.; Liang, X.; Chen, L.; Wang, J.; Peng, X. Solution-Processed, High-Performance Light-Emitting Diodes Based on Quantum Dots. *Nature* **2014**, *515* (7525), 96–99. https://doi.org/10.1038/nature13829.

(125)   Manders, J. R.; Qian, L.; Titov, A.; Hyvonen, J.; Tokarz-Scott, J.; Acharya, K. P.; Yang, Y.; Cao, W.; Zheng, Y.; Xue, J.; et al. High Efficiency and Ultra-Wide Color Gamut Quantum Dot LEDs for next Generation Displays. *J. Soc. Inf. Disp.* **2015**, *23* (11), 523–528. https://doi.org/10.1002/jsid.393.

(126)   Kim, H.-M.; Geng, D.; Kim, J.; Hwang, E.; Jang, J. Metal-Oxide Stacked Electron Transport Layer for Highly Efficient Inverted Quantum-Dot Light Emitting Diodes. *ACS Appl. Mater. Interfaces* **2016**, *8* (42), 28727–28736. https://doi.org/10.1021/acsami.6b10314.

(127)   Kirkwood, N.; Singh, B.; Mulvaney, P. Enhancing Quantum Dot LED Efficiency by Tuning Electron Mobility in the ZnO Electron Transport Layer. *Adv. Mater. Interfaces* **2016**, *3* (22), 1600868. https://doi.org/10.1002/admi.201600868.

(128)   Zhang, H.; Sui, N.; Chi, X.; Wang, Y.; Liu, Q.; Zhang, H.; Ji, W. Ultrastable Quantum-Dot Light-Emitting Diodes by Suppression of Leakage Current and Exciton Quenching Processes. *ACS Appl. Mater. Interfaces* **2016**, *8* (45), 31385–31391. https://doi.org/10.1021/acsami.6b09246.

(129)   Liang, F.; Liu, Y.; Hu, Y.; Shi, Y.-L.; Liu, Y.-Q.; Wang, Z.-K.; Wang, X.-D.; Sun, B.-Q.; Liao, L.-S. Polymer as an Additive in the Emitting Layer for High-Performance Quantum Dot Light-Emitting Diodes. *ACS Appl. Mater. Interfaces* **2017**, *9* (23), 20239–20246. https://doi.org/10.1021/acsami.7b05629.

(130)   Ding, K.; Chen, H.; Fan, L.; Wang, B.; Huang, Z.; Zhuang, S.; Hu, B.; Wang, L. Polyethylenimine Insulativity-Dominant Charge-Injection Balance for Highly Efficient Inverted Quantum Dot Light-Emitting Diodes. *ACS Appl. Mater. Interfaces* **2017**, *9* (23), 20231–20238. https://doi.org/10.1021/acsami.7b04662.

(131)   Shen, H.; Lin, Q.; Cao, W.; Yang, C.; Shewmon, N. T.; Wang, H.; Niu, J.; Li, L. S.; Xue, J. Efficient and Long-Lifetime Full-Color Light-Emitting Diodes Using High Luminescence Quantum Yield Thick-Shell Quantum Dots. *Nanoscale* **2017**, *9* (36), 13583–13591. https://doi.org/10.1039/C7NR04953F.

(132)   Acharya, K. P.; Titov, A.; Hyvonen, J.; Wang, C.; Tokarz, J.; Holloway, P. H. High Efficiency Quantum Dot Light Emitting Diodes from Positive Aging. *Nanoscale* **2017**, *9* (38), 14451–14457. https://doi.org/10.1039/c7nr05472f.

(133)   Chen, H.; Ding, K.; Fan, L.; Liu, W.; Zhang, R.; Xiang, S.; Zhang, Q.; Wang, L. All-Solution-Processed Quantum Dot Light Emitting Diodes Based on Double Hole Transport Layers by Hot Spin-Coating with Highly Efficient and Low Turn-On Voltage. *ACS Appl. Mater. Interfaces* **2018**, *10* (34), 29076–29082. https://doi.org/10.1021/acsami.8b06917.

(134)   Liu, Y.; Jiang, C.; Song, C.; Wang, J.; Mu, L.; He, Z.; Zhong, Z.; Cun, Y.; Mai, C.; Wang, J.; et al. Highly Efficient All-Solution Processed Inverted Quantum Dots Based Light Emitting Diodes. *ACS Nano* **2018**, *12* (2), 1564–1570. https://doi.org/10.1021/acsnano.7b08129.

(135)   Kim, H.-M.; Cho, S.; Kim, J.; Shin, H.; Jang, J. Li and Mg Co-Doped Zinc Oxide Electron Transporting Layer for Highly Efficient Quantum Dot Light-Emitting Diodes. *ACS Appl. Mater. Interfaces* **2018**, *10* (28), 24028–24036. https://doi.org/10.1021/acsami.8b04721.

(136)   Su, Q.; Sun, Y.; Zhang, H.; Chen, S. Origin of Positive Aging in Quantum-Dot Light-Emitting Diodes. *Adv. Sci.* **2018**, *5* (10), 1800549. https://doi.org/10.1002/advs.201800549.

(137)   Zhang, Z.; Ye, Y.; Pu, C.; Deng, Y.; Dai, X.; Chen, X.; Chen, D.; Zheng, X.; Gao, Y.; Fang, W.; et al. High-Performance, Solution-Processed, and Insulating-Layer-Free Light-Emitting Diodes Based on Colloidal Quantum Dots. *Adv. Mater.* **2018**, *30* (28), 1801387. https://doi.org/10.1002/adma.201801387.

(138)   Xiong, X.; Wei, C.; Xie, L.; Chen, M.; Tang, P.; Shen, W.; Deng, Z.; Li, X.; Duan, Y.; Su, W.; et al. Realizing 17.0% External Quantum Efficiency in Red Quantum Dot Light-Emitting Diodes by Pursuing the Ideal Inkjet-Printed Film and Interface. *Org. Electron.* **2019**, *73* (June), 247–254. https://doi.org/10.1016/j.orgel.2019.06.016.

(139)   Zhiwei, M.; Liping, T.; Bingbing, L. Highly Efficient Full Color Light-Emitting Diodes Based on Quantum Dots Surface Passivation Engineering. *Org. Electron.* **2019**, *70* (August 2018), 140–148. https://doi.org/10.1016/j.orgel.2019.04.014.

(140)   Zhu, Y.; Hu, H.; Liu, Y.; Zheng, X.; Ju, S.; Lin, W.; Guo, T.; Li, F. Efficient Hole Injection of MoOx -Doped Organic Layer for Printable Red Quantum Dot Light-Emitting Diodes. *IEEE Electron Device Lett.* **2019**, *40* (7), 1147–1150. https://doi.org/10.1109/LED.2019.2916933.

(141)   Zhang, M.; Hu, B.; Meng, L.; Bian, R.; Wang, S.; Wang, Y.; Liu, H.; Jiang, L. Ultrasmooth Quantum Dot Micropatterns by a Facile Controllable Liquid-Transfer Approach: Low-Cost Fabrication of High-Performance QLED. *J. Am. Chem. Soc.* **2018**, *140* (28), 8690–8695. https://doi.org/10.1021/jacs.8b02948.

(142)   Zou, Y.; Ban, M.; Cui, W.; Huang, Q.; Wu, C.; Liu, J.; Wu, H.; Song, T.; Sun, B. A General Solvent Selection Strategy for Solution Processed Quantum Dots Targeting High Performance Light-Emitting Diode. *Adv. Funct. Mater.* **2016**, *27* (1), 1603325. https://doi.org/10.1002/adfm.201603325.

(143)   Cao, F.; Wang, H.; Shen, P.; Li, X.; Zheng, Y.; Shang, Y.; Zhang, J.; Ning, Z.; Yang, X. High-Efficiency and Stable Quantum Dot Light-Emitting Diodes Enabled by a Solution-Processed Metal-Doped Nickel Oxide Hole Injection Interfacial Layer. *Adv. Funct. Mater.* **2017**, *27* (42), 1704278. https://doi.org/10.1002/adfm.201704278.

(144)   Kim, H.-M.; Kim, J.; Cho, S.-Y.; Jang, J. Solution-Processed Metal-Oxide p–n Charge Generation Junction for High-Performance Inverted Quantum-Dot Light-Emitting Diodes. *ACS Appl. Mater. Interfaces* **2017**, *9* (44), 38678–38686. https://doi.org/10.1021/acsami.7b14584.

(145)   Fu, Y.; Kim, D.; Moon, H.; Yang, H.; Chae, H. Hexamethyldisilazane-Mediated, Full-Solution-Processed Inverted Quantum Dot-Light-Emitting Diodes. *J. Mater. Chem. C* **2017**, *5* (3), 522–526. https://doi.org/10.1039/C6TC05119G.

(146)   Li, Z.; Hu, Y.; Shen, H.; Lin, Q.; Wang, L.; Wang, H.; Zhao, W.; Li, L. S. Efficient and Long-Life Green Light-Emitting Diodes Comprising Tridentate Thiol Capped Quantum Dots. *Laser Photon. Rev.* **2017**, *11* (1), 1600227. https://doi.org/10.1002/lpor.201600227.

(147)   Sun, Y.; Wang, W.; Zhang, H.; Su, Q.; Wei, J.; Liu, P.; Chen, S.; Zhang, S. High-Performance Quantum Dot Light-Emitting Diodes Based on Al-Doped ZnO Nanoparticles Electron Transport Layer. *ACS Appl. Mater. Interfaces* **2018**, *10* (22), 18902–18909. https://doi.org/10.1021/acsami.8b04754.

(148)   Fu, Y.; Jiang, W.; Kim, D.; Lee, W.; Chae, H. Highly Efficient and Fully Solution-Processed Inverted Light-

Emitting Diodes with Charge Control Interlayers. *ACS Appl. Mater. Interfaces* **2018**, *10* (20), 17295–17300. https://doi.org/10.1021/acsami.8b05092.

(149) Sun, Y.; Chen, W.; Wu, Y.; He, Z.; Zhang, S.; Chen, S. A Low-Temperature-Annealed and UV-Ozone-Enhanced Combustion Derived Nickel Oxide Hole Injection Layer for Flexible Quantum Dot Light-Emitting Diodes. *Nanoscale* **2019**, *11* (3), 1021–1028. https://doi.org/10.1039/C8NR08976K.

(150) Wang, X.; Shen, P.; Cao, F.; Wang, S.; Wang, H.; Wu, Q.; Zhang, J.; Yang, X. Stepwise Bi-Layer Hole-Transport Interlayers With Deep Highest Occupied Molecular Orbital Level for Efficient Green Quantum Dot Light-Emitting Diodes. *IEEE Electron Device Lett.* **2019**, *40* (7), 1139–1142. https://doi.org/10.1109/LED.2019.2916584.

(151) Zhu, Y.; Hu, H.; Liu, Y.; Chen, M.; Lin, W.; Ye, Y.; Guo, T.; Li, F. All-Solution-Processed High-Performance Quantum Dot Light Emitting Devices Employing an Inorganic Thiocyanate as Hole Injection Layer. *Org. Electron.* **2019**, *70* (April), 279–285. https://doi.org/10.1016/j.orgel.2019.04.037.

(152) Jin, H.; Moon, H.; Lee, W.; Hwangbo, H.; Yong, S. H.; Chung, H. K.; Chae, H. Charge Balance Control of Quantum Dot Light Emitting Diodes with Atomic Layer Deposited Aluminum Oxide Interlayers. *RSC Adv.* **2019**, *9* (21), 11634–11640. https://doi.org/10.1039/C9RA00145J.

(153) Wang, L.; Chen, T.; Lin, Q.; Shen, H.; Wang, A.; Wang, H.; Li, C.; Li, L. S. High-Performance Azure Blue Quantum Dot Light-Emitting Diodes via Doping PVK in Emitting Layer. *Org. Electron.* **2016**, *37*, 280–286. https://doi.org/10.1016/j.orgel.2016.06.032.

(154) Lin, Q.; Wang, L.; Li, Z.; Shen, H.; Guo, L.; Kuang, Y.; Wang, H.; Li, L. S. Nonblinking Quantum-Dot-Based Blue Light-Emitting Diodes with High Efficiency and a Balanced Charge-Injection Process. *ACS Photonics* **2018**, *5* (3), 939–946. https://doi.org/10.1021/acsphotonics.7b01195.

(155) Cheng, T.; Wang, F.; Sun, W.; Wang, Z.; Zhang, J.; You, B.; Li, Y.; Hayat, T.; Alsaed, A.; Tan, Z. High-Performance Blue Quantum Dot Light-Emitting Diodes with Balanced Charge Injection. *Adv. Electron. Mater.* **2019**, *5* (4), 1800794. https://doi.org/10.1002/aelm.201800794.

(156) Chen, S.; Cao, W.; Liu, T.; Tsang, S.-W.; Yang, Y.; Yan, X.; Qian, L. On the Degradation Mechanisms of Quantum-Dot Light-Emitting Diodes. *Nat. Commun.* **2019**, *10* (1), 765. https://doi.org/10.1038/s41467-019-08749-2.

(157) Dienel, T.; Proehl, H.; Forker, R.; Leo, K.; Fritz, T. Metal-Induced Photoluminescence Quenching of Organic Molecular Crystals. *J. Phys. Chem. C* **2008**, *112* (24), 9056–9060. https://doi.org/10.1021/jp709718t.

(158) Burin, A. L.; Ratner, M. a. Exciton Migration and Cathode Quenching in Organic Light Emitting Diodes. *J. Phys. Chem. A* **2000**, *104*, 4704–4710. https://doi.org/10.1021/jp994162x.

(159) Dabbousi, B. O.; Bawendi, M. G.; Onitsuka, O.; Rubner, M. F. Electroluminescence from CdSe Quantum-

dot/Polymer Composites. *Appl. Phys. Lett.* **1995**, *66* (11), 1316–1318. https://doi.org/10.1063/1.113227.

(160)   Coe, S.; Woo, W.-K.; Bawendi, M.; Bulović, V. Electroluminescence from Single Monolayers of Nanocrystals in Molecular Organic Devices. *Nature* **2002**, *420* (6917), 800–803. https://doi.org/10.1038/nature01217.

(161)   Coe-Sullivan, S.; Woo, W.-K.; Steckel, J. S.; Bawendi, M.; Bulović, V. Tuning the Performance of Hybrid Organic/Inorganic Quantum Dot Light-Emitting Devices. *Org. Electron.* **2003**, *4* (2–3), 123–130. https://doi.org/10.1016/j.orgel.2003.08.016.

(162)   Coe-Sullivan, S.; Steckel, J. S.; Woo, W.-K.; Bawendi, M. G.; Bulović, V. Large-Area Ordered Quantum-Dot Monolayers via Phase Separation During Spin-Casting. *Adv. Funct. Mater.* **2005**, *15* (7), 1117–1124. https://doi.org/10.1002/adfm.200400468.

(163)   Hikmet, R. A. M.; Chin, P. T. K.; Talapin, D. V.; Weller, H. Polarized-Light-Emitting Quantum-Rod Diodes. *Adv. Mater.* **2005**, *17* (11), 1436–1439. https://doi.org/10.1002/adma.200401763.

(164)   Adachi, C.; Baldo, M. A.; Thompson, M. E.; Forrest, S. R. Nearly 100% Internal Phosphorescence Efficiency in an Organic Light-Emitting Device. *J. Appl. Phys.* **2001**, *90* (10), 5048–5051. https://doi.org/10.1063/1.1409582.

(165)   Zhang, Y. Q.; Cao, X. A. Electroluminescence of Green CdSe/ZnS Quantum Dots Enhanced by Harvesting Excitons from Phosphorescent Molecules. *Appl. Phys. Lett.* **2010**, *97* (25), 253115. https://doi.org/10.1063/1.3530450.

(166)   Anikeeva, P. O.; Halpert, J. E.; Bawendi, M. G.; Bulović, V. Quantum Dot Light-Emitting Devices with Electroluminescence Tunable over the Entire Visible Spectrum. *Nano Lett.* **2009**, *9* (7), 2532–2536. https://doi.org/10.1021/nl9002969.

(167)   Caruge, J.-M.; Halpert, J. E.; Bulović, V.; Bawendi, M. G. NiO as an Inorganic Hole-Transporting Layer in Quantum-Dot Light-Emitting Devices. *Nano Lett.* **2006**, *6* (12), 2991–2994. https://doi.org/10.1021/nl0623208.

(168)   Kim, Y.; Ippen, C.; Fischer, B.; Lange, A.; Wedel, A. Efficiency Enhancement of InP-Based Inverted QD-LEDs by Incorporation of a Polyethylenimine Modified Al:ZnO Layer. *J. Soc. Inf. Disp.* **2015**, *23* (8), 377–383. https://doi.org/10.1002/jsid.322.

(169)   Jiang, C.; Zhong, Z.; Liu, B.; He, Z.; Zou, J.; Wang, L.; Wang, J.; Peng, J.; Cao, Y. Coffee-Ring-Free Quantum Dot Thin Film Using Inkjet Printing from a Mixed-Solvent System on Modified ZnO Transport Layer for Light-Emitting Devices. *ACS Appl. Mater. Interfaces* **2016**, *8* (39), 26162–26168. https://doi.org/10.1021/acsami.6b08679.

(170)   Ji, C.; Lu, M.; Wu, H.; Zhang, X.; Shen, X.; Wang, X.; Zhang, Y.; Wang, Y.; Yu, W. W. 1,2-Ethanedithiol

Treatment for AgIn 5 S 8 /ZnS Quantum Dot Light-Emitting Diodes with High Brightness. *ACS Appl. Mater. Interfaces* **2017**, *9* (9), 8187–8193. https://doi.org/10.1021/acsami.6b16238.

(171)   Davidson-Hall, T.; Aziz, H. The Role of Polyethylenimine in Enhancing the Efficiency of Quantum Dot Light-Emitting Devices. *Nanoscale* **2018**, *10* (5), 2623–2631. https://doi.org/10.1039/C7NR07683E.

(172)   Kim, H. H.; Park, S.; Yi, Y.; Son, D. I.; Park, C.; Hwang, D. K.; Choi, W. K. Inverted Quantum Dot Light Emitting Diodes Using Polyethylenimine Ethoxylated Modified ZnO. *Sci. Rep.* **2015**, *5* (1), 8968. https://doi.org/10.1038/srep08968.

(173)   Kim, H. H.; Shim, J. W.; You, Y.-J.; Lee, Y. J.; Park, C.; Hwang, D. K.; Choi, W. K. Highly Flexible Inverted-Quantum-Dot Light-Emitting Diodes on Elastic Polyurethane Substrates. *J. Mater. Chem. C* **2017**, *5* (7), 1596–1600. https://doi.org/10.1039/C6TC04310K.

(174)   Shen, P.; Cao, F.; Wang, H.; Wei, B.; Wang, F.; Sun, X. W.; Yang, X. Solution-Processed Double-Junction Quantum-Dot Light-Emitting Diodes with an EQE of Over 40%. *ACS Appl. Mater. Interfaces* **2019**, *11* (1), 1065–1070. https://doi.org/10.1021/acsami.8b18940.

(175)   Cao, F.; Zhao, D.; Shen, P.; Wu, J.; Wang, H.; Wu, Q.; Wang, F.; Yang, X. High-Efficiency, Solution-Processed White Quantum Dot Light-Emitting Diodes with Serially Stacked Red/Green/Blue Units. *Adv. Opt. Mater.* **2018**, *6* (20), 1800652. https://doi.org/10.1002/adom.201800652.

(176)   Zhang, Y.; Zhang, F.; Wang, H.; Wang, L.; Wang, F.; Lin, Q.; Shen, H.; Li, L. S. High-Efficiency CdSe/CdS Nanorod–Based Red Light–Emitting Diodes. *Opt. Express* **2019**, *27* (6), 7935. https://doi.org/10.1364/OE.27.007935.

(177)   Yang, X.; Zhang, Z.-H.; Ding, T.; Wang, N.; Chen, G.; Dang, C.; Demir, H. V.; Sun, X. W. High-Efficiency All-Inorganic Full-Colour Quantum Dot Light-Emitting Diodes. *Nano Energy* **2018**, *46* (February), 229–233. https://doi.org/10.1016/j.nanoen.2018.02.002.

(178)   Kim, H.-M.; Youn, J.-H.; Seo, G.-J.; Jang, J. Inverted Quantum-Dot Light-Emitting Diodes with Solution-Processed Aluminium–Zinc Oxide as a Cathode Buffer. *J. Mater. Chem. C* **2013**, *1* (8), 1567–1573. https://doi.org/10.1039/C2TC00339B.

(179)   Sun, Y.; Peng, H.; Chen, S.; Zhang, S. P-117: Inverted Quantum Dot Light-Emitting Diodes with MgZnO Modified Electron Transport Layer. *SID Symp. Dig. Tech. Pap.* **2017**, *48* (1), 1699–1701. https://doi.org/10.1002/sdtp.11991.

(180)   Xia, F.; Sun, X. W.; Chen, S. Alternating-Current Driven Quantum-Dot Light-Emitting Diodes with High Brightness. *Nanoscale* **2019**, *11* (12), 5231–5239. https://doi.org/10.1039/C8NR10461A.

(181)   Lee, Y.; Kim, H.-M.; Kim, J.; Jang, J. Remarkable Lifetime Improvement of Quantum-Dot Light Emitting Diodes by Incorporating Rubidium Carbonate in Metal-Oxide Electron Transport Layers. *J. Mater. Chem. C*

2019, *7* (32), 10082–10091. https://doi.org/10.1039/C9TC02683E.

(182)   Jiang, C.; Liu, H.; Liu, B.; Zhong, Z.; Zou, J.; Wang, J.; Wang, L.; Peng, J.; Cao, Y. Improved Performance of Inverted Quantum Dots Light Emitting Devices by Introducing Double Hole Transport Layers. *Org. Electron.* **2016**, *31* (2016), 82–89. https://doi.org/10.1016/j.orgel.2016.01.009.

(183)   Ji, W.; Lv, Y.; Jing, P.; Zhang, H.; Wang, J.; Zhang, H.; Zhao, J. Highly Efficient and Low Turn-On Voltage Quantum Dot Light-Emitting Diodes by Using a Stepwise Hole-Transport Layer. *ACS Appl. Mater. Interfaces* **2015**, *7* (29), 15955–15960. https://doi.org/10.1021/acsami.5b04050.

(184)   Kathirgamanathan, P.; Kumaraverl, M.; Bramananthan, N.; Ravichandran, S. High Efficiency and Highly Saturated Red Emitting Inverted Quantum Dot Devices (QLEDs): Optimisation of Their Efficiencies with Low Temperature Annealed Sol–Gel Derived ZnO as the Electron Transporter and a Novel High Mobility Hole Transporter and Thermal. *J. Mater. Chem. C* **2018**, *6* (43), 11622–11644. https://doi.org/10.1039/C8TC03676D.

(185)   Zhu, B.; Ji, W.; Duan, Z.; Sheng, Y.; Wang, T.; Yuan, Q.; Zhang, H.; Tang, X.; Zhang, H. Low Turn-on Voltage and Highly Bright Ag–In–Zn–S Quantum Dot Light-Emitting Diodes. *J. Mater. Chem. C* **2018**, *6* (17), 4683–4690. https://doi.org/10.1039/C8TC01022F.

(186)   Huang, X.; Su, S.; Su, Q.; Zhang, H.; Wen, F.; Chen, S. The Influence of the Hole Transport Layers on the Performance of Blue and Color Tunable Quantum Dot Light-Emitting Diodes. *J. Soc. Inf. Disp.* **2018**, *26* (8), 470–476. https://doi.org/10.1002/jsid.681.

(187)   Ji, W.; Jing, P.; Zhao, J.; Liu, X.; Wang, A.; Li, H. Inverted CdSe/CdS/ZnS Quantum Dot Light Emitting Devices with Titanium Dioxide as an Electron-Injection Contact. *Nanoscale* **2013**, *5* (8), 3474–3480. https://doi.org/10.1039/c3nr34168b.

(188)   Zamani Siboni, H.; Sadeghimakki, B.; Sivoththaman, S.; Aziz, H. Very High Brightness Quantum Dot Light-Emitting Devices via Enhanced Energy Transfer from a Phosphorescent Sensitizer. *ACS Appl. Mater. Interfaces* **2015**, *7* (46), 25828–25834. https://doi.org/10.1021/acsami.5b08097.

(189)   Ji, W.; Jing, P.; Zhang, L.; Li, D.; Zeng, Q.; Qu, S.; Zhao, J. The Work Mechanism and Sub-Bandgap-Voltage Electroluminescence in Inverted Quantum Dot Light-Emitting Diodes. *Sci. Rep.* **2015**, *4* (1), 6974. https://doi.org/10.1038/srep06974.

(190)   Zhang, Y.-N.; Liu, Y.-S.; Yan, M.-M.; Wei, Y.; Zhang, Q.-L.; Zhang, Y. Efficient Quantum-Dot Light-Emitting Diodes Employing Thermally Activated Delayed Fluorescence Emitters as Exciton Harvesters. *ACS Appl. Mater. Interfaces* **2018**, *10* (8), 7435–7441. https://doi.org/10.1021/acsami.7b16579.

(191)   Zheng, W.; Xu, Z.; Song, D.; Zhao, S.; Qiao, B.; Chen, J.; Wang, P.; Zheng, X. Enhancing the Efficiency and the Luminance of Quantum Dot Light-Emitting Diodes by Inserting a Leaked Electron Harvesting Layer with Thermal-Activated Delayed Fluorescence Material. *Org. Electron.* **2019**, *65*, 357–362.

https://doi.org/10.1016/j.orgel.2018.11.031.

(192) Cho, Y. J.; Zhang, Y.; Yu, H.; Aziz, H. The Root Causes of the Limited Stability of Solution-Coated Small-Molecule Organic Light-Emitting Devices: Faster Host Aggregation by Exciton–Polaron Interactions. *Adv. Funct. Mater.* **2016**, *26* (47), 8662–8669. https://doi.org/10.1002/adfm.201603542.

(193) Tsang, D. P.-K.; Matsushima, T.; Adachi, C. Operational Stability Enhancement in Organic Light-Emitting Diodes with Ultrathin Liq Interlayers. *Sci. Rep.* **2016**, *6* (1), 22463. https://doi.org/10.1038/srep22463.

(194) Yu, H.; Zhang, Y.; Cho, Y. J.; Aziz, H. Exciton-Induced Degradation of Carbazole-Based Host Materials and Its Role in the Electroluminescence Spectral Changes in Phosphorescent Organic Light Emitting Devices with Electrical Aging. *ACS Appl. Mater. Interfaces* **2017**, *9* (16), 14145–14152. https://doi.org/10.1021/acsami.7b01432.

(195) Giebink, N. C.; D'Andrade, B. W.; Weaver, M. S.; Mackenzie, P. B.; Brown, J. J.; Thompson, M. E.; Forrest, S. R. Intrinsic Luminance Loss in Phosphorescent Small-Molecule Organic Light Emitting Devices Due to Bimolecular Annihilation Reactions. *J. Appl. Phys.* **2008**, *103* (4), 044509. https://doi.org/10.1063/1.2884530.

(196) Setzer, T.; Friederich, P.; Meded, V.; Wenzel, W.; Lennartz, C.; Dreuw, A. Meltdown! Local Heating by Decaying Excited Host Positive Polarons Triggers Aggregation Quenching in Blue PhOLEDs. *ChemPhysChem* **2018**, *19* (21), 2961–2966. https://doi.org/10.1002/cphc.201800250.

(197) Chang, J. H.; Park, P.; Jung, H.; Jeong, B. G.; Hahm, D.; Nagamine, G.; Ko, J.; Cho, J.; Padilha, L. A.; Lee, D. C.; et al. Unraveling the Origin of Operational Instability of Quantum Dot Based Light-Emitting Diodes. *ACS Nano* **2018**, *12* (10), 10231–10239. https://doi.org/10.1021/acsnano.8b03386.

(198) Davidson-Hall, T.; Aziz, H. The Role of Excitons within the Hole Transporting Layer in Quantum Dot Light Emitting Device Degradation. *Nanoscale* **2019**, *11* (17), 8310–8318. https://doi.org/10.1039/C8NR09560D.

(199) Znaidi, L. Sol-Gel-Deposited ZnO Thin Films: A Review. *Mater. Sci. Eng. B Solid-State Mater. Adv. Technol.* **2010**, *174* (1–3), 18–30. https://doi.org/10.1016/j.mseb.2010.07.001.

(200) Jou, J.-H.; Kumar, S.; Singh, M.; Chen, Y.-H.; Chen, C.-C.; Lee, M.-T. Carrier Modulation Layer-Enhanced Organic Light-Emitting Diodes. *Molecules* **2015**, *20* (7), 13005–13030. https://doi.org/10.3390/molecules200713005.

(201) Räupke, A.; Palma-Cando, A.; Shkura, E.; Teckhausen, P.; Polywka, A.; Görrn, P.; Scherf, U.; Riedl, T. Highly Sensitive Gas-Phase Explosive Detection by Luminescent Microporous Polymer Networks. *Sci. Rep.* **2016**, *6* (March), 1–7. https://doi.org/10.1038/srep29118.

(202) Yook, K. S.; Lee, J. Y. Organic Materials for Deep Blue Phosphorescent Organic Light-Emitting Diodes. *Adv. Mater.* **2012**, *24* (24), 3169–3190. https://doi.org/10.1002/adma.201200627.

(203) Su, S.-J.; Sasabe, H.; Takeda, T.; Kido, J. Pyridine-Containing Bipolar Host Materials for Highly Efficient

Blue Phosphorescent OLEDs. *Chem. Mater.* **2008**, *20* (5), 1691–1693. https://doi.org/10.1021/cm703682q.

(204) Ngo, P. S.; Hung, M. K.; Tsai, K. W.; Sharma, S.; Chen, S. A. Highly Efficient Solution-Processed Thermally Activated Delayed Fluorescence Bluish-Green and Hybrid White Organic Light-Emitting Diodes Using Novel Bipolar Host Materials. *ACS Appl. Mater. Interfaces* **2019**, *11* (49), 45939–45948. https://doi.org/10.1021/acsami.9b14168.

(205) Lee, J.-H.; Lin, T.-C.; Liao, C.-C.; Yang, F. H. Study on Organic Light-Emitting Device with More Balanced Charge Transport. In *Proc. SPIE*; Yu, G., Chen, C., Lee, C., Eds.; 2005; Vol. 5632, p 220. https://doi.org/10.1117/12.576013.

(206) Xiao, L.; Chen, Z.; Qu, B.; Luo, J.; Kong, S.; Gong, Q.; Kido, J. Recent Progresses on Materials for Electrophosphorescent Organic Light-Emitting Devices. *Adv. Mater.* **2011**, *23* (8), 926–952. https://doi.org/10.1002/adma.201003128.

(207) Furukawa, T.; Nakanotani, H.; Inoue, M.; Adachi, C. Dual Enhancement of Electroluminescence Efficiency and Operational Stability by Rapid Upconversion of Triplet Excitons in OLEDs. *Sci. Rep.* **2015**, *5* (1), 8429. https://doi.org/10.1038/srep08429.

(208) Tao, S.; Hong, Z.; Peng, Z.; Ju, W.; Zhang, X.; Wang, P.; Wu, S.; Lee, S. Anthracene Derivative for a Non-Doped Blue-Emitting Organic Electroluminescence Device with Both Excellent Color Purity and High Efficiency. *Chem. Phys. Lett.* **2004**, *397* (1–3), 1–4. https://doi.org/10.1016/j.cplett.2004.07.111.

(209) Luo, Y.; Aziz, H. Correlation Between Triplet-Triplet Annihilation and Electroluminescence Efficiency in Doped Fluorescent Organic Light-Emitting Devices. *Adv. Funct. Mater.* **2010**, *20* (8), 1285–1293. https://doi.org/10.1002/adfm.200902329.

(210) Okamoto, S.; Tanaka, K.; Izumi, Y.; Adachi, H.; Yamaji, T.; Suzuki, T. Simple Measurement of Quantum Efficiency in Organic Electroluminescent Devices. *Jpn. J. Appl. Phys.* **2001**, *40* (Part 2, No. 7B), L783–L784. https://doi.org/10.1143/JJAP.40.L783.

(211) Cusumano, P. Study of Voltage Decrease in Organic Light Emitting Diodes during the Initial Stage of Lifetime. *Solid. State. Electron.* **2016**, *116*, 30–32. https://doi.org/10.1016/j.sse.2015.11.032.

(212) Xiao, H.; Xiao, X.; Wu, D.; Wang, R.; Wang, K.; Chiang, K. S. Effects of Injection Current on the Modulation Bandwidths of Quantum-Dot Light-Emitting Diodes. *IEEE Trans. Electron Devices* **2019**, *66* (11), 4805–4810. https://doi.org/10.1109/TED.2019.2941561.

(213) Anikeeva, P. O.; Madigan, C. F.; Coe-Sullivan, S. A.; Steckel, J. S.; Bawendi, M. G.; Bulović, V. Photoluminescence of CdSe/ZnS Core/Shell Quantum Dots Enhanced by Energy Transfer from a Phosphorescent Donor. *Chem. Phys. Lett.* **2006**, *424* (1–3), 120–125. https://doi.org/10.1016/j.cplett.2006.04.009.

(214)   Wood, V.; Panzer, M. J.; Halpert, J. E.; Caruge, J.-M.; Bawendi, M. G.; Bulović, V. Selection of Metal Oxide Charge Transport Layers for Colloidal Quantum Dot LEDs. *ACS Nano* **2009**, *3* (11), 3581–3586. https://doi.org/10.1021/nn901074r.

(215)   Zhang, Y.; Wang, S.; Chen, L.; Fang, Y.; Shen, H.; Du, Z. Solution-Processed Quantum Dot Light-Emitting Diodes Based on NiO Nanocrystals Hole Injection Layer. *Org. Electron.* **2017**, *44* (2017), 189–197. https://doi.org/10.1016/j.orgel.2017.02.023.

(216)   Pan, J.; Chen, J.; Huang, Q.; Khan, Q.; Liu, X.; Tao, Z.; Zhang, Z.; Lei, W.; Nathan, A. Size Tunable ZnO Nanoparticles To Enhance Electron Injection in Solution Processed QLEDs. *ACS Photonics* **2016**, *3* (2), 215–222. https://doi.org/10.1021/acsphotonics.5b00267.

(217)   Son, D. I.; Kim, H. H.; Cho, S.; Hwang, D. K.; Seo, J. W.; Choi, W. K. Carrier Transport of Inverted Quantum Dot LED with PEIE Polymer. *Org. Electron.* **2014**, *15* (4), 886–892. https://doi.org/10.1016/j.orgel.2014.01.014.

(218)   Son, D. I.; Kim, H. H.; Hwang, D. K.; Kwon, S.; Choi, W. K. Inverted CdSe–ZnS Quantum Dots Light-Emitting Diode Using Low-Work Function Organic Material Polyethylenimine Ethoxylated. *J. Mater. Chem. C* **2014**, *2* (3), 510–514. https://doi.org/10.1039/C3TC31297F.

(219)   Zhou, Y.; Fuentes-Hernandez, C.; Shim, J.; Meyer, J.; Giordano, A. J.; Li, H.; Winget, P.; Papadopoulos, T.; Cheun, H.; Kim, J.; et al. A Universal Method to Produce Low-Work Function Electrodes for Organic Electronics. *Science (80-.).* **2012**, *336* (6079), 327–332. https://doi.org/10.1126/science.1218829.

(220)   Li, P.; Wang, G.; Cai, L.; Ding, B.; Zhou, D.; Hu, Y.; Zhang, Y.; Xiang, J.; Wan, K.; Chen, L.; et al. High-Efficiency Inverted Polymer Solar Cells Controlled by the Thickness of Polyethylenimine Ethoxylated (PEIE) Interfacial Layers. *Phys. Chem. Chem. Phys.* **2014**, *16* (43), 23792–23799. https://doi.org/10.1039/c4cp03484h.

(221)   Kang, H.; Hong, S.; Lee, J.; Lee, K. Electrostatically Self-Assembled Nonconjugated Polyelectrolytes as an Ideal Interfacial Layer for Inverted Polymer Solar Cells. *Adv. Mater.* **2012**, *24* (22), 3005–3009. https://doi.org/10.1002/adma.201200594.

(222)   Courtright, B. A. E.; Jenekhe, S. A. Polyethylenimine Interfacial Layers in Inverted Organic Photovoltaic Devices: Effects of Ethoxylation and Molecular Weight on Efficiency and Temporal Stability. *ACS Appl. Mater. Interfaces* **2015**, *7* (47), 26167–26175. https://doi.org/10.1021/acsami.5b08147.

(223)   Kim, Y. H.; Han, T. H.; Cho, H.; Min, S. Y.; Lee, C. L.; Lee, T. W. Polyethylene Imine as an Ideal Interlayer for Highly Efficient Inverted Polymer Light-Emitting Diodes. *Adv. Funct. Mater.* **2014**, *24* (24), 3808–3814. https://doi.org/10.1002/adfm.201304163.

(224)   Stolz, S.; Scherer, M.; Mankel, E.; Lovrinčić, R.; Schinke, J.; Kowalsky, W.; Jaegermann, W.; Lemmer, U.; Mechau, N.; Hernandez-Sosa, G. Investigation of Solution-Processed Ultrathin Electron Injection Layers for

Organic Light-Emitting Diodes. *ACS Appl. Mater. Interfaces* **2014**, *6* (9), 6616–6622. https://doi.org/10.1021/am500287y.

(225) Stolz, S.; Zhang, Y.; Lemmer, U.; Hernandez-Sosa, G.; Aziz, H. Degradation Mechanisms in Organic Light-Emitting Diodes with Polyethylenimine as a Solution-Processed Electron Injection Layer. *ACS Appl. Mater. Interfaces* **2017**, *9* (3), 2776–2785. https://doi.org/10.1021/acsami.6b15062.

(226) van Reenen, S.; Kouijzer, S.; Janssen, R. A. J.; Wienk, M. M.; Kemerink, M. Origin of Work Function Modification by Ionic and Amine-Based Interface Layers. *Adv. Mater. Interfaces* **2014**, *1* (8), 1400189. https://doi.org/10.1002/admi.201400189.

(227) Fokina, A.; Lee, Y.; Chang, J. H.; Park, M.; Sung, Y.; Bae, W. K.; Char, K.; Lee, C.; Zentel, R. The Role of Emission Layer Morphology on the Enhanced Performance of Light-Emitting Diodes Based on Quantum Dot-Semiconducting Polymer Hybrids. *Adv. Mater. Interfaces* **2016**, *3* (18), 1600279. https://doi.org/10.1002/admi.201600279.

(228) Ok, K.-H.; Kim, J.; Park, S.-R.; Kim, Y.; Lee, C.-J.; Hong, S.-J.; Kwak, M.-G.; Kim, N.; Han, C. J.; Kim, J.-W. Ultra-Thin and Smooth Transparent Electrode for Flexible and Leakage-Free Organic Light-Emitting Diodes. *Sci. Rep.* **2015**, *5* (1), 9464. https://doi.org/10.1038/srep09464.

(229) Talapin, D. V.; Nelson, J. H.; Shevchenko, E. V.; Aloni, S.; Sadtler, B.; Alivisatos, A. P. Seeded Growth of Highly Luminescent CdSe/CdS Nanoheterostructures with Rod and Tetrapod Morphologies. *Nano Lett.* **2007**, *7* (10), 2951–2959. https://doi.org/10.1021/nl072003g.

(230) Sitt, A.; Hadar, I.; Banin, U. Band-Gap Engineering, Optoelectronic Properties and Applications of Colloidal Heterostructured Semiconductor Nanorods. *Nano Today* **2013**, *8* (5), 494–513. https://doi.org/10.1016/j.nantod.2013.08.002.

(231) Shi, Y.-L.; Liang, F.; Hu, Y.; Wang, X.-D.; Wang, Z.-K.; Liao, L.-S. High-Efficiency Quantum Dot Light-Emitting Diodes Employing Lithium Salt Doped Poly(9-Vinlycarbazole) as a Hole-Transporting Layer. *J. Mater. Chem. C* **2017**, *5* (22), 5372–5377. https://doi.org/10.1039/C7TC00449D.

(232) Sun, B.; Sirringhaus, H. Solution-Processed Zinc Oxide Field-Effect Transistors Based on Self-Assembly of Colloidal Nanorods. *Nano Lett.* **2005**, *5* (12), 2408–2413. https://doi.org/10.1021/nl051586w.

(233) Gupta, S.; Zhang, Q.; Emrick, T.; Russell, T. P. "Self-Corralling" Nanorods under an Applied Electric Field. *Nano Lett.* **2006**, *6* (9), 2066–2069. https://doi.org/10.1021/nl061336v.

(234) Aziz, H.; Popovic, Z.; Xie, S.; Hor, A.-M.; Hu, N.-X.; Tripp, C.; Xu, G. Humidity-Induced Crystallization of Tris (8-Hydroxyquinoline) Aluminum Layers in Organic Light-Emitting Devices. *Appl. Phys. Lett.* **1998**, *72* (7), 756–758. https://doi.org/10.1063/1.120867.

(235) Jonda, C.; Mayer, A. B. R.; Stolz, U.; Elschner, A.; Karbach, A. Surface Roughness Effects and Their

Influence on the Degradation of Organic Light Emitting Devices. *J. Mater. Sci.* **2000**, *35* (22), 5645–5651. https://doi.org/10.1023/A:1004842004640.

(236)   Liu, G.; Kerr, J. B.; Johnson, S. Dark Spot Formation Relative to ITO Surface Roughness for Polyfluorene Devices. *Synth. Met.* **2004**, *144* (1), 1–6. https://doi.org/10.1016/j.synthmet.2004.01.011.

(237)   Kim, T.-H.; Cho, K.-S.; Lee, E. K.; Lee, S. J.; Chae, J.; Kim, J. W.; Kim, D. H.; Kwon, J.-Y.; Amaratunga, G.; Lee, S. Y.; et al. Full-Colour Quantum Dot Displays Fabricated by Transfer Printing. *Nat. Photonics* **2011**, *5* (3), 176–182. https://doi.org/10.1038/nphoton.2011.12.

(238)   Wang, Q.; Williams, G.; Aziz, H. Photo-Degradation of the Indium Tin Oxide (ITO)/Organic Interface in Organic Optoelectronic Devices and a New Outlook on the Role of ITO Surface Treatments and Interfacial Layers in Improving Device Stability. *Org. Electron.* **2012**, *13* (10), 2075–2082. https://doi.org/10.1016/j.orgel.2012.06.017.

(239)   Scholz, S.; Walzer, K.; Leo, K. Analysis of Complete Organic Semiconductor Devices by Laser Desorption/Ionization Time-of-Flight Mass Spectrometry. *Adv. Funct. Mater.* **2008**, *18* (17), 2541–2547. https://doi.org/10.1002/adfm.200700816.

(240)   Kim, S.; Moon, H.; Gupta, D.; Yoo, S.; Choi, Y.-K. Resistive Switching Characteristics of Sol–Gel Zinc Oxide Films for Flexible Memory Applications. *IEEE Trans. Electron Devices* **2009**, *56* (4), 696–699. https://doi.org/10.1109/TED.2009.2012522.

(241)   Gong, S.; He, X.; Chen, Y.; Jiang, Z.; Zhong, C.; Ma, D.; Qin, J.; Yang, C. Simple CBP Isomers with High Triplet Energies for Highly Efficient Blue Electrophosphorescence. *J. Mater. Chem.* **2012**, *22* (7), 2894–2899. https://doi.org/10.1039/C1JM14903B.

(242)   Saragi, T. P. I.; Spehr, T.; Siebert, A.; Fuhrmann-Lieker, T.; Salbeck, J. Spiro Compounds for Organic Optoelectronics. *Chem. Rev.* **2007**, *107* (4), 1011–1065. https://doi.org/10.1021/cr0501341.

(243)   Duan, L.; Hou, L.; Lee, T.-W.; Qiao, J.; Zhang, D.; Dong, G.; Wang, L.; Qiu, Y. Solution Processable Small Molecules for Organic Light-Emitting Diodes. *J. Mater. Chem.* **2010**, *20* (31), 6392–6407. https://doi.org/10.1039/b926348a.

(244)   Jones, M.; Nedeljkovic, J.; Ellingson, R. J.; Nozik, A. J.; Rumbles, G. Photoenhancement of Luminescence in Colloidal CdSe Quantum Dot Solutions. *J. Phys. Chem. B* **2003**, *107* (41), 11346–11352. https://doi.org/10.1021/jp035598m.

(245)   Kondakov, D. Y.; Young, R. H. Variable Sensitivity of Organic Light-Emitting Diodes to Operation-Induced Chemical Degradation: Nature of the Antagonistic Relationship between Lifetime and Efficiency. *J. Appl. Phys.* **2010**, *108* (7), 074513. https://doi.org/10.1063/1.3483251.

(246)   Sandanayaka, A. S. D.; Matsushima, T.; Adachi, C. Degradation Mechanisms of Organic Light-Emitting

Diodes Based on Thermally Activated Delayed Fluorescence Molecules. *J. Phys. Chem. C* **2015**, *119* (42), 23845–23851. https://doi.org/10.1021/acs.jpcc.5b07084.

(247)   Kim, S.; Bae, H. J.; Park, S.; Kim, W.; Kim, J.; Kim, J. S.; Jung, Y.; Sul, S.; Ihn, S.-G.; Noh, C.; et al. Degradation of Blue-Phosphorescent Organic Light-Emitting Devices Involves Exciton-Induced Generation of Polaron Pair within Emitting Layers. *Nat. Commun.* **2018**, *9* (1), 1211. https://doi.org/10.1038/s41467-018-03602-4.

(248)   Kim, S. H.; Jang, J.; Lee, J. Y. Relationship between Host Energy Levels and Device Performances of Phosphorescent Organic Light-Emitting Diodes with Triplet Mixed Host Emitting Structure. *Appl. Phys. Lett.* **2007**, *91* (8), 083511. https://doi.org/10.1063/1.2773941.

(249)   Zhang, Y.; Aziz, H. Influence of the Guest on Aggregation of the Host by Exciton-Polaron Interactions and Its Effects on the Stability of Phosphorescent Organic Light-Emitting Devices. *ACS Appl. Mater. Interfaces* **2016**, *8* (22), 14088–14095. https://doi.org/10.1021/acsami.6b02946.

(250)   Li, X.; Zhao, Y.-B.; Fan, F.; Levina, L.; Liu, M.; Quintero-Bermudez, R.; Gong, X.; Quan, L. N.; Fan, J.; Yang, Z.; et al. Bright Colloidal Quantum Dot Light-Emitting Diodes Enabled by Efficient Chlorination. *Nat. Photonics* **2018**, *12* (3), 159–164. https://doi.org/10.1038/s41566-018-0105-8.

(251)   Cho, Y. R.; Kang, P.-G.; Shin, D. H.; Kim, J.-H.; Maeng, M.-J.; Sakong, J.; Hong, J.-A.; Park, Y.; Suh, M. C. Effect of Anode Buffer Layer on the Efficiency of Inverted Quantum-Dot Light-Emitting Diodes. *Appl. Phys. Express* **2016**, *9* (1), 012103. https://doi.org/10.7567/APEX.9.012103.

(252)   Zhao, Y.; Zhang, J.; Liu, S.; Gao, Y.; Yang, X.; Leck, K. S.; Abiyasa, A. P.; Divayana, Y.; Mutlugun, E.; Tan, S. T.; et al. Transition Metal Oxides on Organic Semiconductors. *Org. Electron.* **2014**, *15* (4), 871–877. https://doi.org/10.1016/j.orgel.2014.01.011.

(253)   Hikmet, R. A. M.; Talapin, D. V.; Weller, H. Study of Conduction Mechanism and Electroluminescence in CdSe/ZnS Quantum Dot Composites. *J. Appl. Phys.* **2003**, *93* (6), 3509–3514. https://doi.org/10.1063/1.1542940.

(254)   Lin, B.-Y.; Easley, C. J.; Chen, C.-H.; Tseng, P.-C.; Lee, M.-Z.; Sher, P.-H.; Wang, J.-K.; Chiu, T.-L.; Lin, C.-F.; Bardeen, C. J.; et al. Exciplex-Sensitized Triplet–Triplet Annihilation in Heterojunction Organic Thin-Film. *ACS Appl. Mater. Interfaces* **2017**, *9* (12), 10963–10970. https://doi.org/10.1021/acsami.6b16397.

(255)   Lee, J.; Lee, J.-I.; Chu, H. Y. Improved Performance of White Phosphorescent Organic Light-Emitting Diodes through a Mixed-Host Structure. *ETRI J.* **2009**, *31* (6), 642–646. https://doi.org/10.4218/etrij.09.1209.0005.

(256)   Qiao, X.; Chen, J.; Li, X.; Ma, D. Observation of Hole Hopping via Dopant in MoOx-Doped Organic Semiconductors: Mechanism Analysis and Application for High Performance Organic Light-Emitting Devices. *J. Appl. Phys.* **2010**, *107* (10), 104505. https://doi.org/10.1063/1.3428374.

(257)   Vasan, R.; Salman, H.; Manasreh, M. O. Solution Processed High Efficiency Quantum Dot Light Emitting Diode With Inorganic Charge Transport Layers. *IEEE Electron Device Lett.* **2018**, *39* (4), 536–539. https://doi.org/10.1109/LED.2018.2808679.